
Electronic Thesis and Dissertation Repository

6-19-2014 12:00 AM

Image-based registration methods for quantification and compensation of prostate motion during trans-rectal ultrasound (TRUS)-guided biopsy

Tharindu De Silva
The University of Western Ontario

Supervisor

Dr. Aaron Fenster
The University of Western Ontario Joint Supervisor

Dr. Aaron Ward
The University of Western Ontario Joint Supervisor

Dr. Jagath Samarabandu
The University of Western Ontario

Graduate Program in Biomedical Engineering

A thesis submitted in partial fulfillment of the requirements for the degree in Doctor of Philosophy

© Tharindu De Silva 2014. Works at: <https://ir.lib.uwo.ca/etd>



Part of the [Bioimaging and Biomedical Optics Commons](#)

Recommended Citation

De Silva, Tharindu, "Image-based registration methods for quantification and compensation of prostate motion during trans-rectal ultrasound (TRUS)-guided biopsy" (2014). *Electronic Thesis and Dissertation Repository*. 2110.

<https://ir.lib.uwo.ca/etd/2110>

This Dissertation/Thesis is brought to you for free and open access by Scholarship@Western. It has been accepted for inclusion in Electronic Thesis and Dissertation Repository by an authorized administrator of Scholarship@Western. For more information, please contact wlsadmin@uwo.ca.

IMAGE-BASED REGISTRATION METHODS FOR
QUANTIFICATION AND COMPENSATION OF PROSTATE MOTION
DURING TRANS-RECTAL ULTRASOUND (TRUS)-GUIDED BIOPSY

(Thesis format: Integrated Article)

by

Tharindu De Silva

Graduate Program in Biomedical Engineering

A thesis submitted in partial fulfillment
of the requirements for the degree of
Doctor of Philosophy

The School of Graduate and Postdoctoral Studies
The University of Western Ontario
London, Ontario, Canada

© Tharindu De Silva 2014

Abstract

Prostate biopsy is the clinical standard for cancer diagnosis and is typically performed under two-dimensional (2D) transrectal ultrasound (TRUS) for needle guidance.

Unfortunately, most early stage prostate cancers are not visible on ultrasound and the procedure suffers from high false negative rates due to the lack of visible targets. Fusion of pre-biopsy MRI to 3D TRUS for targeted biopsy could improve cancer detection rates and volume of tumor sampled. In MRI-TRUS fusion biopsy systems, patient or prostate motion during the procedure causes misalignments in the MR targets mapped to the live 2D TRUS images, limiting the targeting accuracy of the biopsy system.

In order to sample smallest clinically significant tumours of 0.5 cm^3 with 95% confidence, the root mean square (RMS) error of the biopsy system needs to be $<2.5 \text{ mm}$. In addition to intermittent prostate motion during the procedure, prostate deformation due to needle insertion and biopsy gun firing is a potential source of error that limits needle targeting accuracy. Using non-rigid registration of 2D TRUS images, we quantified the deformation that occurs during the needle insertion and the biopsy gun firing and showed that the tissue deformation was such that throughout the length of the needle axis, spherical tumours with radius 2.1 mm or more can be sampled with 95% confidence, under the assumption of zero error elsewhere in the biopsy system.

The target misalignments due to intermittent prostate motion during the procedure can be compensated by registering the live 2D TRUS images acquired during the biopsy procedure to the pre-acquired baseline 3D TRUS image. The registration must be performed both accurately and quickly in order to be useful during the clinical procedure. We developed an intensity-based 2D-3D rigid registration algorithm and validated it by

calculating the target registration error (TRE) using manually identified fiducials within the prostate. We discuss two different approaches that can be used to improve the robustness of this registration to meet the clinical requirements. Firstly, we evaluated the impact of intra-procedural 3D TRUS imaging on motion compensation accuracy since the limited anatomical context available in live 2D TRUS images could limit the robustness of the 2D-3D registration. The results indicated that TRE improved when intra-procedural 3D TRUS images were used in registration, with larger improvements in the base and apex regions as compared with the mid-gland region. Secondly, we developed and evaluated a registration algorithm whose optimization is based on learned prostate motion characteristics. Compared to our initial approach, the updated optimization improved the robustness during 2D-3D registration by reducing the number of registrations with a $TRE > 5$ mm from 9.2% to 1.2% with an overall RMS TRE of 2.3 mm.

The methods developed in this work were intended to improve the needle targeting accuracy of 3D TRUS-guided biopsy systems. The successful integration of the techniques into current 3D TRUS-guided systems could improve the overall cancer detection rate during the biopsy and help to achieve earlier diagnosis and fewer repeat biopsy procedures in prostate cancer diagnosis.

Keywords: prostate biopsy, three-dimensional ultrasound, transrectal ultrasound, prostate motion, motion compensation, image registration, 2D-3D registration, registration optimization

Co-Authorship

This thesis is an integration of four articles, each constituting a chapter; the journal publications listed in the following are either published, in revision, or in preparation for submission.

Chapter 2: Quantification of prostate deformation due to needle insertion during TRUS-guided biopsy: Comparison of hand-held and mechanically stabilized systems, *Medical Physics*, 38 (3), 1718-32 (2011).

My contributions for this work included data preparation, development of software to perform image registration, manual identification of fiducials for validation, implementation of software for results analysis and validation, and manuscript preparation. C. Romagnoli and J. Izawa acquired the necessary clinical images to perform the experiments. The work was motivated by A. Ward who contributed many ideas related to image registration and statistical data analysis in a supervisory role and helped in manuscript preparation. All authors helped in manuscript review. The work was performed under the supervision of J. Samarabandu and A. Fenster.

Chapter 3: 2D-3D rigid registration to compensate for prostate motion during 3D TRUS-guided biopsy, *Medical Physics*, 40(2), 022904, (2013).

My contributions for this chapter included data selection and preparation, development of software algorithms to perform registrations, manual identification of fiducials for validation, developing software code for validation, and manuscript preparation. C. Romagnoli acquired clinical images for this retrospective study and L. Gardi helped with the data acquisition, recording and clinical integration of the software to the biopsy platform. R. Zhao helped with the graphics processing unit (GPU) implementation of the

code. All authors helped in the manuscript preparation and review. The work was conducted under the supervision of A. Ward and A. Fenster.

Chapter 4: Evaluating the utility of intra-procedure 3D TRUS image information in guiding registration for motion compensation during prostate biopsy, submitted to Medical Physics, January, 2014 - currently under revision.

My contributions to this work included data preparation, writing software to perform image registration experiments, writing software code to perform validation, and manuscript preparation. D. Cool and C. Romagnoli were involved in clinical image acquisition. D. Cool manually identified fiducials in the images for validation and provided clinical perspectives with many brainstorming sessions. All authors aided in manuscript preparation. This work was performed under the supervision A. Ward and A. Fenster.

Chapter 5: Robust 2D-3D registration optimization using learned prostate motion data, this work is currently under preparation to IEEE TMI.

Preliminary version of this work was published in the proceedings of Medical Image Computing and Computer Assistant Intervention (MICCAI), 2013. My contributions to this work included data preparation, development and implementation of registration algorithms, writing software code to perform validation, and manuscript preparation. D. Cool and C. Romagnoli were involved in clinical image acquisitions. D. Cool manually identified fiducials in the images for validation. The work was performed under the supervision of A. Ward and A. Fenster.

Acknowledgements

The support and guidance of many individuals were instrumental to the completion of the work presented in this thesis. Firstly, I would like to thank Dr. Aaron Fenster for the mentorship and supervision provided throughout my graduate studies. I am profoundly inspired by his experienced perspectives in vastly diverse areas and his passionate enthusiasm in graduate supervision. His influence moulded my research trajectory during my graduate studies and cultivated the motivation to continue to grow as a researcher.

I was extremely fortunate to have been able to work with Dr. Aaron Ward from the very beginning of my graduate studies. I would like to express my utmost gratitude for his enormous amount of time and effort that nourished this work and instilled in me a continuous passion for research. His availability to engage in illuminating brainstorming sessions, his perspectives on research methodology and his detailed feedback to improve written/oral presentation skills when disseminating research work were instrumental in shaping my academic and personal growth during these years.

I am indebted to Dr. Jagath Samarabandu for providing me the opportunity to reach greater heights in research and his guidance and encouragement provided throughout the years in many different ways as a supervisor. I would also like to thank Dr. Abbas Samani for his guidance and mentorship as a member of the advisory committee.

Many individuals in Dr. Fenster's lab and Western University contributed to build an academically stimulating environment to perform cutting-edge research. I would like to especially thank Dr. Derek Cool for his involvement and enthusiasm shown for this research. He provided me with invaluable perspectives that elevated my understanding

of the problems in the clinical domain. I am also grateful for Lori Gardi and Dr. David Tessier for being very helpful with the work related to the laboratory prototype of the biopsy system. Lori integrated and tested the new software solutions in the biopsy system and always willing to help with new experiments and protocols. David managed the clinical trials in an efficient manner and assisted with many daily activities in the lab. I would also like thank Ren Zhao for his help with the GPU implementation. I was also fortunate to work with Dr. Jing Yuan including many brainstorming sessions where he shared his knowledge and expertise in optimization algorithms applicable to image registration problems.

There are many individuals in Dr. Fenster's and Dr. Ward's labs who need to be recognized for their contributions to my research as well as the companionship that made my stay during the lab a memorable one. My sincere gratitude goes to Vaishali Karnik, Dr. Cesare Romagnoli, Igor Gyackov, Dr. Chandima Edirisinghe, Dr. Eranga Ukwatta, Dr. Jeremy Cepek, Eli Gibson, Hamid Neshat, Bon Ryu, Yue Sun, Dr. Wu Qiu, Dr. Derek Cool, Peter Martin, Sarah Mattonen, Yiwen Xu, Mehrnoush Salarian, Jessica Kishimoto, Dr. Harish Sharma, Maysam Shahedi, Jacques Montreuil, Kevin Barker, Dr. Suha Ghoul, Dr. Bahram Marami, Manale Saikaly, Matt Gravett, Matt Kramers, Tom Hrinivich and many other colleagues in different labs at the Robarts Research Institute and Western University who continuously supported me at multiple stages during my graduate studies. Finally, I would like to thank my parents, my siblings and other extended family and friends for their incredible support and encouragement along every step during this journey.

Table of Contents

Abstract	ii
Co-Authorship	iv
Table of Contents	viii
List of Tables	xii
List of Figures	xiii
List of Abbreviations	xviii
Chapter 1. Introduction	1
1.1 Prostate cancer and its prevalence.....	3
1.2 Prostate cancer diagnosis	6
1.2.1 Digital rectal examination (DRE)	6
1.2.2 Prostate specific antigen (PSA) test.....	6
1.2.3 Prostate biopsy	7
1.3 Prostate cancer imaging	10
1.3.1 Ultrasound imaging.....	10
1.3.2 Computed tomography (CT) and nuclear imaging	13
1.3.3 MR imaging	13
1.4 3D-guided prostate biopsy systems.....	16
1.4.1 Direct MR-guided biopsy systems.....	17
1.4.2 MR-TRUS fusion biopsy systems	19
1.5 Challenges in 3D-guided biopsy systems	21
1.6 Image-based registration techniques	24
1.7 Image registration accuracy required for the clinical application	26
1.8 Hypothesis.....	27
1.9 Objectives.....	27
1.10 Thesis outline	28
1.10.1 Chapter 2 - Quantification of prostate deformation due to needle insertion during TRUS-guided biopsy: Comparison of hand-held and mechanically stabilized systems	28
1.10.2 Chapter 3 - 2D-3D rigid registration to compensate for prostate motion during 3D TRUS-guided biopsy	29
1.10.3 Chapter 4 – Evaluating the utility of intra-procedural 3D TRUS image information in guiding registration for displacement compensation during prostate biopsy.....	31
1.10.4 Chapter 5 – Robust 2D-3D registration optimization to motion compensation using learned prostate motion data	33
References	34

Chapter 2. Quantification of prostate deformation due to needle insertion during TRUS-guided biopsy: Comparison of hand-held and mechanically stabilized systems	46
2.1 Introduction	46
2.2 Method	49
2.2.1 Data Acquisition	49
2.2.2 Image registration	51
2.2.3 Image registration validation	53
2.2.4 Quantification of deformation.....	54
2.3 Results	63
2.3.1 Image registration validation	63
2.3.2 Quantification of deformation.....	63
2.4 Discussion	69
2.4.1 Image registration validation	69
2.4.2 Quantification of deformation.....	70
2.4.3 Limitations	72
2.5 Conclusion	74
References	77
Chapter 3. 2D-3D rigid registration to compensate for prostate motion during 3D TRUS-guided biopsy	79
3.1 Introduction	79
3.2 Materials and methods	84
3.2.1 Data acquisition	84
3.2.2 2D-3D registration – biopsy protocol	85
3.2.3 Incremental 2D-3D registration for continuous intra-biopsy motion compensation	88
3.2.4 2D-3D registration – probe pressure protocol	88
3.2.5 Validation.....	89
3.2.6 GPU implementation	93
3.2.7 Correlation between image similarity metric and misalignment	93
3.2.8 TRE as a function of distance to the probe tip.....	94
3.3 Results	95
3.3.1 Validation: biopsy protocol data	95
3.3.2 Validation: probe pressure protocol data	98
3.3.3 Speed of execution.....	100
3.3.4 Correlation between image similarity measure and misalignment	100
3.3.5 TRE as a function of distance to the probe tip.....	104
3.4 Discussion	104
3.4.1 Accuracy of registration.....	104
3.4.2 Change of TRE with time during biopsy	106
3.4.3 Probe pressure protocol.....	107
3.4.4 Correlation between similarity metric and TRE	108
3.5 Conclusions	108
References	110

Chapter 4. Evaluating the utility of intra-procedural 3D TRUS image information in guiding registration for motion compensation during prostate biopsy	112
4.1 Introduction	112
4.2 Materials and methods	115
4.2.1 Materials	115
4.2.2 Image registration	117
4.2.3 Registration error measurement	120
4.2.4 Experimental methods	120
4.2.5 TRE for different fixed image configurations	121
4.2.6 TRE for base, mid-gland and apex regions.....	122
4.3 Results	123
4.3.1 TRE for different fixed image configurations	123
4.3.2 TRE for base, mid-gland and apex regions.....	126
4.4 Discussion	128
4.4.1 TRE for different fixed image configurations	130
4.4.2 TRE for base, mid-gland and apex regions.....	131
4.4.3 Limitations	131
4.5 Conclusion	133
References	134
Chapter 5. Robust 2D-3D registration optimization to motion compensation using learned prostate motion data	137
5.1 Introduction	137
5.2 Materials and Methods	139
5.2.1 Data acquisition	139
5.2.2 Modelling rigid prostate motion	140
5.2.3 Robust search strategy during registration optimization	142
5.2.4 Experiments	146
5.3 Results	146
5.4 Discussion	150
5.5 Conclusions	152
References	153
Chapter 6. Conclusions and Directions for Future Work	155
6.1 Conclusions	155
6.2 Suggestions for future work	159
6.2.1 Applications in ongoing clinical studies	159
6.2.2 Applications in other clinical procedures	160
6.2.3 Applications in image-based tracking.....	161
References	163
Appendix A	164
A.1 Permission to reproduce previously published material in Chapters 2, 3 and 4 .	164
A.2 Permission to reproduce previously published material in Chapters 5	165

List of Tables

Table 1.1: TNM staging of prostate cancer.....	8
Table 1.2: A comparison of some commercially available 3D TRUS-guided biopsy systems.....	20
Table 2.1: Comparison of TRE before and after registration for each tested registration method. Registration 1 captures tissue motion during needle insertion and biopsy gun firing, registration 2 captures needle insertion only, and registration 3 captures biopsy gun firing only.....	63
Table 3.1: Errors before and after probe protocol registration.	99
Table 4.1: Mean execution times for registration with different fixed image configurations	126
Table 4.2: RMS \pm std TREs for registrations at different sextant probe positions.	127
Table 5.1: Comparisons of performance before and after registration with new and initial methods, and FRE.....	147
Table 5.2: Comparison of performance for registrations with TRE >5 mm with the initial approach.....	148

List of Figures

Figure 1.1: (a) Anatomical position of the prostate relative to the neighboring organs in a sagittal view. (b) Primary anatomic regions of the prostate in a sagittal view.	3
Figure 1.2: Central zone (CZ), peripheral zone (PZ), transition zone (TZ), anterior fibromuscular stroma (AZ) constituting the zonal anatomy of the prostate in a sagittal view.....	5
Figure 1.3: The appearance of (a) a calcification, and (b) a cyst in a 2D TRUS image..	12
Figure 1.4: Multiparametric MR images of the prostate with suspicious region for cancer indicated by the yellow arrow: (a) T2-weighted image showing a region with hypo intensity. (b) DCE image not showing any contrast for this patient in the suspicious area.	14
Figure 2.1: Mechanically assisted 3D TRUS-guided biopsy system. The biopsy gun is retained in a clip and the needle is coupled to the TRUS probe using a needle guide. A spring-based counter balancing system maintains probe position and orientation even when the physician removes his hand from the probe.	50
Figure 2.2: Images in a biopsy sequence, and the names used for the three indicated registrations throughout this paper. The first image occurs immediately prior to the physician's insertion of the biopsy needle. The second image occurs immediately prior to firing the biopsy gun, and the third image occurs immediately after the biopsy gun has been fired. The dotted curves indicate portions of the prostate boundary that interact with the needle, which lies between the two solid vertical segments in the second and third images; note the deformation at the lower piercing point.	51
Figure 2.3: Overall process used in this work. The moving image (from an earlier time point) is registered to the fixed image (from a later time point) using non-rigid registration. This yields a deformation vector field that is used to quantify the underlying motion of the tissue. The error in the non-rigid registration algorithm is measured by calculating a TRE based on corresponding intrinsic fiducial markers. Measurements, incorporating the TRE, are then taken from the deformation vector field to characterize the underlying motion of the prostate tissue in response to the insertion of the biopsy needle and firing of the biopsy gun.....	53
Figure 2.4: (a) Deformation vector field magnitude with prostate boundary and needle location indicated. (b) Lateral (x) components of the deformation field. (c) Axial (y) components of the deformation field. The needle axis lies between the vertical white line in each image.....	53
Figure 2.5: Calcifications used to validate the registration algorithms, indicated by arrows.....	54
Figure 2.6: Diagram depicting a prostate contoured on a 2D TRUS image with the needle axis As to the left of the probe, as in all of our images. The perpendicular	

distance DA of a point P to the needle axis is shown. The lower piercing point l_s is indicated, as is the distance DI between P and the lower piercing point..... 60

Figure 2.7: Diagram depicting prostate anatomy in a sagittal view, indicating the peripheral zone (PZ), central zone (CZ), transition zone (TZ), and anterior zone (AZ). Three biopsy targets are shown as A, B, and C. The biopsy needle enters the prostate on the posterior side by penetrating the rectal wall, as shown..... 61

Figure 2.8: Deformation versus distance to the needle axis. Dashed curve: the signed mean of the deformation ($\bar{D}_r(P_d^A)$). Dotted curve: the 95% confidence interval around the tissue deformation ($\tilde{\sigma}_r(P_d^A)$). Solid curve: the 95% confidence interval incorporating the TRE ($\sigma_r(P_d^A)$). (a, b): registration 1, (c, d): registration 2, (e, f): registration 3. (a, c, e): hand held, (b, d, f): mechanically assisted..... 65

Figure 2.9: Deformation versus distance to the lower piercing point. Dashed curve: the signed mean of the deformation ($\bar{D}_r(P_d^l)$). Dotted curve: the 95% confidence interval around the tissue deformation ($\tilde{\sigma}_r(P_d^l)$). Solid curve: the 95% confidence interval incorporating the TRE ($\sigma_r(P_d^l)$). (a, b): registration 1, (c, d): registration 2, (e, f): registration 3. (a, c, e): hand held, (b, d, f): mechanically assisted..... 66

Figure 2.10: Lateral-axial decompositions of the 95% confidence intervals shown in Figures 8 and 9, for registration 1. (a, b): Deformation versus distance to the needle axis. Solid curve: the 95% confidence interval around the tissue deformation incorporating the TRE ($\sigma_r(P_d^A)$). Dashed curve: the lateral (x) component of this confidence interval ($\sigma_1^x(P_d^A)$). Dotted curve: the axial (y) component ($\sigma_1^y(P_d^A)$). (c, d): Deformation versus distance to the lower piercing point. Solid curve: the 95% confidence interval around the tissue deformation incorporating the TRE ($\sigma_r(P_d^l)$). Dashed curve: the lateral (x) component of this confidence interval ($\sigma_1^x(P_d^l)$). Dotted curve: the axial (y) component ($\sigma_1^y(P_d^l)$) (a, c): hand held, (b, d): mechanically assisted..... 68

Figure 2.11: Deformation as a function of lateral position of the needle relative to the prostate, for registration 1. The distance to the left edge of the prostate is shown on the horizontal axis (0 = left edge, 0.5 = middle, 1 = right edge). The vertical axis shows the width of the 95% confidence interval on the tissue deformation within a region lying 5 mm on either side of the needle axis ($\sigma_1(P_{5\text{mm}}^{AR})$). The best fit line is plotted, showing a weak negative relationship ($r = -0.17$)..... 69

Figure 3.1: 2D-3D registration workflow 86

Figure 3.2: Sample fiducials identified..... 91

Figure 3.3: TRE before registration, after registration and after continuous registration every second for each biopsy in prostate biopsy protocol..... 96

Figure 3.4: Images before and after registration immediately prior to taking a biopsy sample. Left column: Real-time 2D TRUS images. Middle column: Corresponding images before registration assuming no prostate motion (from the transformation

given by the mechanical tracking system). Right column: Corresponding images after registration.	97
Figure 3.5: TRE as a function of time elapsed from the start of the biopsy. (a) TRE before registration. (b) TRE after registration. (c) TRE after registering the images acquired every second.	97
Figure 3.6: Histograms for TRE before and after registration for probe pressure protocol data. Left: TRE distribution before registration Middle: TRE distribution after registration. Right: TRE distribution with the best rigid alignment for the identified fiducials.	99
Figure 3.7: TRE of each fiducial as a function of distance to the registration plane. The black line represents the least-square fit to the scattered points.	99
Figure 3.8: TRE as a function of metric value during the optimization. Initial points (circles), converged (squares) and converging points (crosses).	100
Figure 3.9: TRE distributions before registration, during convergence and after registration.	100
Figure 3.10: Mean and standard deviations of normalized cross-correlation values for 16 image pairs of eight patients in the six-degrees-of-freedom transformation space, one degree-of-freedom varying at a time. The zero location in the x-axis corresponds to real-time 2D-TRUS frame.	102
Figure 3.11: Normalized cross-correlation values for a single image pair of a biopsy for 3 patients (each biopsy represented by a separate line pattern) in the six-degrees-of-freedom transformation space, one degree-of-freedom varying at a time. The zero location in the x-axis corresponds to real-time 2D-TRUS frame.	103
Figure 3.12: TRE as a function of distance to the probe tip.	104
Figure 4.1: (a) Coronal view (from the posterior perspective of the TRUS probe) of relative positions of the probe tip during image acquisition (B: baseline, 1-6: sextant locations) (b) Transverse view showing the necessary reorientation of the probe to acquire images at baseline and targets 2 and 5.	116
Figure 4.2: Fixed image configurations used in this paper: notation and schematics of planes from a probe-axis view.	118
Figure 4.3: Overall workflow in methods and validation.	119
Figure 4.4: Distribution of manually identified fiducials used for registration validation. Each fiducial is shown with its Anterior/Posterior (A/P), Left/Right (L/R) and Inferior/Superior (I/S) position within the normalized prostate in which the boundaries extend from 0 to 1 along each direction.	121
Figure 4.5: Example of the identified fiducials for three pairs of images. Arrows point to homologous fiducial pairs in each row. Baseline images with the fiducials are shown in the left and the sextant images of the same patient with corresponding fiducials are shown in the right.	122

Figure 4.6: TRE histograms for registrations using different fixed images, with the RMS \pm std TRE shown in the top left of each histogram. To provide context for the TRE distributions, row 1, column 1 shows the error distribution prior to registration and row 2, column 1 shows the error distribution after optimal rigid registration using the fiducials (FRE).....	123
Figure 4.7: Comparison of TRE distribution parameters for different fixed image configurations.	125
Figure 4.8: Histogram of TRE differences between I_0 and I_{0-179}	125
Figure 4.9: Corresponding transverse 2D planes from; (a) fixed image, (b)-(d) transformed moving image after registration using the fixed image configurations as indicated, (e) moving image before registration.	126
Figure 5.1: Probe positions during image acquisition shown relative to (a) coronal view (b) axial view.....	140
Figure 5.2: Diagram depicting the improvement (i.e., decrease) of the condition number (λ_2/λ_1) of a 2D objective function by scaling the search space according to the eigenvalues (λ_2, λ_1) of the matrix A of the objective function. (a) Initial search space of the objective function. (b) Situation after the search space is scaled according to λ_2, λ_1 . Black ellipsoids/circles show the function iso-contours, with larger circles/ellipses indicating less optimal values of the objective function. The red circle shows an example initial search location and the red arrow shows a typical Powell's method initial search direction.....	143
Figure 5.3: Scaling the search space according to the eigen values (λ_2, λ_1) of the covariance matrix C of the observed motion vectors. (a) Initial distribution of the motion vectors in the search space. (b) After the search space is scaled according to λ_2, λ_1 in the principal directions. The points representing the observed motion vectors (i.e., objective function optima). The red circle shows an example initial search location and the red arrow show a typical Powell's method initial line search direction.	145
Figure 5.4: TRE histograms (a) TRE before registration. (b) TRE after registration without using learned prostate motion characteristics. (c) TRE after registration using the proposed method.	147
Figure 5.5: Images before and after registration for 5 patients. Top row: extracted 2D images (I_{pi}). Middle row: corresponding frames from the registered I_B . Bottom row: corresponding frames before registration obtained from I_B after tracking the probe.	148
Figure 5.6: Comparisons of TREs in the two methods. The gray circles indicate biopsies for which the TRE from the initial method was ≤ 5 mm. The coloured symbols indicate biopsies for which the TRE from the initial method was > 5 mm. The coloured squares indicate TREs from the initial method, and the coloured triangles indicate TREs from the new method. Upward-pointing triangles show cases where the TRE from the new method was larger than the TRE from the initial method. Downward-pointing triangles indicate cases where the TRE from the new	

method was smaller than the TRE from the initial method. A symbol of a given colour corresponds to a specific registration. 149

Figure 5.7: Comparison of NCC at convergence in the two methods. The gray circles indicate biopsies for which the TRE from the initial method was ≤ 5 mm. The coloured symbols indicate biopsies for which the TRE from the initial method was > 5 mm. The coloured squares indicate NCCs from the initial method, and the coloured triangles indicate NCCs from the new method. Downward-pointing triangles show cases where the NCC from the new method was smaller than the NCC from the initial method. Upward-pointing triangles indicate cases where the NCC from the new method was larger than the NCC from the initial method. A symbol of a given colour corresponds to a specific registration..... 150

List of Abbreviations

2D	Two-Dimensional
3D	Three-Dimensional
ADC	Apparent Diffusion Coefficient
AZ	Anterior Fibromuscular Stroma
BPH	Benign Prostatic Hyperplasia
CEUS	Contrast-enhanced Ultrasound
CT	Computed Tomography
CUDA	Compute Unified Device Architecture
CZ	Central Zone
DCE	Dynamic Contrast-Enhanced
DRE	Digital Rectal Examination
EM	Electromagnetic
ESUR	European Society of Urogenital Radiology
FEA	Finite Element Analysis
FLE	Fiducial Localization Error
FRE	Fiducial Registration Error
GPU	Graphics Processing Unit
MRI	Magnetic Resonance Imaging
MRSI	Magnetic Resonance Spectroscopy Imaging
NCC	Normalized Cross-Correlation
PET	Positron Emission Tomography
PI-RADS	Prostate Imaging and Reporting Data System
PSA	Prostate Specific Antigen
PZ	Peripheral Zone
RCM	Remote Center of Motion
RMS	Root Mean Square
SPECT	Single Photon Emission Computed Tomography
SSD	Sum-of-Squared Difference
TRE	Target Registration Error

TRUS Transrectal Ultrasound

TZ Transition Zone

Chapter 1.

Introduction

Prostate biopsy is the clinical standard for prostate cancer diagnosis, which is a procedure usually performed under two-dimensional (2D) transrectal ultrasound (TRUS) guidance. Unfortunately, most early stage prostate cancers are not visible on ultrasound, so the procedure is routinely performed in a systematic, but ultimately random fashion, where biopsy cores are collected following a standard sextant plan with the aim of sampling any tumors that are occult on ultrasound [1]. The procedure suffers from a false negative rate as high as 30% due to the lack of visible targets [2]. Prostate magnetic resonance imaging (MRI) is more sensitive to detection of small lesions and its use for pre-biopsy target identification is rapidly growing [3-5]. With the objective of improving the cancer detection rate during biopsy, systems have been developed to perform a targeted biopsy by fusing pre-biopsy MRI with 3D TRUS [6-11]. In many such systems, prior to performing biopsy, suspicious lesions delineated as targets in a pre-biopsy MR image are mapped to the static baseline 3D TRUS image acquired at the beginning of the biopsy session [12-15]. Biopsy is subsequently performed, targeting each suspicious lesion using the live 2D TRUS images acquired while tracking the ultrasound probe position and orientation relative to the baseline 3D TRUS image.

Prostate biopsy is an outpatient procedure that is performed when the patient is awake in the lateral decubitus position under local anaesthesia. We have observed that patient discomfort can lead to intermittent prostate motion/displacement during the procedure. TRUS probe pressure is another source of prostate motion, when the

physician maneuvers the probe to reach different regions within the prostate; although the prostate is attached to the surrounding tissue, it can move as a unit within the pelvis in response to probe pressure at different prostate locations [16]. The variability in applied TRUS probe pressure could also deform the prostate, particularly in the posterior region. In a targeted approach to biopsy where suspicious locations for cancer need to be sampled, intermittent prostate motion during the procedure could limit accuracy in maintaining the correspondence between live TRUS images and the targets defined in the baseline 3D TRUS image. Identification of the errors due to prostate motion and the development of accurate and fast registration methods to compensate for patient and prostate motion during the procedure are therefore helpful to improve needle targeting accuracy of 3D TRUS-guided biopsy systems.

The focus of this thesis is to quantify and compensate for the errors due to patient and prostate motion during biopsy in the mechanically assisted 3D TRUS-guided biopsy system [8] previously developed in our lab. This would help to detect clinically significant tumours at an early stage using the emerging MR-targeted, 3D TRUS-guided approach to performing biopsy and could impact the overall prostate cancer detection rate from biopsy, leading to fewer biopsy sessions, earlier diagnosis, and appropriate treatment selection. The remainder of the chapter describes the current status in prostate cancer prevalence, the available diagnostic methods, 3D-guided biopsy systems and how image-based registration could help improve their clinical outcomes in practice with hypothesis and specific objectives of the thesis.

1.1 Prostate cancer and its prevalence

Prostate cancer is the most commonly diagnosed non-skin cancer among Canadian men contributing to 25% (~24, 000) of all estimated new cancer cases in 2013 [17]. It is also reported to be the third largest contributor to estimated cancer deaths among Canadian men in 2013, representing 10% of all deaths [17]. Approximately 1 in 7 men will be diagnosed with prostate cancer during his lifetime and 1 in 37 will die of this disease. Prostate cancer incidence increases with age, with 34% of men in their 50s and 70% of the men at the age 80 showing histologic evidence of prostate cancer [18]. Prostate cancer exhibits a wide variation of natural history, with the existence of clinically indolent tumours in some men and aggressive, metastatic, lethal tumours with considerable morbidity in others. Therefore, the ability to differentiate between indolent and aggressive disease during the diagnosis is paramount for successful prostate cancer management in the population.

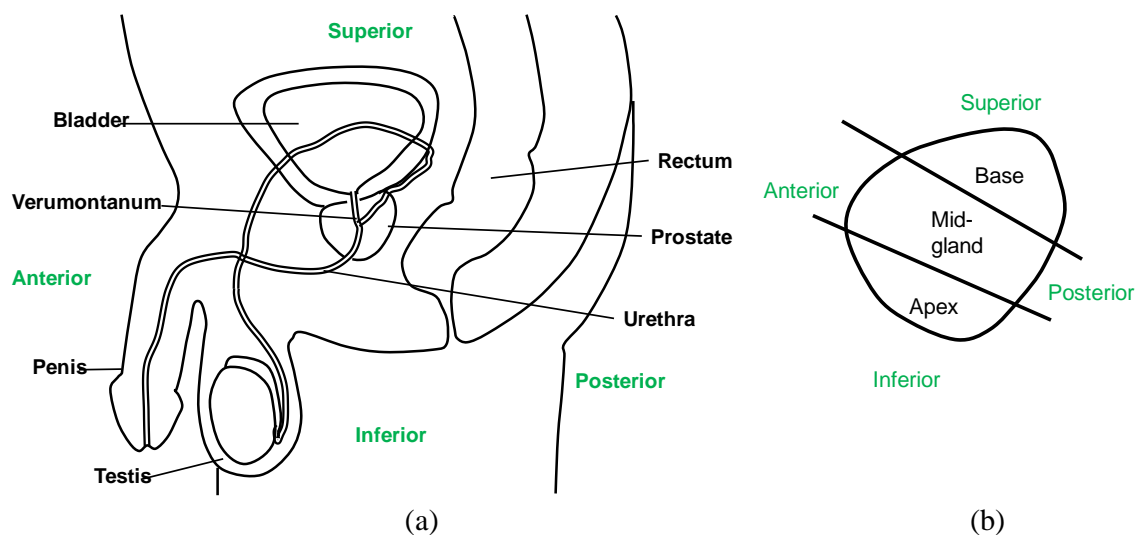


Figure 1.1: (a) Anatomical position of the prostate relative to the neighboring organs in a sagittal view. (b) Primary anatomic regions of the prostate in a sagittal view.

The prostate in a healthy adult male is a walnut sized organ, approximately 20 cm³ in volume, sitting on the pelvic floor, surrounding the urethra, and proximal to the bladder neck (Figure 1.1(a)). The base, the mid-gland and the apex constitute the three primary anatomic regions of the prostate (Figure 1.1(b)). The superior region of the prostate proximal to the bladder neck is identified as the base, while the inferior region proximal to the urogenital diaphragm is identified as the apex. The prostate has also been divided anatomically into four different lobes: (1) anterior lobe, (2) posterior lobe, (3) lateral lobes, and (4) median lobe. McNeal [19-21] proposed a zonal model, which is widely used in pathology, to describe prostate glandular anatomy, dividing the prostate into three distinct zones: (1) central zone; (2) peripheral zone; and (3) transition zone (Figure 1.2). The central zone (CZ) is a wedge-shaped volume containing about 25% of the glandular tissue of the prostate, in the region between the bladder neck to verumontanum. The peripheral zone (PZ) is the largest zone lying distal to the central zone containing about 70% of the glandular tissue within the prostate. The transition zone (TZ) comprises 5% to 10% of prostate glandular tissue lying on either side of the urethra just above the ejaculatory duct openings. The anterior fibromuscular stroma (AZ) is another portion consisting of approximately one-third of the prostate organ. It is composed of non-glandular tissue [21], although some consider it to be the fourth zone [22].

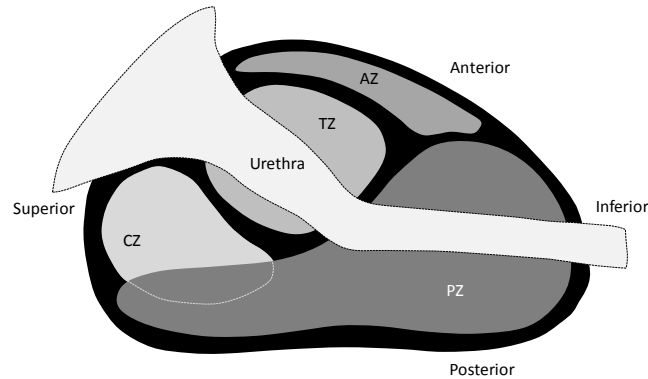


Figure 1.2: Central zone (CZ), peripheral zone (PZ), transition zone (TZ), anterior fibromuscular stroma (AZ) constituting the zonal anatomy of the prostate in a sagittal view.

Most men tend to have some enlargement of the prostate with aging, sometimes causing a common urologic condition known as benign prostatic hyperplasia (BPH). This enlargement affects primarily the transition zone, occurring above the level of verumontanum. Since the prostate wraps around the urethra, prostate enlargement can obstruct the flow of urine. Therefore, urinary obstructive symptoms such as urinary retention, frequent urination and nocturnal voiding are possible with BPH patients. However, BPH patients do not show increased risk of developing prostate cancer [23].

BPH is not the only cause of prostate growth in aging men. Prostate cancer tumours could cause growth and create hard nodules within the prostate. Prostate cancers can be multi focal, and about two thirds are found in the peripheral zone, causing an asymmetric growth of the prostate. Unlike BPH, however, early stage prostate cancers are asymptomatic, making timely diagnosis very challenging. Although current understanding of what causes prostate cancer is limited [24], endogenous factors such as age, family history and ethnicity have shown association with cancer risk [25].

1.2 Prostate cancer diagnosis

1.2.1 Digital rectal examination (DRE)

Early detection of prostate cancer is critical to devise successful treatment methods in order to reduce morbidity and mortality. Since early stage prostate cancer is asymptomatic, there are screening tests advocated with the goal of improving diagnostic outcomes among the average to high-risk population. Digital rectal examination (DRE) is the first screening method introduced as early as in 1905, in which the physician palpates the prostate with a gloved finger inserted into the patient's rectum. The physician examines for discrete hard nodules, prostate asymmetry and firmness as characteristics that are suspicious for cancer. Although this is an easy, inexpensive test, it suffers from poor sensitivity with cancer detection rates $< 50\%$, missing most early stage tumours [26]. Most cancers were detected at an advanced stage with this method and the diagnostic decisions were prone to high inter-examiner variability [27].

1.2.2 Prostate specific antigen (PSA) test

The serum level of prostate specific antigen (PSA) in the blood is another screening test introduced in the late 1980s. The probability of cancer increases with concentration of PSA in blood, with the most commonly used threshold being 4 ng/ml for prostate cancer detection. Although PSA has high sensitivity for cancer detection, the PSA level in the blood can increase due to conditions unrelated to cancer, such as BPH, infection or inflammation, resulting in poor specificity of the test [28, 29]. Although the use of PSA screening since 1985 has impacted the patterns in cancer incidence and mortality [30], the poor sensitivity of screening tests for detecting cancer and the challenges in

differentiating between indolent and aggressive disease could potentially result in overdiagnosis and overtreatment. Currently, the American Cancer Society recommends that average-risk, asymptomatic men at age 50 to make an informed decision with the physician to be screened for prostate cancer [31]. The clinical standard for definitive diagnosis of prostate cancer is prostate biopsy.

1.2.3 Prostate biopsy

Patients with elevated PSA or abnormal DRE are referred to prostate biopsy. Needle biopsy remains the clinical standard for prostate cancer diagnosis, a procedure performed with the objective of detecting aggressive tumours that could cause potential harm. It is an outpatient procedure conventionally performed using 2D transrectal ultrasound (TRUS) guidance. It is usually performed when the patient is in left lateral decubitus position with local or topical anesthesia. The physician samples tissue locations following a sextant template biopsy scheme using a spring-loaded 18-gauge biopsy needle. Several systematic biopsy schemes have been proposed [1, 32, 33] and usually 6-12 biopsy cores are taken during the procedure under these schemes. The tissue samples are then processed and examined by urological pathologists in search for any histological abnormalities and to assess the severity and extent of the disease.

Assessing the extent of the disease is a vital component before devising appropriate treatment methods. The most commonly used method to categorize the disease extent is the TNM staging system [34]. According to this scheme, cancer is classified into four major stages (T1 – T4) evaluating three main areas: (1) primary tumour, (2) metastatic disease, and (3) involvement of nearby lymph nodes. Table 1.1 shows the diagnostic criteria for classification of the different stages of cancer. Prostate

biopsy results, prostate cancer imaging and manual palpation of the prostate could aid in determining the disease stage during diagnosis. TRUS has been the conventional and most widely used imaging modality in examining the extent of hypoechoic regions in the prostate for suspicion of cancer [35]. However, MRI has recently shown promise, with improved sensitivity (73-86%) and specificity (77-94%) in determining cancer stage [36, 37].

Table 1.1: TNM staging of prostate cancer

Stage	Criteria
T1	Tumour at incidental stage, but impalpable and not detectable by imaging
T2	Locally confined palpable tumour
-T2a	Tumour exists in half or less than half of one of the two lobes
-T2b	Tumour exists in more than half of only one lobe
-T2c	Tumour exists in both the lobes
T3	Tumour has spread through the prostatic capsule
T4	Tumour has invaded to other neighboring organs

In measuring the severity of prostate cancer, the Gleason grading system [38] is the most widely accepted and commonly used method. In this system, the glandular pattern of the tumour in biopsy cores is identified and assigned a grade from 1 to 5 at a relatively low magnification level. The scoring is based on the differentiation of prostate cancer cells, with 1 the most differentiated and 5 the least differentiated. Both the primary tissue grade – score given to the most prevalent pattern containing the tumour –, and the secondary grade – the score given to the second most prevalent pattern containing the tumour – are assessed independently and summed to get the overall Gleason score. Thus, the Gleason score can range from 2 (1+1) to 10 (5+5), with 2 being the lowest grade given to insignificant disease and 10 being the highest grade given to advanced disease. A Gleason score of 7 (4 +3) indicates that the patient has the most

common glandular pattern with a score 4 and the second most common pattern with a score 3. A Gleason score of 7 (4 + 3) is less desirable than a score of 7 (3 + 4), since the most common glandular pattern is less aggressive in the latter.

Based on the results of PSA, staging and grading, cancer patients can be classified into three risk groups [39-41]. According to the classification by D'Amico et al. [41], patients with Gleason score 8-10, stage \geq T2c or PSA >20 ng/ml are considered high risk, with aggressive tumours and advanced disease. While these patients are not recommended for localized therapy, the typical treatment options are radical prostatectomy and external beam radiotherapy. Patients with Gleason score 7, stage T2b or PSA 10.1-20 ng/ml are considered to be intermediate risk. These patients with organ confined disease are amenable to be treated with localized treatment methods such as focal laser ablation and high intensity focused ultrasound. On the other hand, the patients with Gleason score 2-6, stage T1-T2a, and/or PSA <10 ng/ml are considered to be low risk and clinically insignificant.

The prostate biopsy results play a critical role in differentiating between aggressive and indolent disease and in selecting treatment options for tumours that need attention. While underdiagnosis and undertreatment of aggressive cancers could cause lethal effects on patients, overdiagnosis and overtreatment could lead to undesirable health outcomes like urinary incontinence and erectile dysfunction. Unfortunately, the “blind” approach to systematic prostate biopsy has high false negative rates in the range 10-30% [32, 42-44], leaving uncertainty in the generated results during its role as the diagnostic tool for prostate cancer. As a consequence, clinicians have to base their decisions on evidence that is inconclusive and repeat biopsies might need to be

performed to increase the certainty of the diagnosis. For example, an increasing trend in PSA level could lead to repeat biopsy in patients who have already undergone prior negative biopsies. Patients who underwent a second biopsy session have reported cancer detection rates of 19%, [45] indicating the limitations of the conventional systematic biopsy scheme. In order to improve the cancer detection rates, saturation biopsy schemes have been proposed by increasing the number of biopsy cores to the range 15-31 [46-48]. However, the high probability of these schemes to detect clinically indolent cancers, increased cost and morbidity have limited their adaptation as the mainstay approach to biopsy in comparison to the sextant approach with 6-12 cores. In fact, a subsequent prospective study [49] reported no significant difference in terms of cancer detection rate in saturation and sextant approaches.

1.3 Prostate cancer imaging

1.3.1 Ultrasound imaging

Ultrasound evaluation of the prostate could be achieved via transabdominal, transrectal or transperineal access. TRUS is the most common approach used in prostate examinations to detect pathology and calculation of prostate volume [50]. The transrectal approach provides better access to peripheral zone tumours in prostate posterior, where 70-80% of the prostate cancers arise [51] and improves the ability to direct needles into regions of interest during biopsy procedures.

A transducer containing transmitting elements, electrodes, and protective face generates ultrasound waves [52]. High frequency ultrasound transducers within the range 5-10 MHz are used for TRUS imaging. Commercially available TRUS probes are either

side-firing or end-firing, with end-firing probes more suitable for image guidance during trans-rectal prostate biopsy [53]. Some probes come with enhanced functionality to simultaneously acquire dual-orthogonal (transverse and sagittal) planes or full 3D imaging. While the acquisition rate is 10-20 frames per second using single-plane 2D-TRUS probes, 3D image acquisition could take up to 5 s using enhanced probes.

Ultrasound waves are reflected as they penetrate through different tissues and anatomical structures. The degree of reflectance depends on the acoustic impedance between two layers of tissue. Structures that reflect most of the ultrasound waves appear as bright regions in images while the structures that reflect the least appear as dark regions. Relative to the medium-gray echogenicity of the peripheral zone, structures that appear brighter are termed *hyperechoic* and those that appear darker are termed *hypoechoic*. The pubic bone and prostatic calcifications are examples of hyperechoic anatomical structures that appear bright on ultrasound. On the other hand, fluid-filled structures like seminal vesicles, vas deferens, ejaculatory ducts, cysts, and the gall bladder appear hypoechoic in ultrasound. Figure 1.3 shows examples of the appearance of a calcification and a cyst in 2D TRUS images. The boundaries between zonal anatomical structures can often be identified in ultrasound images as hypoechoic linear demarcations. Prostate cancer in the peripheral zone is typically considered to appear as hypoechoic on TRUS [54], while transition zone cancers have shown more heterogeneity in appearance. However, elusive nature of cancer appearance in TRUS has posed many challenges in using it as an imaging modality to detect suspicious regions for prostate cancer [55, 56] and has been reported with low sensitivity (35-91%) and specificity (24-81%) values in prostate cancer screening [57-61].

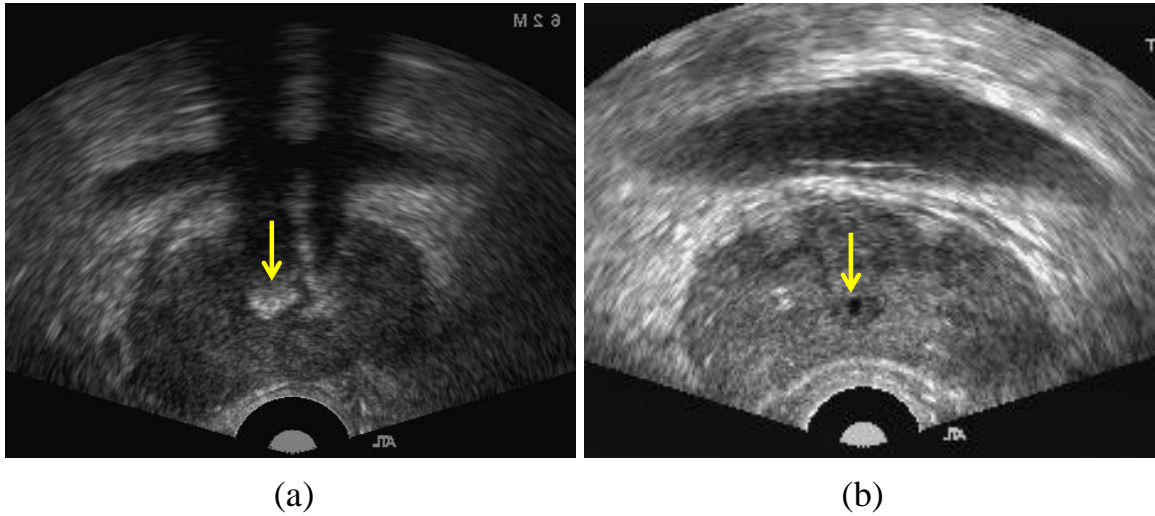


Figure 1.3: The appearance of (a) a calcification, and (b) a cyst in a 2D TRUS image.

With the objective of improving cancer detection using ultrasound imaging modality and providing guidance to suspicious target regions during biopsy, several enhanced techniques have been investigated. Color and power Doppler ultrasound imaging has been applied to evaluate blood flow and vascularity within the prostate tissue [62, 63]. Due to the formation of new vessels in tumours, cancerous tissues tend to demonstrate hypervascularity [64]. Contrast-enhanced ultrasound (CEUS) is another approach to improve tumour visibility in imaging where encapsulated gas microbubbles are injected into the small vessels to improve their ultrasound reflectivity in highly vascular regions formed potentially due to cancer [65, 66]. Elastography is another ultrasound-based imaging technique that is currently being investigated to detect tumours using mechanical properties of tissues. Since the tissue stiffness properties differ in cancerous tissues, elasticity imaging techniques could potentially be used to identify them in real time [67]. Although some of these ultrasound-based imaging methods are the subject of active research, the benefits of such approaches in improving clinical outcomes over systematic biopsy have not yet been proven [68, 69].

1.3.2 Computed tomography (CT) and nuclear imaging

Other modalities like CT, positron emission tomography (PET) and single photon emission computed tomography (SPECT) have been used to image the prostate.

However, their use has been primarily focused on radiotherapy planning and prognostic evaluation of metastatic disease. CT images are sometimes acquired for the purpose of determining the cancer stage when it has spread at a macroscopic level to the perineal floor and lymph nodes [70], but are rarely acquired for primary prostate evaluation.

Similarly, PET and SPECT imaging are used in identification of metastatic spread of cancer to the bones.

1.3.3 MR imaging

Although moderate staging performance was observed for images obtained from early MR scanners [71], with recent improvements in signal-to-noise ratio and image quality [72], multi-parametric MR images have shown promise in detecting and localizing prostate cancer. T1-weighted imaging has been demonstrated to be useful in TRUS-guided biopsy hemorrhage artifact detection, but has limited use in prostate cancer imaging due to low contrast. T2-weighted MR is the most widely used sequence for prostate cancer imaging and it can clearly differentiate the prostate zonal anatomy. On T2-weighted images, the typical peripheral zone has high-signal intensity, greater than nearby structures [73]. In prostate cancer, the loss of normal glandular morphology tends to cause regions with low-intensity level. Benign conditions like BPH typically have a nodular appearance on T2-weighted imaging; however, loss of glandular morphology can also cause BPH to appear as a low-intensity signal. Due to these confounding

factors, prostate cancer detection using T2-weighted imaging alone could be challenging [74]. However, different functional MR techniques can be used in combination to improve the differentiation of cancerous tissue.

Diffusion-weighted MR imaging is a functional imaging technique in which proton diffusion properties in water are used to generate image contrast by quantifying the average random motion of hydrogen nuclei within the body. The apparent diffusion coefficient (ADC) quantifies the direction and distance of water molecules due to both perfusion and diffusion within the interpulse time of an applied motion-encoding gradient in MR that cause proton movements and phase shifts. Healthy prostate peripheral zone tissue contains tubular structures that allow abundant diffusion of water molecules in these regions, resulting in high ADC values. Prostate cancer, in contrast, tends to destroy the tubular structures and replace ducts often showing lower ADC values when compared with healthy prostate tissue [75, 76]. However, conditions like BPH and prostatitis could result in lower ADC values, which could limit the ability to make a definitive diagnosis using this information alone [77, 78].

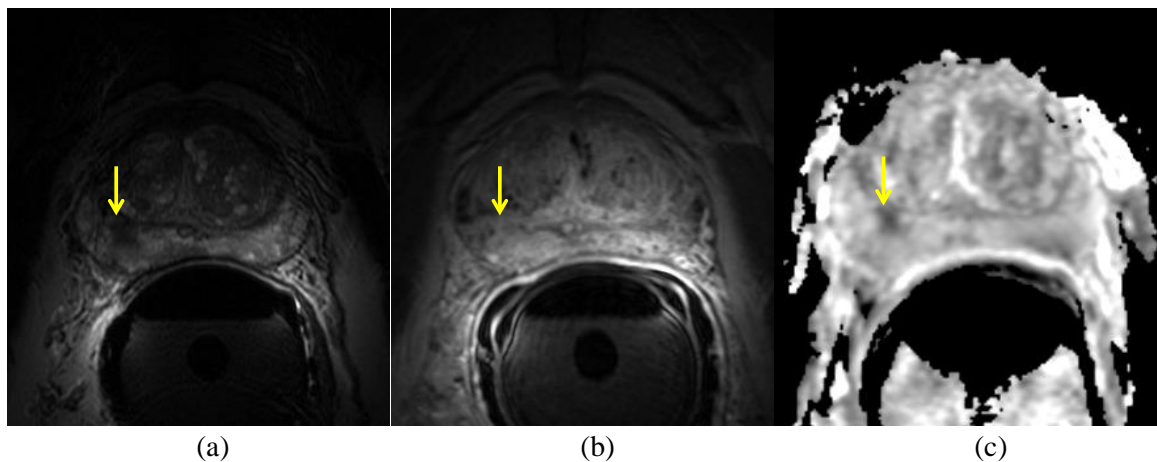


Figure 1.4: Multiparametric MR images of the prostate with suspicious region for cancer indicated by the yellow arrow: (a) T2-weighted image showing a region with hypo intensity. (b) DCE image not showing any contrast for this patient in the suspicious area. (c) ADC map showing a region of hypointensity.

Dynamic contrast-enhanced (DCE) MR imaging is another functional imaging method to aid in the detection of cancerous regions by noninvasively examining tumor angiogenesis. It consists of a series of T1-weighted images acquired successively after injection of a gadolinium contrast agent to evaluate tumour vascular function. Since prostate cancer tumours are highly vascular, a comparison of pre- and post-gadolinium images could be used to identify regions suspicious for prostate cancer [79]. When compared with healthy tissue, prostate cancer tends to show rapid wash-in and wash-out with the contrast agent injection [80]. Magnetic resonance spectroscopy imaging (MRSI) [81], MR elastography [82] and sodium imaging [83] are some other emerging techniques that have the potential to aid prostate cancer detection via imaging.

Developing mechanisms for prostate cancer detection and localization is a non-trivial task considering the biological and pathological complexity of the disease. Although different MR imaging sequences have their strengths and limitations, combination of different techniques could help to mitigate the limitations of individual sequences and help improve the accuracy in making a definitive diagnosis. Figure 1.4 shows the appearance of a suspicious cancer region of a patient in T2-weighted, DCE and DWI images. The European Society of Urogenital Radiology (ESUR) has recently published a report [84] providing guidelines for MRI of prostate cancer based on published evidence and expert opinion. This report recommends the use of a combination of high-resolution T2-weighted images and at least two functional MRI techniques when detecting cancer with a multiparametric MRI examination. The guidelines also include a structured scoring system (Prostate Imaging and Reporting Data System [PI-RADS]) for classification and reporting of tumours during the diagnosis. While the clinical protocols

using multiparametric MRI for prostate cancer are becoming standardized, currently active research is focused on investigation of MR to histopathology correlation to further improve the detection of cancer using *in vivo* imaging [85-88]. Although currently reported sensitivity (73-86%) and specificity (77-94%) results [89-91] for prostate cancer detection in MR imaging does not permit replacement of needle biopsy as the clinical standard of diagnosis, multi-parametric MR has the potential utility in guiding biopsy towards target regions and subsequently could be used in conjunction with biopsy results to make informative assessment during staging and grading of cancer. Detecting cancer using *in vivo* imaging is also beneficial in contouring tumours for localized treatment of intermediate-risk prostate cancer.

1.4 3D-guided prostate biopsy systems

While the standard sextant approach to prostate biopsy under 2D TRUS-guidance usually lacks visible tumour targets, multi-parametric MRI has shown promise in non-invasive detection of cancer. The addition of the MR-detected cancer suspicious regions as targets during biopsy could impact and improve the limited sensitivity and specificity of the conventional sextant template schemes. Aligning the biopsy needle trajectories with the regions identified in MR requires accurate localization of target locations within the 3D anatomy of the prostate. In order to achieve this objective, the physician could initially identify the target locations in MR and then mentally map those locations into the space of intra-procedural TRUS imaging for targeting. Such an approach to performing biopsy with cognitive MR-TRUS fusion can be implemented with existing conventional 2D TRUS-guided biopsy systems, eliminating the need for the development and integration

of additional hardware and/or software components [92]. However, previous studies [15, 93, 94] have not shown convincing results in terms of improvement in cancer detection rates with this approach in comparison to random systematic biopsy. In addition, a cognitive fusion of images of two modalities is, in principle, operator dependent and needle targeting accuracy is likely to be correlated with the 3D cognitive spatial skills and experience level of the physician with this task. Moreover, rotational symmetry and the limited discrete anatomical landmarks of the prostate available in 2D TRUS images could pose challenges in accurate localization of the target locations in 3D. Thus, the anatomical and spatial context achieved with conventional 2D TRUS guidance alone might not yield the desired level of accuracy to guide needles to successfully sample tissue from target locations.

With the objective of improving needle targeting accuracy during biopsy, systems [6, 8, 95, 96] have been developed to provide 3D guidance during biopsy. In addition to providing a richer 3D context within which to guide biopsy needle insertion, these systems can record and archive biopsy locations in 3D. These archived locations could assist in determining the biopsy target locations if repeat biopsies are required either to avoid targeting previously sampled locations or to take a sample closer to a previously biopsied location. MR-identified target locations have been mapped to the intra-procedural imaging space using two major approaches in the emerging 3D-guided biopsy systems: (1) direct MR-guided biopsy systems, and (2) MR-TRUS fusion biopsy systems.

1.4.1 Direct MR-guided biopsy systems

There are multiple systems [97] developed that are capable of acquiring MR images directly during the procedure for guidance and recording of biopsy locations in 3D. In

these systems, the patient usually lies in the prone position and the needles are inserted via either transrectal or transperineal access. Some of the systems have been designed to perform the MR-guided biopsy in an open bore [98-100], while some others perform the biopsy in a closed bore [95, 101, 102]. Although open bore systems have less confined space during needle manipulation, the image quality is poor due to the use of low field magnets. On the other hand, although closed-bore MR scanners can generate superior image quality for better guidance, the confined space inside the bore could pose challenges in tool design and manipulation. During the typical workflow in these systems, suspicious target delineation is performed using a previously acquired diagnostic MR image prior to the procedure, and identified locations are mapped to the intra-procedural imaging space and verified using serial MR scans acquired immediately prior to needle placement. Ultrasound images are not acquired with these systems, and the ability to perform the biopsy using a single image modality eliminates complications arising when fusing data between two modalities. Although there has been previously published work [103] suggesting improved cancer detection rates with this approach, there are several disadvantages limiting its mainstream use as a standard tool for prostate cancer diagnosis. In-bore biopsy procedures have been reported [95] to require more than an hour and the patient is usually sedated using general anaesthesia. Lengthy MR scanner time and patient recovery times could impose a huge cost burden on the healthcare system, considering the large number of biopsies that needs to be performed in a given year. However, this approach, if proven to have superior targeting accuracy, could be amenable to be used in patients who have to undergo multiple repeat biopsies sessions due to previously inconclusive biopsy results. This approach is also valuable to

MRI-histology correlative research studies, since an MR image can be acquired with the needle in place, allowing for a spatial record of the location of this histologic sample within the coordinate system of the MR image.

1.4.2 MR-TRUS fusion biopsy systems

Mapping of MR targets to TRUS image space via software-based image fusion is the other major approach to 3D-guided biopsy system design. During the clinical workflow in these systems, the diagnostic MR image is typically acquired on a day prior to biopsy to identify suspicious lesions for cancer. These targets are then mapped to a baseline 3D TRUS image acquired immediately prior to performing the biopsy via MR to 3D-TRUS image registration. The co-registration of the MR and 3D TRUS images needs to be performed using a non-rigid transformation to account for the differences in prostate deformation due to pressures exerted from the endorectal coil (if used during MR image acquisition) or alternatively, the lack of pressure from the body coil, and the manually held TRUS probe in the 3D TRUS image acquisition [104, 105]. Live 2D TRUS images are typically acquired during the biopsy procedure for real-time image guidance. The correspondence between live 2D TRUS and the baseline 3D TRUS images, into which the MRI targets have been mapped, is established via tracking of the TRUS probe's position and orientation in space. During the procedure, the physician is able to see a visualization interface that displays the MRI-identified target locations and relative TRUS probe positions and orientations in a 3D context. Thus, in this approach, tumour locations identified from MRI are ultimately targeted with the aid of 3D TRUS image guidance. Hence, the complementary advantages of high soft tissue contrast in MRI and real-time, less expensive TRUS imaging, can be exploited to build an economically

feasible solution with the aim of improving clinical outcomes of prostate cancer diagnosis. In addition, this enables the prostate biopsy to be still performed as an outpatient procedure under local anesthesia, similarly to the conventional 2D TRUS-guided biopsy procedure. Software tools, that accurately co-register MR targets with the baseline 3D TRUS image and intraprocedural TRUS imaging, are thus an essential component to the success of this approach.

Table 1.2: A comparison of some commercially available 3D TRUS-guided biopsy systems.

System	Needle access	US probe type	US probe tracking	Initial 3D US image acquisition
Uronav (In Vivo, USA)	Transrectal	2D TRUS	Magnetic tracking	Free hand axial sweep
Artemis (Eigen, USA)	Transrectal	2D TRUS	Mechanical articulated arm	Rotational sweep
Urostation (Koelis, France)	Transrectal	3D TRUS	Image-based tracking	Panoramic image from 3 volume acquisitions
Biopsee (Pi Medical, Greece)	Transperineal	Bi-plane TRUS	Mechanical stepper	Rotational sweep

There are several solutions developed with different hardware and software designs to provide image guidance for accurate needle targeting using a MR-TRUS fusion approach. Table 1.2 contains a comparison of some commercially available systems showing the approach to image acquisition, tracking and needle placement in the different designs. While some systems are designed to retrofit existing 2D TRUS probes, others utilize TRUS probes with enhanced functionality that can simultaneously acquire bi-plane or full 3D imaging. In systems that use conventional 2D TRUS probes, a 3D TRUS image is acquired at the beginning of the procedure via rotational or translational sweep of the 2D TRUS probe, followed by a reconstruction of the resulting 2D planes to obtain a 3D image. Although enhanced 3D TRUS probes can be more convenient during 3D image acquisition, the ability to retrofit existing ultrasound systems could be a

desirable feature in translating the technology to the widespread clinical use due to the potential to leverage the substantial investment in existing equipment. Accurate and reliable TRUS probe tracking is essential to facilitate 3D guidance in these systems. The Uronav system is equipped with electromagnetic (EM) tracking using an external magnetic field generator and a freehand TRUS probe [10]. The major disadvantage of EM tracking systems is the disruptive influence on tracking arising from potential interference from nearby metal devices in the biopsy environment. The system proposed by Bax et al. [8] uses a mechanically articulated arm to track the motion of the probe during the procedure. While this system provides mechanical stabilisation of the probe, it also supports locking of all joints during 3D initial image acquisition permitting only axial probe rotation. This design is aimed to minimize prostate motion while the 3D image is being acquired, thus minimizing errors during 3D image reconstruction. The system proposed in [6] performs an image-based tracking that completely relies upon the information contained within the image acquired using a specialized probe that can simultaneously reconstruct a 3D volume. Eliminating the hardware tracking devices is a major advantage of this system to come with a compact design. However, this system requires a specialised 3D TRUS imaging system to acquire rich 3D information for tracking purposes.

1.5 Challenges in 3D-guided biopsy systems

In order to achieve accurate cancer detection, the 3D-guided biopsy system needs to accurately sample tissues from the smallest clinically significant tumours. There is a debate in the clinical community regarding the size of the smallest clinically significant

tumour. Epstein et al. [26] suggested a minimum significant prostate tumour volume of 0.5 cm^3 and we refer to this work when discussing the desired level of accuracy in biopsy systems. Assuming we have correctly identified and delineated tumours on MR imaging, there are several potential sources of error that limit 3D-guided biopsy systems in achieving a level of accuracy that allows for needle targeting with high confidence: (1) MR-TRUS co-registration errors, (2) tracking errors in the system, (3) imaging and calibration errors, and (4) errors due to patient and prostate motion/displacement during the procedure. Quantification and minimization of these errors are essential to improving the needle targeting accuracy in 3D biopsy systems. The errors due to sources (1)-(3) have been previously quantified and mitigated [8, 105] in the context of the mechanically-assisted 3D TRUS-guided biopsy system described in [8].

Prostate motion/deformation can cause target misalignment during 3D TRUS-guided biopsy [106]. Since the patient is awake and under local anesthesia, he can move due to discomfort during procedure, which is approximately 15 minutes in duration. The TRUS probe pressure applied while the physician navigates the probe to different regions of the prostate is another potential cause of prostate motion. The needle insertion and biopsy gun firing procedure could also cause some additional motion. These motions during the procedure can disrupt the correspondence between live 2D TRUS images and the targets defined in the coordinate system of the baseline 3D TRUS image, causing target misalignments and needle targeting errors. Studying prostate motion during biopsy and finding methods for motion compensation is critical to improving the needle targeting accuracy of 3D TRUS-guided biopsy systems.

Recent clinical studies [12, 14, 107, 108] comparing 3D versus 2D systematic TRUS-guided biopsies have demonstrated evidence suggesting that prostate cancer detection rates improve with a 3D-guided approach. However, evidence from previous work [109] analysing prostate motion during biopsy suggests that misalignments due to motion can cause substantial errors > 5 mm relative to the clinically significant tumour sizes reported in the literature [26, 110]. Therefore, improving needle targeting accuracy of biopsy systems could help to further improve cancer detection rates of the 3D TRUS guided approach and strengthen the confidence in diagnosing low to intermediate risk cancer. Automatic localization of corresponding anatomical landmarks within the anatomy is one potential approach to track motion during biopsy. Surface-based registration algorithms are an example where the segmentation of the prostate boundary can be used to achieve correspondence. While this approach relies upon an accurate, automatic segmentation algorithm of the prostate, developing such an algorithm that is sufficiently robust can be a challenging task in ultrasound images. Therefore, using the image intensity information could lead to more robust image registration solutions and simplify the workflow by eliminating the need for prostate segmentation. Development and successful clinical translation of rapid image intensity-based registration methods to compensate for misalignments due to prostate motion is an indispensable step towards improving targeting accuracy to enable sampling of clinically significant tumours during prostate biopsy.

1.6 Image-based registration techniques

Image registration is the process of transforming multiple images to spatially align them in a single coordinate system. In image-based registration, the alignment is achieved using the information in image signal intensities. A quantitative measure that reflects the desirable properties of a good alignment is defined as the objective function, and can comprise of an image similarity metric and a regularization term. For rigid registration applications, the objective function is typically the image similarity metric. One image is transformed, interpolated and compared with the other image to calculate the image-similarity metric. In a rigid, affine or non-rigid transformation space, optimization techniques are utilised to find the optimum metric value in an efficient manner. Thus, the registration framework constitutes of multiple components: (1) image similarity metric, (2) optimization technique, (3) transformation (e.g., rigid, affine or non-rigid), and (4) interpolator. These components need to be specified in developing the image-registration technique.

Live 2D TRUS images acquired during the procedure need to be co-registered with the baseline 3D TRUS image acquired at the beginning of the procedure to compensate for motion during the biopsy session. The development of accurate and fast 2D-3D registration methods could be challenging due to the limited information available in the live 2D TRUS image. In solving uni-modality registration problems [10], the sum-of-squared difference (SSD) and normalized cross-correlation (NCC) could be suitable image similarity metrics. While SSD assumes the same level of image intensity at homologous pixels in the two images, NCC tolerates a linear relationship in intensities. Therefore, NCC is invariant to the changes in intensity scaling and shift. These metrics

can be inherently parallelized to achieve high-speed implementations to be useful for clinical application. The capture range of the metric is another important consideration when selecting a useful metric. If the metric has a wide capture range within the transformation space, large misalignments can be compensated using local optimizers to successfully converge at the desired solutions.

Since brute-force searching of the transformation space is intractable due to registration time requirements, the optimization technique is an essential component of the registration algorithm to traverse the transformation space in an efficient manner. While local optimization techniques are widely used in registration problems that have convex, quasi-convex or monotonic objective function landscapes [111], some methods in the literature [112, 113] have investigated the development of global optimization techniques to improve registration accuracy and robustness. Multi-start [114], simulated annealing [115], particle swarm [116], genetic [117] approaches have been used in registration problems with the objective of improving robustness. However, this could lead to an increase in computation times due to the increase in the number of image similarity metric evaluations and slower convergence properties. Efficient implementation of optimization algorithms using graphics processing units (GPU) [113] and development of algorithms with improved convergence properties [118] could be helpful in adopting such algorithms for applications that require rapid registration.

The properties of some optimization techniques can be more desirable in achieving high speed performance in principle. Multiple local optimization techniques (e.g., Newton's method, quasi-Newton method, conjugate gradient method, Powell's method) developed over the years are derived from a quadratic model and have quadratic

convergence properties. These methods assume and approximate second order characteristics of the function within its local neighborhood and are capable of finding the optimum of the function in a finite number of function/derivative evaluations given a reasonable satisfaction of the quadratic model assumption. This is a useful property that aids fast convergence when optimizing a multi-dimensional function in image registration. Techniques that rely on first order properties of the function (e.g., gradient descent/steepest descent [119, 120]), on the other hand, have linear convergence properties. There is another classification of optimization methods based on whether the calculation of the objective function's derivative is required. Some optimization methods (e.g., conjugate gradient method, Newton's method) explicitly calculate the derivative of the objective function, while some others (e.g., Powell's method [121], CMA-ES method [122]) are derivative-free and the optimization is achieved using only function evaluations. Derivative-free methods can be useful if the explicit calculation of the function derivative is either time consuming or not straightforward.

1.7 Image registration accuracy required for the clinical application

The work in this thesis is focused on the errors due to prostate motion that limit the biopsy system in achieving the desired targeting accuracy, but had not been previously quantified and mitigated from the potential sources of error that we have enumerated in section 1.5. Given that the suspicious tumour locations have been identified in the baseline 3D TRUS image, errors due to intermittent patient and prostate motion/displacement during the procedure and due to prostate deformation during the needle insertion and the biopsy-gun firing could challenge the accurate targeting of those

locations using a 3D TRUS-guided biopsy system. On the other hand, there is evidence suggesting that tumours $> 0.5 \text{ cm}^3$ are clinically significant [26, 110]; such tumours have a radius of 5 mm under the spherical assumption. In order to accurately target a 5 mm radius spherical tumour with 95% probability, the root mean square (RMS) error of the biopsy system should be $\leq 2.5 \text{ mm}$.

1.8 Hypothesis

The central hypothesis is that image-based 2D-3D registration of TRUS images can correct for intermittent prostate displacement during the biopsy procedure, with an RMS target registration error (TRE) $\leq 2.5 \text{ mm}$.

1.9 Objectives

To test the central hypothesis, the four major objectives of this thesis work are:

- I. To quantify the prostate motion and deformation due to needle insertion and biopsy-gun firing procedure and calculate the 95% prediction interval around the tissue deformation and compare this deformation in handheld and mechanically-assisted systems.
- II. To (a) develop a 2D-3D registration technique with sufficient accuracy and speed for prostate motion compensation during biopsy, and (b) validate this registration method retrospectively using live 2D TRUS images and baseline 3D TRUS images acquired during human clinical biopsy procedures using a mechanically-assisted 3D TRUS-guided biopsy system [8].
- III. To (a) evaluate the utility of intra-procedural 3D TRUS images in guiding registration during motion compensation to robust solutions, (b) identify the

anatomical regions that benefit the most from such additional intra-procedural 3D information, and (c) test whether a robust rigid registration is sufficient to achieve clinically desired level of accuracy.

- IV. To (a) improve the robustness of registration optimization using learned characteristics from observed prostate motion data, (b) measure the major patterns of prostate motion during biopsy, and (c) modify Powell's direction set method initialization to incorporate learned motion characteristics.

1.10 Thesis outline

1.10.1 Chapter 2 - Quantification of prostate deformation due to needle insertion during TRUS-guided biopsy: Comparison of hand-held and mechanically stabilized systems

In this chapter, we describe our work to quantify the deformation that occurs during the needle insertion and the biopsy-gun firing procedure using non-rigid registration of 2D TRUS images acquired during human clinical biopsy procedures. We calculated the spatially varying 95% confidence interval on the prostate tissue motion and analysed this motion both as a function of distance to the biopsy needle and as a function of distance to the lower piercing point of the prostate. The former is relevant because biopsy targets lie along the needle axis, and the latter is of particular importance due to the reported high concentration of prostate cancer in the peripheral zone, a substantial portion of which lies on the posterior side of the prostate where biopsy needles enter the prostate after penetrating the rectal wall during transrectal biopsy.

The results showed that for both systems, the tissue deformation is such that throughout the length of the needle axis, including regions proximal to the lower piercing point, spherical tumours with radius 2.1 mm or more can be sampled with 95% confidence, under the assumption of zero error elsewhere in the biopsy system. More deformation was observed in the direction orthogonal to the needle axis, compared to the direction parallel to the needle axis; this is of particular importance given the long, narrow shape of the biopsy core. We measured lateral tissue motion proximal to the needle axis of not more than 1.5 mm, with 95% confidence. We observed a statistically significant, but clinically insignificant maximum difference of 0.38 mm in the deformation resulting from the hand held and mechanically assisted systems along the needle axis, and the mechanical system resulted in a lower relative increase in deformation proximal to the needle axis during needle insertion, as well as lower variability of deformation during biopsy gun firing.

1.10.2 Chapter 3 - 2D-3D rigid registration to compensate for prostate motion during 3D TRUS-guided biopsy

The error due to needle insertion and biopsy gun-firing procedure, described in Chapter 2, occurs during a very short period of time and is challenging to compensate. Intermittent patient and prostate motion cause larger misalignments [109] challenging the needle targeting accuracy to meet this requirement. To compensate for this motion, we implemented and tested an intensity-based 2D-3D rigid registration algorithm optimizing the NCC using Powell's method. The 2D TRUS images acquired during the procedure prior to biopsy gun firing were registered to the baseline 3D TRUS image acquired at the

beginning of the procedure. The accuracy was measured by calculating the TRE using manually identified fiducial markers (henceforth *fiducials*) within the prostate for eight patients. These fiducials were used for validation only and were not provided as inputs to the registration algorithm. We also measured the accuracy when the registrations were performed continuously throughout the biopsy procedure by acquiring and registering live 2D TRUS images every second. This measured the improvement in accuracy resulting from performing the registration continuously compensating for motion during the procedure. To further validate the method using a more challenging data set from 10 patients, registrations were performed using 3D TRUS images acquired by intentionally exerting different levels of ultrasound probe pressures in order to measure the performance of our algorithm when the prostate tissue was intentionally deformed. In this data set, biopsy scenarios were simulated by extracting 2D frames from the 3D TRUS images and registering them to the baseline 3D image. A GPU-based implementation was used to improve the registration speed. We also studied the correlation between NCC and TREs.

With the GPU based implementation, the registrations were performed with a mean time of 1.1 s. The TRE values before, during and after registration showed a weak correlation ($r^2 = 0.23$) with the similarity metric. However, we measured a generally convex shape of the metric around the ground truth registration, which may explain the rapid convergence of our algorithm to accurate results. The RMS TRE of registrations performed prior to biopsy gun firing was found to be 1.87 ± 0.81 mm. This was an improvement over 4.75 ± 2.62 mm before registration. When the registrations were performed every second during the biopsy, the RMS TRE was reduced to 1.63 ± 0.51

mm. However, for a 3D data set acquired under a more controlled range of probe pressures intended to test the robustness of the algorithm, the RMS TRE was found to be 3.18 ± 1.6 mm. This was an improvement from 6.89 ± 4.1 mm before registration. Assuming this TRE and the TRE resulting from tissue displacement during needle insertion (Chapter 2) are independent, they can be added in quadrature to determine an overall TRE that can be compared against the 2.5 mm TRE threshold in the central hypothesis. From Chapter 2, we measured an RMS TRE of 1.1 mm; adding (in quadrature) a further TRE of 2.3 mm to this 1.1 mm yields a total of 2.5 mm. *Thus, for the central hypothesis of this work to be confirmed, an image registration algorithm with RMS TRE ≤ 2.3 mm is required.* While the results in this chapter showed encouraging results in improving the accuracy in needle targeting, the measured 3.18 mm RMS TRE suggests that further improvements in accuracy and robustness could be helpful to meet the clinical requirements for successful translation of this method.

1.10.3 Chapter 4 – Evaluating the utility of intra-procedural 3D TRUS image information in guiding registration for displacement compensation during prostate biopsy.

The 2D-3D registration for motion compensation described in Chapter 3 can be challenging in cases where a single plane 2D TRUS plane does not capture enough anatomical context to drive the registration algorithm to the desired solution. While 2D TRUS images are widely used for intra-procedural guidance, some solutions utilize richer intra-procedural images such as bi- or multi-planar TRUS or 3D TRUS, acquired by specialized probes. In this chapter, the impact of such richer intra-procedural imaging on

motion compensation accuracy was measured to evaluate the tradeoff between cost and complexity of intra-procedural imaging versus improved motion compensation. Baseline and intra-procedural 3D TRUS images were acquired from 29 patients at standard sextant-template biopsy locations. Planes extracted from 3D TRUS images acquired at sextant positions were used to simulate 2D and 3D intra-procedural information available in different potential clinically-relevant scenarios for co-registration with the baseline 3D TRUS image. In practice, intra-procedural 3D information can be acquired either via the use of specialized ultrasound probes (e.g., multi-planar or 3D probes) or via axial rotation of a tracked 2D TRUS probe. Registration accuracy was evaluated by calculating the TRE using manually-identified homologous intrinsic fiducial markers (micro-calcifications). The TRE was analysed separately at the base, mid-gland and apex regions of the prostate.

The results indicated that TRE improved gradually as the number of intra-procedural imaging planes used in registration was increased, implying that 3D TRUS information assisted the registration algorithm to robustly converge to more accurate solutions. The acquisition of a partial volume up to the angle of rotation supported more accurate motion compensation than acquiring bi-plane configurations. Additional intra-procedural 3D TRUS image information was more beneficial to registration accuracy in the base and apex regions as compared with the mid-gland region

1.10.4 Chapter 5 – Robust 2D-3D registration optimization to motion compensation using learned prostate motion data

In the previous chapter, we investigated a mechanism to achieve robust registration for motion compensation during biopsy by acquiring additional intra-procedure image information. In this chapter, we discuss an alternative approach to registration to improve accuracy and robustness. We developed and evaluated a registration algorithm in which the optimization is based on learned prostate motion characteristics of the prostate. We performed an unsupervised clustering of rigid prostate motion vectors observed in our data set. We developed a multi-start search strategy, starting at each cluster mean and then directing the search towards the areas where motion vectors had already been observed by appropriately scaling the search space and specifying the initial search directions during optimization using the Powell's direction set method.

Prostate motion analysis and registration validation was performed using a leave-one-out-cross-validation approach using the 3D TRUS images acquired from 29 patients at baseline and sextant template biopsy locations. With this method the RMS TRE \pm std improved from 4.9 ± 2.35 mm to 2.3 ± 1.1 mm. The initial approach described in Chapter 3 yielded an accuracy of 3.1 ± 1.7 mm with this data set. Compared to the initial approach, the updated optimization method improved the robustness during 2D-3D registration by reducing the number of registrations with a TRE > 5 mm from 9.2% to 1.2%. With a total execution time of 2.8 s to perform motion compensation, this method is amenable to useful integration into a clinical 3D guided prostate biopsy workflow.

References

1. K. K. Hodge, J. E. Mcneal, M. K. Terris and T. A. Stamey, "Random Systematic Versus Directed Ultrasound Guided Trans-Rectal Core Biopsies of the Prostate," *Journal of Urology* **142**, 71-75 (1989).
2. K. R. Moreira Leite, L. H. Camara-Lopes, M. F. Dall'Oglio, J. Cury, A. A. Antunes, A. Sanudo and M. Srougi, "Upgrading the Gleason score in extended prostate biopsy: implications for treatment choice," *Int J Radiat Oncol Biol Phys* **73**, 353-356 (2009).
3. D. W. Cool, J. Bax, C. Romagnoli, A. D. Ward, L. Gardi, V. V. Karnik, J. Izawa, J. Chin and A. Fenster, *Medical Image Computing and Computer-Assisted Intervention (MICCAI): Prostate Cancer Imaging Workshop*, Toronto, Canada, 2011.
4. B. A. Hadaschik, T. H. Kuru, C. Tulea, P. Rieker, I. V. Popeneciu, T. Simpfendorfer, J. Huber, P. Zogal, D. Teber, S. Pahernik, M. Roethke, P. Zamecnik, W. Roth, G. Sakas, H. P. Schlemmer and M. Hohenfellner, "A novel stereotactic prostate biopsy system integrating pre-interventional magnetic resonance imaging and live ultrasound fusion," *J Urol* **186**, 2214-2220 (2011).
5. P. A. Pinto, P. H. Chung, A. R. Rastinehad, A. A. Baccala, Jr., J. Kruecker, C. J. Benjamin, S. Xu, P. Yan, S. Kadoury, C. Chua, J. K. Locklin, B. Turkbey, J. H. Shih, S. P. Gates, C. Buckner, G. Bratslavsky, W. M. Linehan, N. D. Glossop, P. L. Choyke and B. J. Wood, "Magnetic resonance imaging/ultrasound fusion guided prostate biopsy improves cancer detection following transrectal ultrasound biopsy and correlates with multiparametric magnetic resonance imaging," *J Urol* **186**, 1281-1285 (2011).
6. M. Baumann, P. Mozer, V. Daanen and J. Troccaz, "Prostate biopsy tracking with deformation estimation," *Med Image Anal* **16**, 562-576 (2013).
7. M. Baumann, P. Mozer, V. Daanen and J. Troccaz, "Prostate biopsy assistance system with gland deformation estimation for enhanced precision," *Med Image Comput Assist Interv* **12**, 67-74 (2009).
8. J. Bax, D. Cool, L. Gardi, K. Knight, D. Smith, J. Montreuil, S. Sherebrin, C. Romagnoli and A. Fenster, "Mechanically assisted 3D ultrasound guided prostate biopsy system," *Med Phys* **35**, 5397-5410 (2008).
9. D. Cool, S. Sherebrin, J. Izawa, J. Chin and A. Fenster, "Design and evaluation of a 3D transrectal ultrasound prostate biopsy system," *Med Phys* **35**, 4695-4707 (2008).
10. S. Xu, J. Kruecker, B. Turkbey, N. Glossop, A. K. Singh, P. Choyke, P. Pinto and B. J. Wood, "Real-time MRI-TRUS fusion for guidance of targeted prostate biopsies," *Comput Aided Surg* **13**, 255-264 (2008).

11. O. Ukimura, M. M. Desai, S. Palmer, S. Valencerina, M. Gross, A. L. Abreu, M. Aron and I. S. Gill, "3-Dimensional elastic registration system of prostate biopsy location by real-time 3-dimensional transrectal ultrasound guidance with magnetic resonance/transrectal ultrasound image fusion," *J Urol* **187**, 1080-1086 (2012).
12. G. A. Sonn, S. Natarajan, D. J. A. Margolis, M. MacAiran, P. Lieu, J. T. Huang, F. J. Dorey and L. S. Marks, "Targeted Biopsy in the Detection of Prostate Cancer Using an Office Based Magnetic Resonance Ultrasound Fusion Device," *Journal of Urology* **189**, 86-91 (2013).
13. M. M. Siddiqui, S. Rais-Bahrami, H. Truong, L. Stamatakis, S. Vourganti, J. Nix, A. N. Hoang, A. Walton-Diaz, B. Shuch, M. Weintraub, J. Kruecker, H. Amalou, B. Turkbey, M. J. Merino, P. L. Choyke, B. J. Wood and P. A. Pinto, "Magnetic Resonance Imaging/Ultrasound-Fusion Biopsy Significantly Upgrades Prostate Cancer Versus Systematic 12-core Transrectal Ultrasound Biopsy," *European Urology* **64**, 713-719 (2013).
14. P. A. Pinto, P. H. Chung, A. R. Rastinehad, A. A. Baccala, J. Kruecker, C. J. Benjamin, S. Xu, P. K. Yan, S. Kadoury, C. Chua, J. K. Locklin, B. Turkbey, J. H. Shih, S. P. Gates, C. Buckner, G. Bratslavsky, W. M. Linehan, N. D. Glossop, P. L. Choyke and B. J. Wood, "Magnetic Resonance Imaging/Ultrasound Fusion Guided Prostate Biopsy Improves Cancer Detection Following Transrectal Ultrasound Biopsy and Correlates With Multiparametric Magnetic Resonance Imaging," *Journal of Urology* **186**, 1281-1285 (2011).
15. N. B. Delongchamps, M. Peyromaure, A. Schull, F. Beuvon, N. Bouazza, T. Flam, M. Zerbib, N. Muradyan, P. Legman and F. Cornud, "Prebiopsy Magnetic Resonance Imaging and Prostate Cancer Detection: Comparison of Random and Targeted Biopsies," *Journal of Urology* **189**, 493-499 (2013).
16. T. De Silva, A. Fenster, D. Cool, L. Gardi, C. Romagnoli, J. Samarabandu and A. D. Ward, "2D-3D rigid registration to compensate for prostate motion during 3D-TRUS guided biopsy," *Medical Physics* **40**, 022904 (2013).
17. "Canadian Cancer Society's Advisory Committee on Cancer Statistics , Canadian Cancer Statistics 2013," (2013).
18. D. Bonekamp, M. A. Jacobs, R. El-Khouli, D. Stoianovici and K. J. Macura, "Advancements in MR imaging of the prostate: from diagnosis to interventions," *Radiographics : a review publication of the Radiological Society of North America, Inc* **31**, 677-703 (2011).
19. J. E. Mcneal, "Regional Morphology and Pathology of Prostate," *Am J Clin Pathol* **49**, 347-& (1968).

20. J. E. Mcneal, "Origin and Evolution of Benign Prostatic Enlargement," *Invest Urol* **15**, 340-345 (1978).
21. J. E. Mcneal, "The Zonal Anatomy of the Prostate," *Prostate* **2**, 35-49 (1981).
22. J. I. Epstein and G. J. Netto, *Biopsy Interpretation of the Prostate*, 4th Edition ed. (2008).
23. Y. L. Chang, S. D. Chang, A. S. Chao, P. C. C. Hsieh, C. N. Wang and T. H. Wang, "Placenta Share Discordance and Umbilical Artery Doppler Change After Antenatal Betamethasone Administration in Monochorionic Twins With Selective Intrauterine Growth Restriction: Is There a Link?," *Twin Res Hum Genet* **15**, 680-684 (2012).
24. D. G. Bostwick, H. B. Burke, D. Djakiew, S. Euling, S. M. Ho, J. Landolph, H. Morrison, B. Sonawane, T. Shifflett, D. J. Waters and B. Timms, "Human prostate cancer risk factors," *Cancer* **101**, 2371-2490 (2004).
25. I. M. Thompson, D. P. Ankerst, C. Chi, P. J. Goodman, C. M. Tangen, M. S. Lucia, Z. D. Feng, H. L. Parnes and C. A. Coltman, "Assessing prostate cancer risk: Results from the prostate cancer prevention trial," *J Natl Cancer I* **98**, 529-534 (2006).
26. J. I. Epstein, P. C. Walsh, M. Carmichael and C. B. Brendler, "Pathologic and clinical findings to predict tumor extent of nonpalpable (stage T1c) prostate cancer," *JAMA : the journal of the American Medical Association* **271**, 368-374 (1994).
27. D. S. Smith and W. J. Catalona, "Interexaminer variability of digital rectal examination in detecting prostate cancer," *Urology* **45**, 70-74 (1995).
28. W. J. Catalona, A. W. Partin, K. M. Slawin, M. K. Brawer, R. C. Flanigan, A. Patel, J. P. Richie, J. B. deKernion, P. C. Walsh, P. T. Scardino, P. H. Lange, E. N. P. Subong, R. E. Parson, G. H. Gasior, K. G. Loveland and P. C. Southwick, "Use of the percentage of free prostate-specific antigen to enhance differentiation of prostate cancer from benign prostatic disease - A prospective multicenter clinical trial," *Jama- J Am Med Assoc* **279**, 1542-1547 (1998).
29. M. A. Khan, A. W. Partin, H. G. Rittenhouse, S. D. Mikolajczyk, L. J. Sokoll, D. W. Chan and R. W. Veltri, "Evaluation of proprostate specific antigen for early detection of prostate cancer in men with a total prostate specific antigen range of 4.0 to 10.0 ng/ml," *J Urol* **170**, 723-726 (2003).
30. A. V. Sarma and D. Schottenfeld, "Projecting prostate cancer incidence & mortality trends using the Surveillance, Epidemiology and End Results (SEER) data.," *Am J Epidemiol* **155**, s15-s15 (2002).
31. A. M. D. Wolf, R. C. Wender, R. B. Etzioni, I. M. Thompson, A. V. D'Amico, R. J. Volk, D. D. Brooks, C. Dash, I. Guessous, K. Andrews, C. DeSantis and R. A. Smith,

- "American Cancer Society Guideline for the Early Detection of Prostate Cancer Update 2010," *Ca-Cancer J Clin* **60**, 70-98 (2010).
32. J. C. Presti, J. J. Chang, V. Bhargava and K. Shinohara, "The optimal systematic prostate biopsy scheme should include 8 rather than 6 biopsies: Results of a prospective clinical trial," *Journal of Urology* **163**, 163-166 (2000).
 33. L. A. Eskew, R. L. Bare and D. L. McCullough, "Systematic 5 region prostate biopsy is superior to sextant method for diagnosing carcinoma of the prostate," *Journal of Urology* **157**, 199-202 (1997).
 34. S. B. Edge and C. C. Compton, "The American Joint Committee on Cancer: the 7th Edition of the AJCC Cancer Staging Manual and the Future of TNM," *Ann Surg Oncol* **17**, 1471-1474 (2010).
 35. K. Shinohara, T. M. Wheeler and P. T. Scardino, "The appearance of prostate cancer on transrectal ultrasonography: correlation of imaging and pathological examinations," *J Urol* **142**, 76-82 (1989).
 36. A. M. Hovels, R. A. Heesakkers, E. M. Adang, G. J. Jager, S. Strum, Y. L. Hoogeveen, J. L. Severens and J. O. Barentsz, "The diagnostic accuracy of CT and MRI in the staging of pelvic lymph nodes in patients with prostate cancer: a meta-analysis," *Clinical radiology* **63**, 387-395 (2008).
 37. M. R. Engelbrecht, G. J. Jager, R. J. Laheij, A. L. Verbeek, H. J. van Lier and J. O. Barentsz, "Local staging of prostate cancer using magnetic resonance imaging: a meta-analysis," *European radiology* **12**, 2294-2302 (2002).
 38. D. F. Gleason and G. T. Mellinger, "Prediction of prognosis for prostatic adenocarcinoma by combined histological grading and clinical staging," *J Urol* **111**, 58-64 (1974).
 39. M. J. Zelefsky, S. A. Leibel, P. B. Gaudin, G. J. Kutcher, N. E. Fleshner, E. S. Venkatramen, V. E. Reuter, W. R. Fair, C. C. Ling and Z. Fuks, "Dose escalation with three-dimensional conformal radiation therapy affects the outcome in prostate cancer," *Int J Radiat Oncol* **41**, 491-500 (1998).
 40. L. N. Lee, R. G. Stock and N. N. Stone, "Role of hormonal therapy in the management of intermediate- to high-risk prostate cancer treated with permanent radioactive seed implantation," *Int J Radiat Oncol* **52**, 444-452 (2002).
 41. A. V. D'Amico, R. Whittington, S. B. Malkowicz, D. Schultz, K. Blank, G. A. Broderick, J. E. Tomaszewski, A. A. Renshaw, I. Kaplan, C. J. Beard and A. Wein, "Biochemical outcome after radical prostatectomy, external beam radiation therapy, or interstitial radiation therapy for clinically localized prostate cancer," *JAMA : the journal of the American Medical Association* **280**, 969-974 (1998).

42. K. G. Fink, G. Hutarew, B. Esterbauer, A. Pytel, A. Jungwirth, O. Dietze and N. T. Schmeller, "Evaluation of transition zone and lateral sextant biopsies for prostate cancer detection after initial sextant biopsy," *Urology* **61**, 748-753 (2003).
43. N. Stroumbakis, M. S. Cookson, V. E. Reuter and W. R. Fair, "Clinical significance of repeat sextant biopsies in prostate cancer patients," *Urology* **49**, 113-118 (1997).
44. J. L. Gore, S. F. Shariat, B. J. Miles, D. Kadmon, N. Jiang, T. M. Wheeler and K. M. Slawin, "Optimal combinations of systematic sextant and laterally directed biopsies for the detection of prostate cancer," *J Urol* **165**, 1554-1559 (2001).
45. D. W. Keetch, W. J. Catalona and D. S. Smith, "Serial Prostatic Biopsies in Men with Persistently Elevated Serum Prostate-Specific Antigen Values," *Journal of Urology* **151**, 1571-1574 (1994).
46. C. S. Stewart, B. C. Leibovich, A. L. Weaver and M. M. Lieber, "Prostate cancer diagnosis using a saturation needle biopsy technique after previous negative sextant biopsies," *Journal of Urology* **166**, 86-91 (2001).
47. N. Fleshner and L. Klotz, "Role of "saturation biopsy" in the detection of prostate cancer among difficult diagnostic cases," *Urology* **60**, 93-97 (2002).
48. P. G. Borboroglu, S. W. Comer, R. H. Riffenburgh and C. L. Amling, "Extensive repeat transrectal ultrasound guided prostate biopsy in patients with previous benign sextant biopsies," *Journal of Urology* **163**, 158-162 (2000).
49. R. A. Ashley, B. A. Inman, J. C. Routh, L. A. Mynderse, M. T. Gettman and M. L. Blute, "Reassessing the diagnostic yield of saturation biopsy of the prostate," *European Urology* **53**, 976-983 (2008).
50. M. D. Rifkin, "Ultrasound of the Prostate - Applications and Indications," *Schweiz Med Wschr* **121**, 282-291 (1991).
51. M. E. Chen, D. A. Johnston, K. Tang, R. J. Babaian and P. Troncoso, "Detailed mapping of prostate carcinoma foci: biopsy strategy implications," *Cancer* **89**, 1800-1809 (2000).
52. S. Jones, *Prostate cancer diagnosis: PSA, biopsy and beyond*. (Springer, 2012).
53. C. B. Ching, A. S. Moussa, J. B. Li, B. R. Lane, C. Zippe and J. S. Jones, "Does Transrectal Ultrasound Probe Configuration Really Matter? End Fire Versus Side Fire Probe Prostate Cancer Detection Rates," *Journal of Urology* **181**, 2077-2082 (2009).
54. E. A. Singer, D. J. Golijanin, R. S. Davis and V. Dogra, "What's new in urologic ultrasound?," *The Urologic clinics of North America* **33**, 279-286 (2006).

55. P. J. Littrup and S. E. Bailey, "Prostate cancer: the role of transrectal ultrasound and its impact on cancer detection and management," *Radiologic clinics of North America* **38**, 87-113 (2000).
56. R. Kranse, P. Beemsterboer, J. Rietbergen, D. Habbema, J. Hugosson and F. H. Schroder, "Predictors for biopsy outcome in the European Randomized Study of Screening for Prostate Cancer (Rotterdam region)," *Prostate* **39**, 316-322 (1999).
57. F. Lee, S. T. Torp-Pedersen, D. B. Siders, P. J. Littrup and R. D. McLeary, "Transrectal ultrasound in the diagnosis and staging of prostatic carcinoma," *Radiology* **170**, 609-615 (1989).
58. P. Hammerer and H. Huland, "Systematic sextant biopsies in 651 patients referred for prostate evaluation," *J Urol* **151**, 99-102 (1994).
59. M. Norberg, L. Egevad, L. Holmberg, P. Sparen, B. J. Norlen and C. Busch, "The sextant protocol for ultrasound-guided core biopsies of the prostate underestimates the presence of cancer," *Urology* **50**, 562-566 (1997).
60. J. L. Sauvain, P. Palascak, D. Bourscheid, C. Chabi, A. Atassi, J. M. Bregon and R. Palascak, "Value of power doppler and 3D vascular sonography as a method for diagnosis and staging of prostate cancer," *Eur Urol* **44**, 21-30; discussion 30-21 (2003).
61. W. J. Ellis, M. P. Chetner, S. D. Preston and M. K. Brawer, "Diagnosis of prostatic carcinoma: the yield of serum prostate specific antigen, digital rectal examination and transrectal ultrasonography," *J Urol* **152**, 1520-1525 (1994).
62. M. D. Rifkin, G. S. Sudakoff and A. A. Alexander, "Prostate: techniques, results, and potential applications of color Doppler US scanning," *Radiology* **186**, 509-513 (1993).
63. M. Remzi, M. Dobrovits, A. Reissigl, V. Ravery, M. Waldert, C. Wiunig, Y. K. Fong, B. Djavan and U. European Society for Oncological, "Can Power Doppler enhanced transrectal ultrasound guided biopsy improve prostate cancer detection on first and repeat prostate biopsy?," *Eur Urol* **46**, 451-456 (2004).
64. C. E. Neumaier, C. Martinoli, L. E. Derchi, E. Silvestri and I. Rosenberg, "Normal prostate gland: examination with color Doppler US," *Radiology* **196**, 453-457 (1995).
65. P. N. Burns and S. R. Wilson, "Microbubble contrast for radiological imaging: 1. Principles," *Ultrasound quarterly* **22**, 5-13 (2006).

66. R. A. Linden, E. J. Trabulsi, F. Forsberg, P. R. Gittens, L. G. Gomella and E. J. Halpern, "Contrast enhanced ultrasound flash replenishment method for directed prostate biopsies," *J Urol* **178**, 2354-2358 (2007).
67. J. Ophir, I. Cespedes, H. Ponnekanti, Y. Yazdi and X. Li, "Elastography: a quantitative method for imaging the elasticity of biological tissues," *Ultrasonic imaging* **13**, 111-134 (1991).
68. E. D. Nelson, C. B. Slotoroff, L. G. Gomella and E. J. Halpern, "Targeted biopsy of the prostate: the impact of color Doppler imaging and elastography on prostate cancer detection and Gleason score," *Urology* **70**, 1136-1140 (2007).
69. M. J. Mitterberger, F. Aigner, W. Horninger, H. Ulmer, S. Cavuto, E. J. Halpern and F. Frauscher, "Comparative efficiency of contrast-enhanced colour Doppler ultrasound targeted versus systematic biopsy for prostate cancer detection," *European radiology* **20**, 2791-2796 (2010).
70. C. Brossner, H. Ringhofer, T. Hernady, W. Kuber, S. Madersbacher and A. Pycha, "Lymphatic drainage of prostatic transition and peripheral zones visualized on a three-dimensional workstation," *Urology* **57**, 389-393 (2001).
71. C. M. Tempany, X. Zhou, E. A. Zerhouni, M. D. Rifkin, L. E. Quint, C. W. Piccoli, J. H. Ellis and B. J. McNeil, "Staging of prostate cancer: results of Radiology Diagnostic Oncology Group project comparison of three MR imaging techniques," *Radiology* **192**, 47-54 (1994).
72. B. N. Bloch, N. M. Rofsky, R. H. Baroni, R. P. Marquis, I. Pedrosa and R. E. Lenkinski, "3 Tesla magnetic resonance imaging of the prostate with combined pelvic phased-array and endorectal coils; Initial experience(1)," *Academic radiology* **11**, 863-867 (2004).
73. C. L. Carrol, F. G. Sommer, J. E. McNeal and T. A. Stamey, "The abnormal prostate: MR imaging at 1.5 T with histopathologic correlation," *Radiology* **163**, 521-525 (1987).
74. J. J. Hom, F. V. Coakley, J. P. Simko, A. Qayyum, P. Carroll and J. Kurhanewicz, "Endorectal MR and MR spectroscopic imaging of prostate cancer: Histopathological determinants of tumor visibility," *Am J Roentgenol* **184**, 62-62 (2005).
75. V. Kumar, N. R. Jagannathan, R. Kumar, S. Thulkar, S. D. Gupta, S. N. Dwivedi, A. K. Hemal and N. P. Gupta, "Apparent diffusion coefficient of the prostate in men prior to biopsy: determination of a cut-off value to predict malignancy of the peripheral zone," *Nmr Biomed* **20**, 505-511 (2007).
76. T. Tamada, T. Sone, S. Toshimitsu, S. Imai, Y. Jo, K. Yoshida, A. Yamamoto, T. Yamashita, N. Egashira, K. Nagai and M. Fukunaga, "Age-related and zonal

- anatomical changes of apparent diffusion coefficient values in normal human prostatic tissues," *J Magn Reson Imaging* **27**, 552-556 (2008).
77. J. Ren, Y. Huan, H. Wang, H. T. Zhao, Y. L. Ge, Y. J. Chang and Y. Liu, "Diffusion-weighted imaging in normal prostate and differential diagnosis of prostate diseases," *Abdom Imaging* **33**, 724-728 (2008).
78. K. N. A. Nagel, M. G. Schouten, T. Hambroek, G. J. S. Litjens, C. M. A. Hoeks, B. ten Haken, J. O. Barentsz and J. J. Futterer, "Differentiation of Prostatitis and Prostate Cancer by Using Diffusion-weighted MR Imaging and MR-guided Biopsy at 3 T," *Radiology* **267**, 164-172 (2013).
79. H. J. Huisman, M. R. Engelbrecht and J. O. Barentsz, "Accurate estimation of pharmacokinetic contrast-enhanced dynamic MRI parameters of the prostate," *J Magn Reson Imaging* **13**, 607-614 (2001).
80. R. Alonzi, A. R. Padhani and C. Allen, "Dynamic contrast enhanced MRI in prostate cancer," *Eur J Radiol* **63**, 335-350 (2007).
81. C. M. Hoeks, J. O. Barentsz, T. Hambroek, D. Yakar, D. M. Somford, S. W. Heijmink, T. W. Scheenen, P. C. Vos, H. Huisman, I. M. van Oort, J. A. Witjes, A. Heerschap and J. J. Futterer, "Prostate cancer: multiparametric MR imaging for detection, localization, and staging," *Radiology* **261**, 46-66 (2011).
82. R. S. Sahebjavaher, A. Baghani, M. Honarvar, R. Sinkus and S. E. Salcudean, "Transperineal prostate MR elastography: initial in vivo results," *Magn Reson Med* **69**, 411-420 (2013).
83. J. Near and R. Bartha, "Quantitative Sodium MRI of the Mouse Prostate," *Magn Reson Med* **63**, 822-827 (2010).
84. J. O. Barentsz, J. Richenberg, R. Clements, P. Choyke, S. Verma, G. Villeirs, O. Rouviere, V. Logager and J. J. Futterer, "ESUR prostate MR guidelines 2012," *European radiology* **22**, 746-757 (2012).
85. A. D. Ward, C. Crukley, C. A. McKenzie, J. Montreuil, E. Gibson, C. Romagnoli, J. A. Gomez, M. Moussa, J. Chin, G. Bauman and A. Fenster, "Prostate: Registration of Digital Histopathologic Images to in Vivo MR Images Acquired by Using Endorectal Receive Coil," *Radiology* **263**, 856-864 (2012).
86. E. Gibson, M. Gaed, J. A. Gomez, M. Moussa, C. Romagnoli, S. Pautler, J. L. Chin, C. Crukley, G. S. Bauman, A. Fenster and A. D. Ward, "3D prostate histology reconstruction: An evaluation of image-based and fiducial-based algorithms," *Medical Physics* **40** (2013).

87. Y. Q. Zhan, Y. M. Ou, M. Feldman, J. Tomaszewski, C. Davatzikos and D. G. Shen, "Registering histologic and MR images of prostate for image-based cancer detection," *Academic radiology* **14**, 1367-1381 (2007).
88. V. Shah, T. Pohida, B. Turkbey, H. Mani, M. Merino, P. A. Pinto, P. Choyke and M. Bernardo, "A method for correlating in vivo prostate magnetic resonance imaging and histopathology using individualized magnetic resonance -based molds," *Rev Sci Instrum* **80** (2009).
89. C. K. Kim, B. K. Park and B. Kim, "Localization of prostate cancer using 3T MRI: comparison of T2-weighted and dynamic contrast-enhanced imaging," *Journal of computer assisted tomography* **30**, 7-11 (2006).
90. P. Gibbs, M. D. Pickles and L. W. Turnbull, "Diffusion imaging of the prostate at 3.0 tesla," *Investigative radiology* **41**, 185-188 (2006).
91. A. Villers, P. Puech, D. Mouton, X. Leroy, C. Ballereau and L. Lemaitre, "Dynamic contrast enhanced, pelvic phased array magnetic resonance imaging of localized prostate cancer for predicting tumor volume: correlation with radical prostatectomy findings," *J Urol* **176**, 2432-2437 (2006).
92. J. K. Logan, S. Rais-Bahrami, B. Turkbey, A. Gomella, H. Amalou, P. L. Choyke, B. J. Wood and P. A. Pinto, "Current Status of MRI and Ultrasound Fusion Software Platforms for Guidance of Prostate Biopsies," *BJU Int* (2013).
93. J. Haffner, L. Lemaitre, P. Puech, G. P. Haber, X. Leroy, J. S. Jones and A. Villers, "Role of magnetic resonance imaging before initial biopsy: comparison of magnetic resonance imaging-targeted and systematic biopsy for significant prostate cancer detection," *BJU Int* **108**, E171-178 (2011).
94. P. Puech, O. Rouviere, R. Renard-Penna, A. Villers, P. Devos, M. Colombel, M. O. Bitker, X. Leroy, F. Mege-Lechevallier, E. Comperat, A. Ouzzane and L. Lemaitre, "Prostate cancer diagnosis: multiparametric MR-targeted biopsy with cognitive and transrectal US-MR fusion guidance versus systematic biopsy--prospective multicenter study," *Radiology* **268**, 461-469 (2013).
95. A. Krieger, R. C. Susil, C. Menard, J. A. Coleman, G. Fichtinger, E. Atalar and L. L. Whitcomb, "Design of a novel MRI compatible manipulator for image guided prostate interventions," *IEEE Trans Biomed Eng* **52**, 306-313 (2005).
96. A. Krieger, Iordachita, II, P. Guion, A. K. Singh, A. Kaushal, C. Menard, P. A. Pinto, K. Camphausen, G. Fichtinger and L. L. Whitcomb, "An MRI-compatible robotic system with hybrid tracking for MRI-guided prostate intervention," *IEEE Trans Biomed Eng* **58**, 3049-3060 (2011).

97. K. M. Pondman, J. J. Futterer, B. ten Haken, L. J. Schultze Kool, J. A. Witjes, T. Hambroek, K. J. Macura and J. O. Barentsz, "MR-guided biopsy of the prostate: an overview of techniques and a systematic review," *Eur Urol* **54**, 517-527 (2008).
98. S. P. DiMaio, S. Pieper, K. Chinzei, N. Hata, S. J. Haker, D. F. Kacher, G. Fichtinger, C. M. Tempany and R. Kikinis, "Robot-assisted needle placement in open MRI: system architecture, integration and validation," *Comput Aided Surg* **12**, 15-24 (2007).
99. N. Hata, M. Jinzaki, D. Kacher, R. Cormak, D. Gering, A. Nabavi, S. G. Silverman, A. V. D'Amico, R. Kikinis, F. A. Jolesz and C. M. Tempany, "MR imaging-guided prostate biopsy with surgical navigation software: device validation and feasibility," *Radiology* **220**, 263-268 (2001).
100. A. V. D'Amico, C. M. Tempany, R. Cormack, N. Hata, M. Jinzaki, K. Tuncali, M. Weinstein and J. P. Richie, "Transperineal magnetic resonance image guided prostate biopsy," *J Urol* **164**, 385-387 (2000).
101. K. Engelhard, H. P. Hollenbach, B. Kiefer, A. Winkel, K. Goeb and D. Engehausen, "Prostate biopsy in the supine position in a standard 1.5-T scanner under real time MR-imaging control using a MR-compatible endorectal biopsy device," *European radiology* **16**, 1237-1243 (2006).
102. R. C. Susil, C. Menard, A. Krieger, J. A. Coleman, K. Camphausen, P. Choyke, G. Fichtinger, L. L. Whitcomb, C. N. Coleman and E. Atalar, "Transrectal prostate biopsy and fiducial marker placement in a standard 1.5T magnetic resonance imaging scanner," *J Urol* **175**, 113-120 (2006).
103. T. Hambroek, C. Hoeks, C. Hulsbergen-van de Kaa, T. Scheenen, J. Futterer, S. Bouwense, I. van Oort, F. Schroder, H. Huisman and J. Barentsz, "Prospective assessment of prostate cancer aggressiveness using 3-T diffusion-weighted magnetic resonance imaging-guided biopsies versus a systematic 10-core transrectal ultrasound prostate biopsy cohort," *Eur Urol* **61**, 177-184 (2012).
104. Y. P. Hu, H. U. Ahmed, Z. Taylor, C. Allen, M. Emberton, D. Hawkes and D. Barratt, "MR to ultrasound registration for image-guided prostate interventions," *Medical Image Analysis* **16**, 687-703 (2012).
105. Y. Sun, J. Yuan, M. Rajchl, W. Qiu, C. Romagnoli and A. Fenster, "Efficient Convex Optimization Approach to 3D Non-rigid MR-TRUS Registration," *Medical Image Computing and Computer-Assisted Intervention (Miccai 2013), Pt I* **8149**, 195-202 (2013).
106. V. V. Karnik, A. Fenster, J. Bax, C. Romagnoli and A. D. Ward, "Evaluation of intersession 3D-TRUS to 3D-TRUS image registration for repeat prostate biopsies," *Med Phys* **38**, 1832-1843 (2011).

107. D. G. Engehausen, K. Engelhard, S. A. Schwab, M. Uder, S. Wach, B. Wullich and F. S. Krause, "Magnetic Resonance Image-Guided Biopsies with a High Detection Rate of Prostate Cancer," *Sci World J* (2012).
108. A. Peltier, F. Aoun, F. El-Khoury, E. Hawaux, K. Limani, K. Narahari, N. Sirtaine and R. van Velthoven, "3D versus 2D Systematic Transrectal Ultrasound-Guided Prostate Biopsy: Higher Cancer Detection Rate in Clinical Practice," *Prostate Cancer* **2013**, 783243 (2013).
109. V. V. Karnik, A. Fenster, J. Bax, D. W. Cool, L. Gardi, I. Gyacskov, C. Romagnoli and A. D. Ward, "Assessment of image registration accuracy in three-dimensional transrectal ultrasound guided prostate biopsy," *Med Phys* **37**, 802-813 (2010).
110. G. Ploussard, J. I. Epstein, R. Montironi, P. R. Carroll, M. Wirth, M. O. Grimm, A. S. Bjartell, F. Montorsi, S. J. Freedland, A. Erbersdobler and T. H. van der Kwast, "The Contemporary Concept of Significant Versus Insignificant Prostate Cancer," *European Urology* **60**, 291-303 (2011).
111. P. Markelj, D. Tomazvic, B. Likar and F. Pernus, "A review of 3D/2D registration methods for image-guided interventions," *Medical Image Analysis* **16**, 642-661 (2012).
112. M. Jenkinson, P. Bannister, M. Brady and S. Smith, "Improved optimization for the robust and accurate linear registration and motion correction of brain images," *Neuroimage* **17**, 825-841 (2002).
113. Y. Otake, A. S. Wang, J. W. Stayman, A. Uneri, G. Kleinszig, S. Vogt, A. J. Khanna, Z. L. Gokaslan and J. H. Siewerdsen, "Robust 3D-2D image registration: application to spine interventions and vertebral labeling in the presence of anatomical deformation," *Physics in Medicine and Biology* **58**, 8535-8553 (2013).
114. G. A. Turgeon, G. Lehmann, G. Guiraudon, M. Drangova, D. Holdsworth and T. Peters, "2D-3D registration of coronary angiograms for cardiac procedure planning and guidance," *Medical Physics* **32**, 3737-3749 (2005).
115. M. Vermandel, N. Betrouni, J. Y. Gauvrit, D. Pasquier, C. Vasseur and J. Rousseau, "Intrinsic 2D/3D registration based on a hybrid approach: Use in the radiosurgical imaging process.," *Cell Mol Biol* **52**, 44-53 (2006).
116. M. P. Wachowiak, R. Smolikova, Y. F. Zheng, J. M. Zurada and A. S. Elmaghraby, "An approach to multimodal biomedical image registration utilizing particle swarm optimization," *Ieee T Evolut Comput* **8**, 289-301 (2004).
117. D. Knaan and L. Joskowicz, "Effective intensity-based 2D/3D rigid registration between fluoroscopic X-ray and CT," *Lect Notes Comput Sc* **2878**, 351-358 (2003).

118. C. Igel, T. Suttorp and N. Hansen, "A computational efficient covariance matrix update and a (1+1)-CMA for evolution strategies," *Gecco 2006: Genetic and Evolutionary Computation Conference, Vol 1 and 2*, 453-460 (2006).
119. D. Zikic, M. Groher, A. Khamene and N. Navab, "Deformable registration of 3D vessel structures to a single projection image," *Medical Imaging 2008: Image Processing, Pts 1-3* **6914** (2008).
120. H. Lamecker, T. H. Wenckebach and H. C. Hege, "Atlas-based 3D-shape reconstruction from x-ray images," *Int C Patt Recog*, 371-374 (2006).
121. M. J. D. Powell, "A Method for Minimizing a Sum of Squares of Non-Linear Functions without Calculating Derivatives," *Comput J* **7**, 303-307 (1965).
122. N. Hansen and A. Ostermeier, "Completely derandomized self-adaptation in evolution strategies," *Evol Comput* **9**, 159-195 (2001).

Chapter 2.

Quantification of prostate deformation due to needle insertion during TRUS-guided biopsy: Comparison of hand-held and mechanically stabilized systems

2.1 Introduction

Prostate biopsy is currently the clinical standard for definitive diagnosis, and two-dimensional (2D) transrectal ultrasound (TRUS) is the most common imaging modality used for guidance during biopsy. However, TRUS-guided biopsy suffers from significant limitations related to difficulties in targeting predefined locations within the prostate, resulting in a false negative rate as high as 29.1% [1]. The limited anatomic information provided by 2D TRUS makes navigation to predefined 3D locations challenging [2], and does not permit a 3D record of biopsy locations, which can be useful in a repeat session wherein previously-determined suspicious targets may need to be rebiopsied. In order to overcome these drawbacks, magnetic resonance imaging (MRI) and TRUS guided systems have been developed to provide biopsy location information in 3D [3-5]. In these systems, biopsy target locations can be determined from previous biopsy sessions, or the radiologist's assessment of an image from a different modality.

In order to be translated to clinical use, a biopsy system should meet the criterion of sampling tumours greater than or equal to a clinically significant minimum size with 95% confidence. A minimum significant prostate cancer volume of 0.5 cm^3 (5 mm radius under an assumption of spherical tumour shape) has been previously established [6]. To meet the targeting criterion, the root-mean-square (RMS) error of a biopsy

system's delivery of needles to targets must be less than 2.5 mm [7]. There are several potential sources of error in biopsy systems: (1) mechanical guidance system errors, (2) imaging and calibration errors, (3) patient and prostate motion due to discomfort during the procedure, (4) prostate deformation due to biopsy needle insertion prior to firing the biopsy gun, and (5) prostate deformation due to biopsy gun firing. The effects of the first three sources of error have been quantified previously [3, 5, 7]. The cumulative effect of all of the above sources has been quantified in the context of MRI-guided biopsy [8]. We hypothesize that deformations due to needle insertion and biopsy gun firing are different in the context of TRUS-guided biopsy due to several important differences in physical configuration. In contrast to the robotic procedure described in Xu et al. [8], where an endorectal coil in a cylindrical housing is placed parallel to the rectal wall for imaging, TRUS-guided biopsy is typically conducted using an end-firing ultrasound transducer, where the spherical transducer tip is manipulated against the anterior rectal wall in order to obtain images. The MR-guided robot in Xu et al. [8] inserts needles into the prostate through the rectal wall at an oblique angle to the endorectal coil housing, whereas in end-firing TRUS biopsy, the needles are nearly parallel to the probe axis. It is reasonable to expect that these differences in physical configuration may lead to differing mechanical dynamics at the time of biopsy needle insertion and gun firing, resulting in different prostate deformation characteristics. The effect of needle insertion on prostate motion has been studied extensively in the context of brachytherapy procedures [9, 10], where the patient is under general anesthesia and the brachytherapy needles are inserted slowly (relative to the rapid firing speed of a biopsy gun) through the perineum. It is reasonable to consider that the effect of the needle in the context of biopsy may be different due to

the reactions (e.g., in the form of pelvic floor muscle contractions) of an awake, uncomfortable patient and the high speed of needle insertion by the biopsy gun.

The objective of this work was to quantify the deformation caused by the needle insertion and biopsy gun firing procedure. The three main contributions of the present work are: (1) to compute clinically relevant confidence intervals around the tissue deformation, accounting for the measured error in our approach to measuring this deformation; (2) to compare the amount of lateral deformation, in the direction orthogonal to the needle, to the amount of axial deformation, in the direction parallel to the needle; and (3) to compare the deformation resulting from the traditional approach to 2D TRUS-guided biopsy where the probe is hand held with that resulting from the use of mechanically assisted biopsy system [5]. With respect to contribution (1), we computed a spatially varying confidence interval around the amount of tissue deformation induced during these two actions in order to permit the determination the difference between the location sampled by the biopsy needle and the planned target location. This is a useful measure from a clinical standpoint, since this confidence interval can be used to determine the smallest tumour that can be accurately sampled with 95% confidence, under the assumption of zero error in all other aspects of the biopsy system. Our initial work on this problem, addressed this quantification in terms of a spatially varying mean and standard deviation of the deformation magnitudes [11]. With respect to contribution (2), given the long, narrow (19 mm \times 0.8 mm) cylindrical shape of the biopsy core, it is useful to decompose the tissue motion into its axial and lateral components, since axial motion poses less of a problem for targeting, compared to lateral motion. With respect to contribution (3), we hypothesize that the characteristics of prostate deformation may

differ when using a hand held TRUS probe during needle insertion and gun firing, as compared with using our mechanically stabilized system where the interaction between the physician and the system is more controlled.

2.2 Materials and Methods

2.2.1 Data Acquisition

We acquired images using a conventional hand held 2D-TRUS biopsy system and a mechanically assisted 3D TRUS biopsy guidance system developed in our laboratory [5] as part of a larger human subjects research ethics board approved MRI-3D TRUS fusion biopsy study of our institution. This system consists of passive mechanical components for guiding, tracking and stabilizing the position and orientation of a conventional TRUS probe (Figure 2.1). The stabilization is accomplished using a mechanical spring-loaded counter-balancing system that maintains the position and orientation of the probe even when the physician removes his hand from the handle. This permits smooth motion of the transducer with a light touch of the physician's hand. In addition, the configuration of the device is such that there exists a remote center of motion (RCM) at a point near to the tip of the TRUS probe. The RCM is intended to minimize prostate motion during reorientation of the probe to aim for different targets in the biopsy plan.

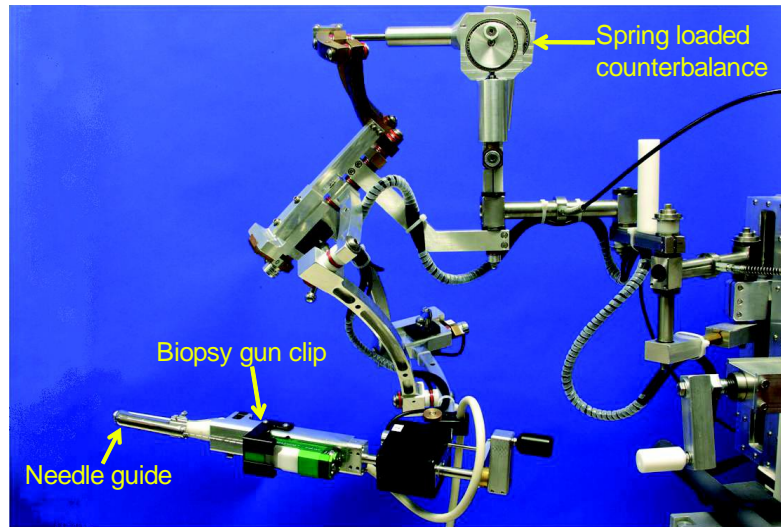


Figure 2.1: Mechanically assisted 3D TRUS-guided biopsy system. The biopsy gun is retained in a clip and the needle is coupled to the TRUS probe using a needle guide. A spring-based counter balancing system maintains probe position and orientation even when the physician removes his hand from the probe.

For both the hand held and mechanically assisted approaches, we used a Philips/ATL HDI 5000 ultrasound machine with a 5-9 MHz end-firing TRUS transducer probe (model C9-5, Philips, Bothell, WA, USA) to acquire images, and a Magnum biopsy gun (C. R. Bard, AZ, USA) to take biopsy samples. We utilized a video capture board to acquire and digitize video from the ultrasound machine's composite video output at a minimum of 10 Hz, recording the 2D ultrasound images (with isotropic pixels of size 0.19 mm) obtained during the entire biopsy procedure for each patient. Across 16 patients, $N_s = 190$ biopsies were obtained (i.e., an average of 12 biopsies per patient). 96 biopsies were taken from 9 patients using the hand held system, and 94 biopsies were taken from 7 patients using the mechanically assisted system. For each biopsy, we manually selected 3 video frames, denoting each frame triplet as a biopsy *sequence*, each of which is assigned a number s between 1 and N_s . The sequence consists of (1) the image I_{s1} acquired immediately prior to needle insertion, (2) the image I_{s2} acquired

immediately prior to biopsy gun firing, and (3) the image I_{s3} acquired immediately after biopsy gun firing (Figure 2.2). Formally, $I_{s1}: \Omega \rightarrow \mathbb{R}$, where $i \in \{1,2,3\}$, $s \in \{1 \dots N_s\}$, and $\Omega \subset \mathbb{R}^2$ represents the domain of the image.

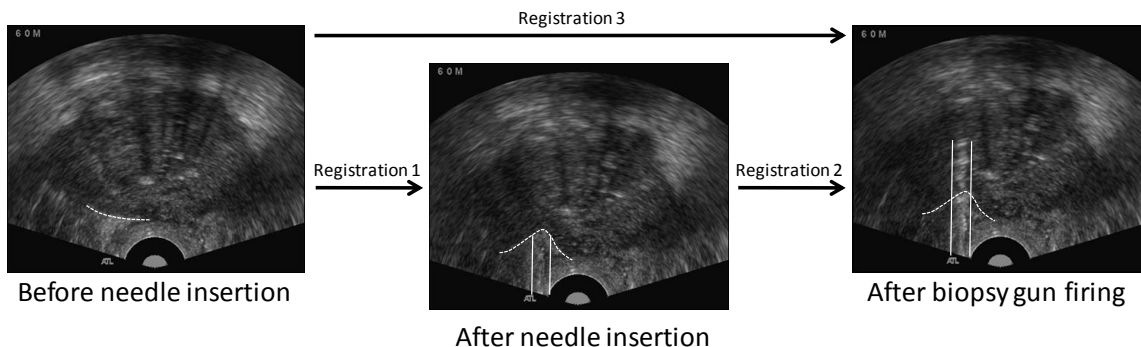


Figure 2.2: Images in a biopsy sequence, and the names used for the three indicated registrations throughout this paper. The first image occurs immediately prior to the physician's insertion of the biopsy needle. The second image occurs immediately prior to firing the biopsy gun, and the third image occurs immediately after the biopsy gun has been fired. The dotted curves indicate portions of the prostate boundary that interact with the needle, which lies between the two solid vertical segments in the second and third images; note the deformation at the lower piercing point.

2.2.2 Image registration

Our method is described at a high level in the block diagram given in Figure 2.3. The process begins with the registration of an image pair, where one image is designated as the fixed image, and the other is designated as the moving image. For each biopsy sequence, we performed three such registrations, described in Figure 2.3. Throughout the remainder of this paper, for a biopsy sequence s , registration 1 refers to the registration of I_{s1} to I_{s3} and reports the combined deformation resulting from both the needle insertion and the biopsy gun firing procedures. Registration 2 refers to the registration of I_{s1} to I_{s2} and reports the deformation resulting from needle insertion only. Registration 3 refers to the registration of I_{s2} to I_{s3} and reports the deformation resulting from biopsy gun firing only. For each indicated image pair, we designated the image at the earlier time point as the moving image and the image at the later time point as the fixed image, since these

designations reflect the movement of the tissue through time during the procedure. We normalized the images with respect to the position of the biopsy needle by flipping the images (if necessary) so that the needle lies to the left of the probe; this normalization allows for the straightforward quantification of deformation with respect to measured spatial distances to the needle. We then non-rigidly registered the moving image to the fixed image, yielding a deformation vector field that we used to quantify the tissue deformation captured by the registration. The deformation field resulting from registration r of biopsy sequence s is denoted $V_{sr}: \Omega \rightarrow \mathbb{R}^2$ and gives the magnitude and direction of deformation at each location in the image domain. We refer to the lateral (x) and axial (y) components of the deformation field as $V_{sr}^x: \Omega \rightarrow \mathbb{R}$ and $V_{sr}^y: \Omega \rightarrow \mathbb{R}$, respectively; Figure 2.4 provides an illustration of the magnitudes of V_{sr} , V_{sr}^x , and V_{sr}^y for one sequence. We tested the following three registration algorithms, with the specified tuning parameters: (1) Demons [12] (standard deviation of smoothing kernel: 1 mm, number of histogram levels: 1024, number of match points: 7), symmetric forces Demons [13] (using the same parameters as for the Demons algorithm) and B-spline [14] (B-spline order: 3, grid spacing: 0.72 mm, similarity metric: normalized cross correlation).

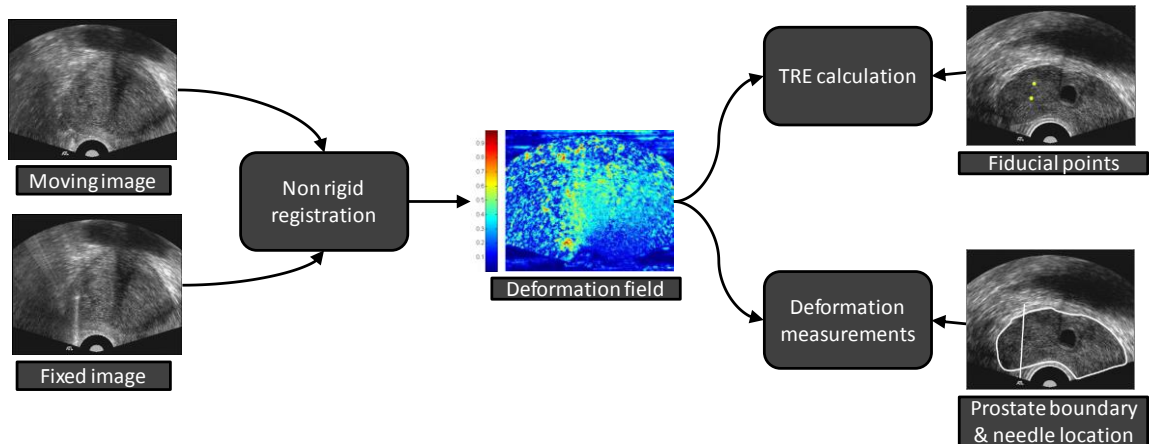


Figure 2.3: Overall process used in this work. The moving image (from an earlier time point) is registered to the fixed image (from a later time point) using non-rigid registration. This yields a deformation vector field that is used to quantify the underlying motion of the tissue. The error in the non-rigid registration algorithm is measured by calculating a TRE based on corresponding intrinsic fiducial markers. Measurements, incorporating the TRE, are then taken from the deformation vector field to characterize the underlying motion of the prostate tissue in response to the insertion of the biopsy needle and firing of the biopsy gun.

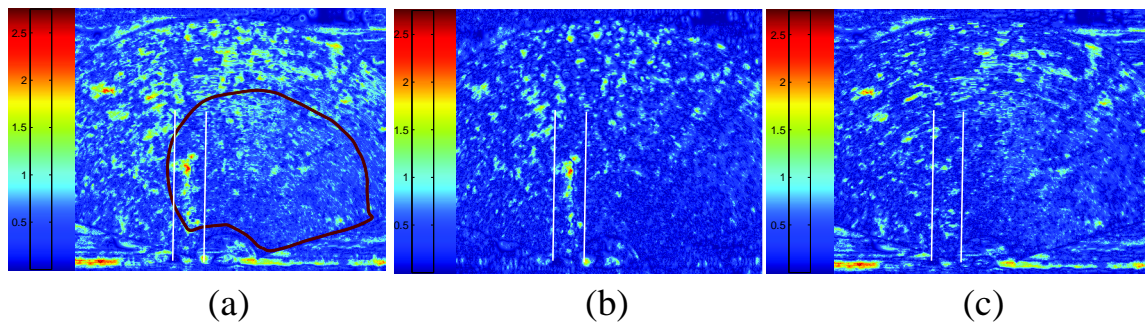


Figure 2.4: (a) Deformation vector field magnitude with prostate boundary and needle location indicated. (b) Lateral (x) components of the deformation field. (c) Axial (y) components of the deformation field. The needle axis lies between the vertical white line in each image.

2.2.3 Image registration validation

The accuracy of a deformation vector field in describing the motion of the tissue depicted in the registered images is influenced by the error of the registration algorithm that generated the deformation vector field. We evaluated each image registration algorithm by estimating its TRE using manually marked, anatomically homologous intrinsic fiducial markers (naturally occurring calcifications) visible in a subset of the images to be registered (Figure 2.5). The TRE is calculated as the RMS error of the spatial locations

of corresponding fiducials, post-registration [15]. To compute the TRE for each algorithm, we performed registrations 1, 2, and 3 on 21 biopsy sequences taken from 4 patients. A total of 390 fiducials were identified and localized in the tested images. To determine the location of each fiducial, an operator localized the fiducial five times during separate sessions, and the centroid (arithmetic mean) of the operator's five selected locations was taken as the estimate of the location of the fiducial. These repeated localizations were also used to compute the fiducial localization error (FLE) as $FLE = \sqrt{\frac{1}{N} \sum_k FLE_k^2}$, where $FLE_k^2 = \sigma^2(x_k) + \sigma^2(y_k)$, and $\sigma^2(x_k)$ and $\sigma^2(y_k)$ are the variances of the x - and y -coordinates, respectively, of the repeated localizations of the k^{th} fiducial.

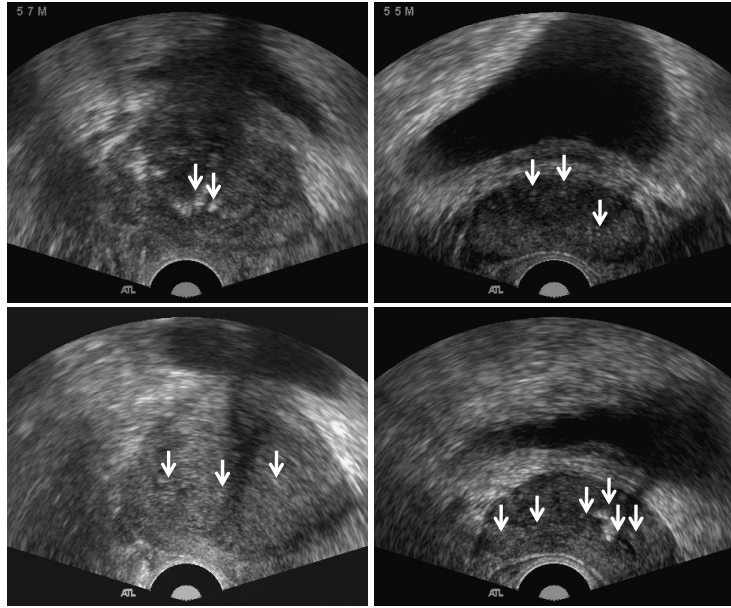


Figure 2.5: Calcifications used to validate the registration algorithms, indicated by arrows.

2.2.4 Quantification of deformation

A clinical objective of image-guided prostate biopsy is to obtain tissue samples from regions of the prostate defined as biopsy targets. In conventional 2D TRUS-guided

biopsy, these targets may be determined according to a predefined pattern (e.g., as in sextant biopsy), or may be determined at time of biopsy based on a visual assessment of the ultrasound image by the physician. In 3D TRUS-guided systems [3, 5], targets may be determined via the physician's assessment of an image of a different modality (e.g., MRI) or based on biopsy targets in a previous 3D TRUS-guided biopsy session [7]. Regardless of the means of defining the target, the physician will insert the biopsy needle through the rectal wall with a trajectory intersecting with the target, advancing the needle tip sufficiently such that the target lies within the throw of the biopsy gun, and then activate the trigger to fire the gun and obtain a sample. It is therefore of interest to quantify the deformation of the prostate tissue proximal to the trajectory of the needle throughout this procedure, in order to determine how far the target may move from the needle path. There are two key aspects to this quantification: (1) defining the appropriate statistical descriptions of the deformation field to characterize the underlying tissue motion within a confidence interval, and (2) defining relevant spatial regions within which these statistics are to be calculated. We define the statistics in Section 2.2.4.1 and the spatial regions in Section 2.2.4.2. In Section 2.2.4.2, we describe the specific measurements computed in this paper using the defined statistics and regions.

2.2.4.1 Deformation vector field statistics

We calculated three statistics: (1) a signed mean of the deformation vector field, to measure coherent tissue motion in some direction; (2) a standard deviation of the vector field, to obtain a confidence interval around the amount of deformation observed in the tissue; and (3) a standard deviation of the vector field that incorporates the measurement error given by the TRE.

Statistic 1: Signed mean of the deformation field. This statistic was computed by summing each of the two signed components of the deformation vectors independently, and squaring and adding the results to obtain a measure of coherence in the motion depicted by the deformation vector field. The signed mean distance across all sequences for a particular registration r (1, 2 or 3) is defined as

$$\bar{D}_r(P) = \left\| \frac{1}{N_s} \sum_{s=1}^{N_s} \left(\frac{1}{|P_s|} \sum_{i=1}^{|P_s|} V_{sr}(\mathbf{p}_i \in P_s) \right) \right\|, \quad (2.1)$$

where $P = \{P_1, P_2, \dots, P_{N_s}\}$ is a set of point sets, one per sequence, and $|P_s|$ is taken to be the cardinality of set P_s . The parameter P allows for the specification of the region of the deformation vector field over which the statistic is to be computed. The elements of P allow for the definition of a different region for each sequence.

Statistic 2: Standard deviation of the deformation field. The standard deviation of the distribution of deformation vectors for all sequences for a registration r is

$$\tilde{\sigma}_r(P) = \sqrt{\widehat{D}_r(P)^2 - \bar{D}_r(P)^2}, \quad (2.2)$$

where the RMS of the deformation is defined as

$$\widehat{D}_r(P) = \frac{1}{N_s} \sum_{s=1}^{N_s} \left(\frac{1}{|P_s|} \sum_{i=1}^{|P_s|} \|V_{sr}(\mathbf{p}_i \in P_s)\| \right). \quad (2.3)$$

The standard deviation $\tilde{\sigma}_r(P)$ is a useful statistic in that it permits the calculation of a confidence interval around the amount of tissue motion in a region of interest defined by P . However, $\tilde{\sigma}_r(P)$ represents the variability of the deformation of the prostate tissue under the assumption of zero measurement error, i.e., zero TRE. Our motivation for performing this calculation is to compare it with the analogous calculation (defined in the next paragraph) that incorporates the TRE, in order to assess the impact of the registration error on the computed confidence interval on the estimated tissue motion.

Statistic 3: Standard deviation of the deformation field, incorporating the

TRE. In a given registration of a moving image to a fixed image, every point in the moving image has an anatomically homologous point in the fixed image to which it would be transformed by an ideal registration algorithm. In practice, a given registration algorithm transforms each point in the moving image to a point which is some (possibly nonzero) distance away from its anatomically homologous point in the fixed image. If we define the anatomically homologous point given by the ideal registration algorithm as our “true target”, the error of a non-ideal registration algorithm places the transformed points from the moving image around the true target according to some distribution. Under the assumption that this distribution is normal, the TRE gives an estimate of its standard deviation. Deformation vector fields generated by a registration algorithm with a nonzero TRE therefore give an approximate measure of the deformation of the tissue, which is reflected in a larger confidence interval on the estimated tissue deformation due to needle insertion and biopsy gun firing. The TRE, measured as an RMS error, adds uncertainty regarding the tissue motion to the uncertainty described by the measured standard deviation of the deformation vector field. These uncertainties are combined by taking their quadratic sum [16] as

$$\sigma_r(P) = \sqrt{\tilde{\sigma}_r(P)^2 + TRE^2}, \quad (2.4)$$

The 95% confidence interval on the magnitude of the prostate tissue displacement is given by $1.96\sigma_r(P)$. To measure the tissue deformation along the lateral (x) and axial (y) directions separately, we computed

$$\sigma_r^x(P) = \sqrt{\tilde{\sigma}_r^x(P)^2 + (TRE^x)^2} \text{ and} \quad (2.5)$$

$$\sigma_r^y(P) = \sqrt{\tilde{\sigma}_r^y(P)^2 + (TRE^y)^2}, \quad (2.6)$$

respectively, where TRE^x and TRE^y are the dimensional components of the TRE, and

$$\begin{aligned} \tilde{\sigma}_r^x(P) &= \sqrt{\widehat{D}_r^x(P)^2 - \bar{D}_r^x(P)^2}, \\ \bar{D}_r^x(P) &= \left\| \frac{1}{N_s} \sum_{s=1}^{N_s} \left(\frac{1}{|P_s|} \right) \sum_{i=1}^{|P_s|} V_{sr}^x(\mathbf{p}_i \in P_s) \right\|, \end{aligned}$$

$$\widehat{D}_r^x(P) = \frac{1}{N_s} \sum_{s=1}^{N_s} \left(\frac{1}{|P_s|} \sum_{i=1}^{|P_s|} \|V_{sr}^x(\mathbf{p}_i \in P_s)\| \right).$$

(and similarly for the y dimension).

2.2.4.2 Measured regions

We calculated the statistics of deformation vector fields lying within three different types of image regions: (1) regions at a specific signed distance to the needle axis, (2) regions within an unsigned distance of the needle axis, and (3) regions at a specific unsigned distance to the point where the biopsy needle enters the prostate (henceforth referred to as the *lower piercing point*).

Region 1: Deformation vectors at a signed distance to the needle axis. The set of points in the image domain lying at a distance d from the needle axis A for sequence s is defined as

$$P_{sd}^A = \{\mathbf{p}_i \in \Omega \mid D_A(A_s, \mathbf{p}_i) = d\}, \quad (2.7)$$

where

$$A_s = \{\mathbf{l}_s + t\mathbf{a}_s \mid t \in \mathbb{R}\},$$

defines the needle axis for sequence s , with \mathbf{l}_s defining the lower piercing point and \mathbf{a}_s defining the needle axis direction. $D_A(A_s, \mathbf{p}_i)$ gives the signed perpendicular distance

between \mathbf{p}_i and the needle axis, with negative distance values defined for points lying to the left of the needle axis. $P_d^A = \{P_{1d}^A, P_{1d}^A, \dots, P_{N_s d}^A\}$ the set of such regions at distance d for all sequences.

Region 2: Deformation vectors within an unsigned distance of the needle axis.

The set of points from sequence s in the image domain lying within a region of the needle axis (“axis region” denoted as AR) defined by a distance d is defined as

$$P_{sd}^{AR} = \{\mathbf{p}_i \in \Omega \mid D_A(A_s, \mathbf{p}_i) \leq d\}. \quad (2.8)$$

$P_d^{AR} = \{P_{1d}^{AR}, P_{1d}^{AR}, \dots, P_{N_s d}^{AR}\}$, the set of such regions at distance d for all sequences.

Region 3: Deformation vectors at a specific unsigned distance to the lower piercing point. The set of points in the image domain lying at a distance d from the lower (denoted as “ l ”) piercing point for sequence s is defined as

$$P_{sd}^l = \{\mathbf{p}_i \in \Omega \mid D_l(\mathbf{l}_s, \mathbf{p}_i) = d\}, \quad (2.9)$$

where $D_l(\mathbf{l}_s, \mathbf{p}_i)$ gives the unsigned Euclidean distance between \mathbf{p}_i and the lower piercing point. $P_d^l = \{P_{1d}^l, P_{1d}^l, \dots, P_{N_s d}^l\}$, the set of such regions at distance d for all sequences.

2.2.4.3 Prostate tissue deformation measurements

Using the statistics and regions defined above, we computed four different measures of prostate tissue deformation, defined in the paragraphs below.

Measurement 1: Deformation as a function of distance to the needle axis. The signed mean, $\bar{D}_r(P_d^A)$, the standard deviation, $\tilde{\sigma}_r(P_d^A)$, and the standard deviation incorporating the TRE, $\sigma_r(P_d^A)$, were determined for regions P_d^A at specific signed distances d to the needle axis (Figure 2.6). These measurements were performed

separately for $r = 1,2,3$, with $d = [-15 \text{ mm}, 50 \text{ mm}]$, a sufficiently large domain to cover all of the prostates in our study. The purpose of these measurements was to find the 95% confidence interval ($1.96\sigma_r(P_d^A)$) on the estimated prostate tissue motion, as well any directionally coherent tissue motion ($\bar{D}_r(P_d^A)$), as a function of distance to the needle axis. Since the biopsy target is presumably near to the needle axis, these measurements allow for the interrogation of a region of clinical interest to determine the amount by which the tissue may move away from the needle during biopsy. Comparing the 95% confidence interval on the tissue motion that incorporates the measured TRE with the corresponding confidence interval computed under the assumption of zero TRE permits the assessment of the effect of the registration error on the confidence interval estimate.

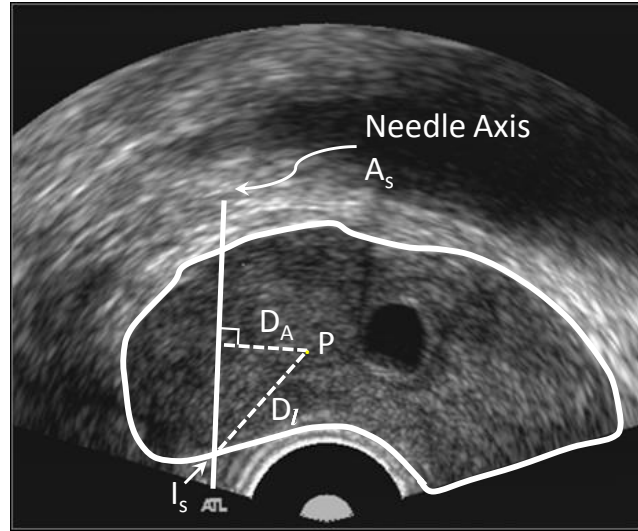


Figure 2.6: Diagram depicting a prostate contoured on a 2D TRUS image with the needle axis A_s to the left of the probe, as in all of our images. The perpendicular distance D_A of a point P to the needle axis is shown. The lower piercing point l_s is indicated, as is the distance D_l between P and the lower piercing point.

Measurement 2: Deformation as a function of distance to the lower piercing point. The signed mean, $\bar{D}_r(P_d^l)$, the standard deviation, $\tilde{\sigma}_r(P_d^l)$, and the standard deviation incorporating the TRE, $\sigma_r(P_d^l)$, were determined for regions P_d^l at specific

unsigned distances d to the lower piercing point (Figure 2.6). These measurements were performed separately for $r = 1, 2, 3$, with $d = [0 \text{ mm}, 30 \text{ mm}]$, a sufficiently large domain to cover all of the prostates in our study. The purpose of these measurements was to find the 95% confidence interval ($1.96\sigma_r(P_d^l)$) on the estimated prostate tissue motion, as well as any directionally coherent tissue motion ($\bar{D}_r(P_d^l)$), as a function of distance to the lower piercing point. These measurements allow for the comparison of the amounts by which the tissue may move away from the biopsy needle when the target is proximal to the piercing point (e.g., target A in Figure 2.7), and when the target is far from the piercing point (e.g., target B in Figure 2.7). This is particularly important since up to 80% of prostate cancer is found in the peripheral zone [17, 18], which lies near to the posterior side where the biopsy needle enters the prostate after penetrating the rectal wall (Figure 2.7).

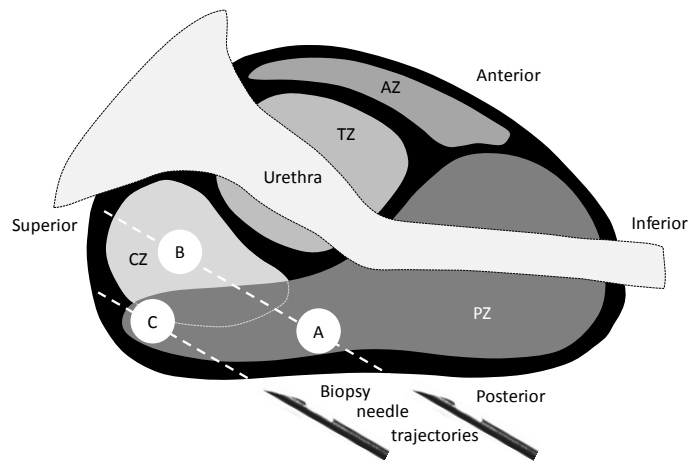


Figure 2.7: Diagram depicting prostate anatomy in a sagittal view, indicating the peripheral zone (PZ), central zone (CZ), transition zone (TZ), and anterior zone (AZ). Three biopsy targets are shown as A, B, and C. The biopsy needle enters the prostate on the posterior side by penetrating the rectal wall, as shown.

Measurement 3: Deformation in the lateral and axial directions. The standard deviations incorporating the TRE along the lateral (x) and axial (y) directions for registration 1, computed as $\sigma_1^x(P_d^A)$ (Equation 2.5) and $\sigma_1^y(P_d^A)$ (Equation 2.6),

respectively, were determined for regions P_d^A at specific signed distances d to the needle axis (Equation 2.7). $\sigma_1^x(P_d^l)$ and $\sigma_1^y(P_d^l)$ are also calculated for regions P_d^l at specific unsigned distances d to the lower piercing point (Equation 2.9). These give decompositions of the two quantifications described above into the lateral and axial directions. The observation of these decompositions is useful because of the highly anisotropic (long, narrow) nature of the biopsy core; axial tissue motion parallel to the needle poses less of a problem with respect to targeting than does lateral tissue motion.

Measurement 4: Deformation as a function of lateral position of the needle relative to the prostate. The standard deviation incorporating the TRE, computed as $\sigma_1(P_{5mm}^{AR})$, was determined for the region P_{5mm}^{AR} within 5 mm of the needle axis (Equation 2.8). This was calculated for registration 1 as a function of w , the lateral position of the needle normalized with respect to the width of the prostate as seen on the 2D TRUS image. At the boundary of the prostate on the 2D TRUS image on the left side of the needle, $w = 0$, in the middle of the prostate, $w = 0.5$, and at the boundary of the prostate on the right side of the needle, $w = 1$. The purpose of this measurement is to investigate the relationship (if any) between the distance of the target from the edge of the prostate, and the amount of tissue deformation that occurs within a clinically meaningful distance of the needle axis. This is illustrated by Figure 2.7; this measurement permits the determination of the difference in deformation when aiming the needle for target A (closer to the middle of the prostate), compared to target C (closer to the edge of the prostate).

2.3 Results

2.3.1 Image registration validation

Table 1 shows the measured TRE values before and after registration for each of the tested algorithms. The symmetric forces Demons registration algorithm was selected for use in this study since it provided the best overall improvement in the TRE. This algorithm is based on optical flow techniques, which have been shown to be suitable for tracking fine-scale structure in ultrasound images in the presence of small tissue deformation [19]; this class of algorithms is therefore suitable for our problem. The calculated FLE was 0.11 mm.

Table 2.1: Comparison of TRE before and after registration for each tested registration method. Registration 1 captures tissue motion during needle insertion and biopsy gun firing, registration 2 captures needle insertion only, and registration 3 captures biopsy gun firing only.

Registration method	Registration 1 TRE (mm)	Registration 2 TRE (mm)	Registration 3 TRE (mm)
Before registration	0.51	0.31	0.40
Demons [12]	0.24	0.13	0.23
Symmetric Forces Demons [13]	0.23	0.14	0.22
B-spline [14]	0.46	0.28	0.37

2.3.2 Quantification of deformation

Measurement 1: Deformation as a function of distance to the needle axis. Figure 2.8 plots the mean deformation, $\bar{D}_r(P_d^A)$, the 95% confidence interval, $1.96\tilde{\sigma}_r(P_d^A)$, and the 95% confidence interval incorporating the TRE, $1.96\sigma_r(P_d^A)$, versus the signed distance d to the needle axis. It can be observed that the coherent tissue motion is relatively small compared to the total amount of deformation (comparing the lowermost curve to the uppermost curve), and that the TRE makes a relatively small contribution to the width of the 95% confidence interval (comparing the middle curve to the uppermost curve). A

local increase in deformation proximal to the needle axis is observed for both systems, with biopsy gun firing being the main contributor to this deformation for the hand held system, and the only contributor for the mechanically assisted system. A two-tailed t-test showed that $1.96\sigma_r(P_d^A)$ was statistically significantly different when comparing the hand held system to the mechanically assisted system ($p < 0.05$), for $|d| < 20$ mm.

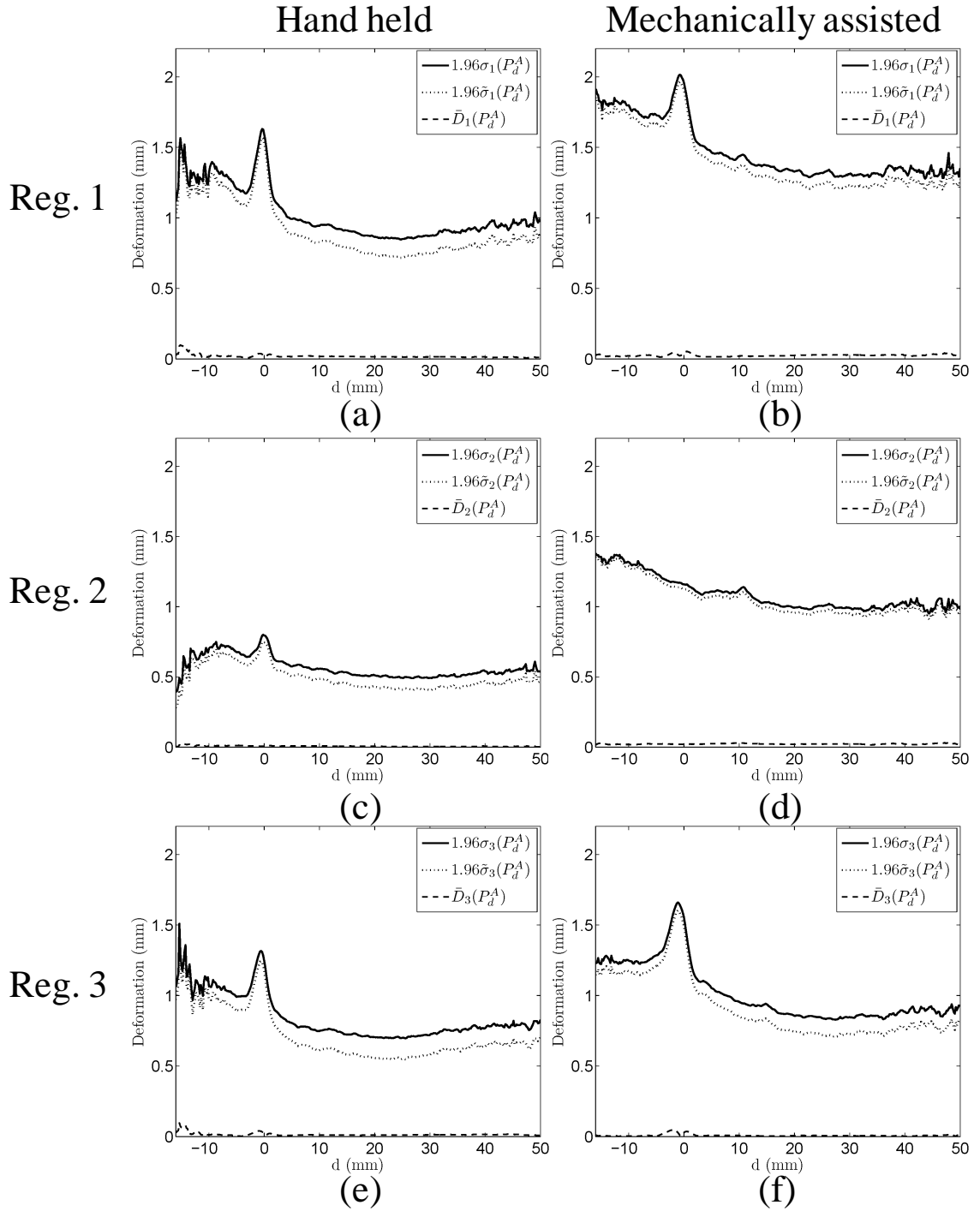


Figure 2.8: Deformation versus distance to the needle axis. Dashed curve: the signed mean of the deformation ($\bar{D}_r(P_d^A)$). Dotted curve: the 95% confidence interval around the tissue deformation ($\bar{\sigma}_r(P_d^A)$). Solid curve: the 95% confidence interval incorporating the TRE ($\sigma_r(P_d^A)$). (a, b): registration 1, (c, d): registration 2, (e, f): registration 3. (a, c, e): hand held, (b, d, f): mechanically assisted.

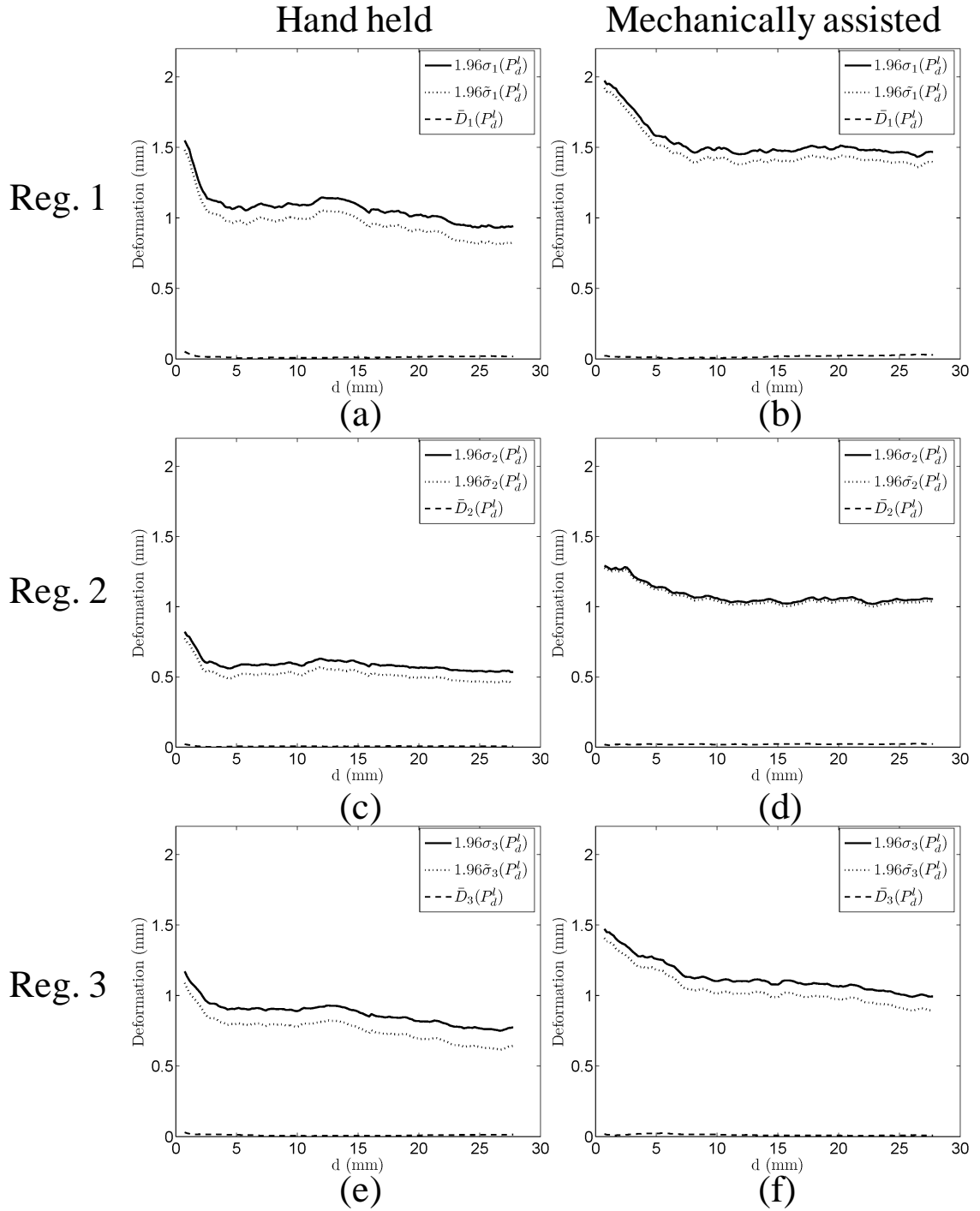


Figure 2.9: Deformation versus distance to the lower piercing point. Dashed curve: the signed mean of the deformation ($\bar{D}_r(P_d^l)$). Dotted curve: the 95% confidence interval around the tissue deformation ($\tilde{\sigma}_r(P_d^l)$). Solid curve: the 95% confidence interval incorporating the TRE ($\sigma_r(P_d^l)$). (a, b): registration 1, (c, d): registration 2, (e, f): registration 3. (a, c, e): hand held, (b, d, f): mechanically assisted.

Measurement 2: Deformation as a function of distance to the lower piercing

point. Figure 2.9 plots the mean deformation, $\bar{D}_r(P_d^l)$, the 95% confidence interval, $1.96\tilde{\sigma}_r(P_d^l)$, and the 95% confidence interval incorporating the TRE, $1.96\sigma_r(P_d^l)$, versus the signed distance d to the needle axis. As in Figure 2.8, it can be observed that the coherent tissue motion is small relative to the total amount of deformation and that the TRE is not a substantially contributing factor. It can also be observed that in general, more deformation occurs proximal to the lower piercing point. A two-tailed t-test showed that $1.96\sigma_r(P_d^l)$ was statistically significantly different when comparing the hand held system to the mechanically assisted system ($p < 0.05$), for $d \geq 1$ mm.

Measurement 3: Deformation in the lateral and axial directions. Figure 2.10(a-b) plot the 95% confidence interval on the tissue deformation, $1.96\sigma_1(P_d^A)$, versus distance to the needle axis, and its lateral and axial components, $1.96\sigma_1^x(P_d^A)$ and $1.96\sigma_1^y(P_d^A)$, respectively. Figure 2.10(c-d) plot the 95% confidence interval on the tissue deformation, $1.96\sigma_1(P_d^l)$, versus distance to the lower piercing point, and its lateral and axial components, $1.96\sigma_1^x(P_d^l)$ and $1.96\sigma_1^y(P_d^l)$, respectively. It can be observed that the deformation is predominantly in the lateral (x) direction proximal to the needle axis (a-b). Proximal to the lower piercing point (c-d), the situation is the opposite, with dependence predominantly in the axial (y) direction.

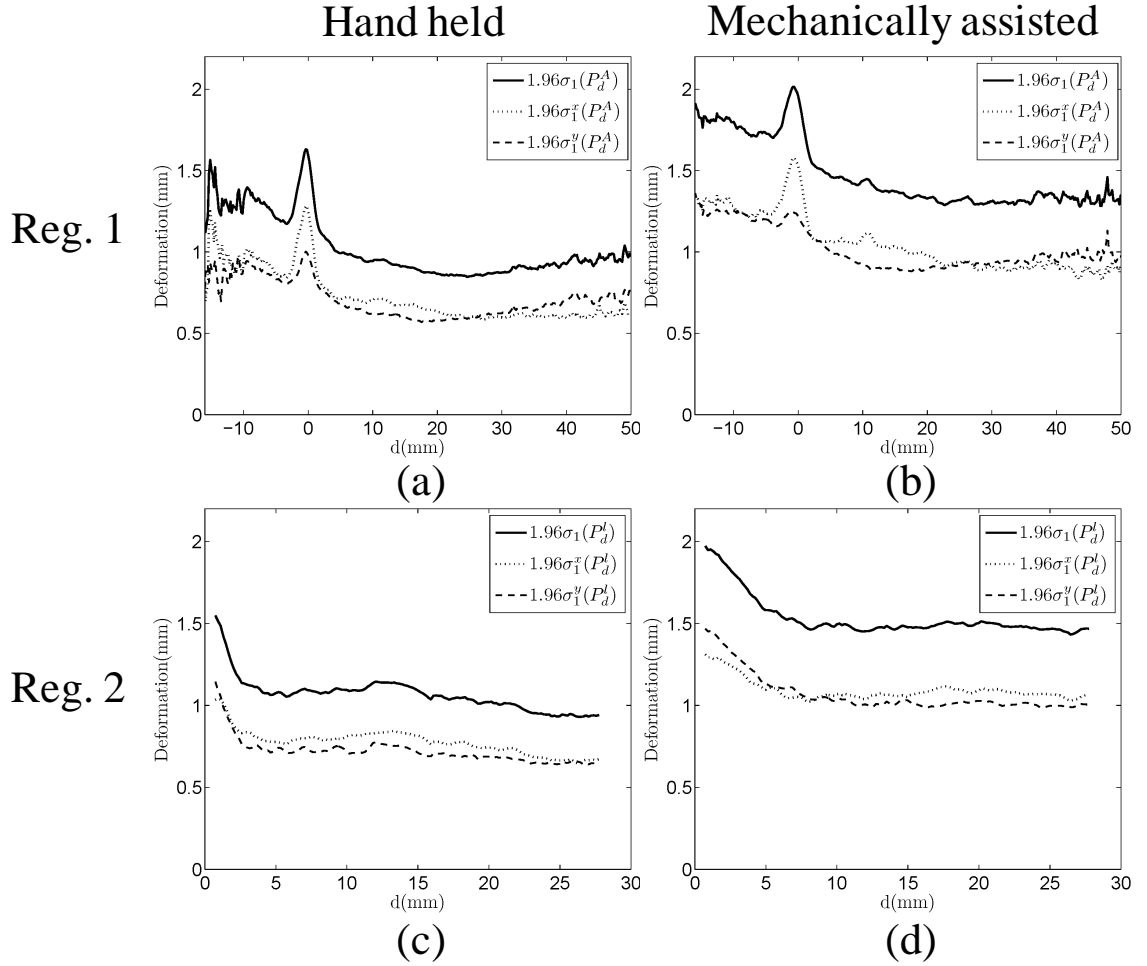


Figure 2.10: Lateral-axial decompositions of the 95% confidence intervals shown in Figures 8 and 9, for registration 1. (a, b): Deformation versus distance to the needle axis. Solid curve: the 95% confidence interval around the tissue deformation incorporating the TRE ($\sigma_r(P_d^A)$). Dashed curve: the lateral (x) component of this confidence interval ($\sigma_1^x(P_d^A)$). Dotted curve: the axial (y) component ($\sigma_1^y(P_d^A)$). (c, d): Deformation versus distance to the lower piercing point. Solid curve: the 95% confidence interval around the tissue deformation incorporating the TRE ($\sigma_r(P_d^L)$). Dashed curve: the lateral (x) component of this confidence interval ($\sigma_1^x(P_d^L)$). Dotted curve: the axial (y) component ($\sigma_1^y(P_d^L)$). (a, c): hand held, (b, d): mechanically assisted.

Measurement 4: Deformation as a function of lateral position of the needle

relative to the prostate. Figure 2.11 plots the 95% confidence interval on the tissue deformation in the region within 5 mm of the needle axis, $1.96\sigma_1(P_{5mm}^{AR})$ as a function of the position of the biopsy needle relative to the left edge of the prostate as seen on the 2D TRUS image (0 is the left edge, 1 is the right edge, and 0.5 is the middle). Since the

needle is consistently oriented to the left side of the probe in our images, most of the plotted points are at less than 0.5 on the horizontal axis. The correlation ratio was found to be -0.17, with a 95% confidence interval of (-0.07, -0.27). The relationship is weak, negative as shown in Figure 2.11.

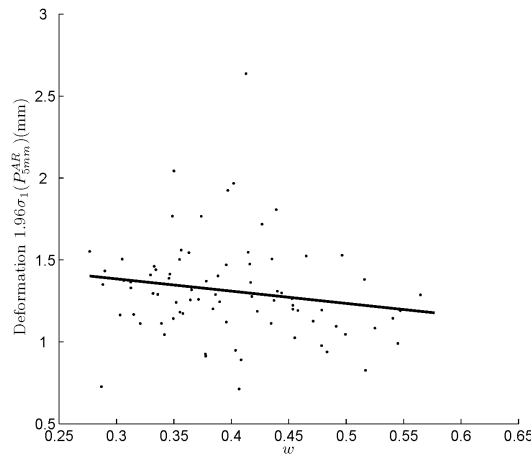


Figure 2.11: Deformation as a function of lateral position of the needle relative to the prostate, for registration 1. The distance to the left edge of the prostate is shown on the horizontal axis (0 = left edge, 0.5 = middle, 1 = right edge). The vertical axis shows the width of the 95% confidence interval on the tissue deformation within a region lying 5 mm on either side of the needle axis ($\sigma_1(P_{5mm}^{AR})$). The best fit line is plotted, showing a weak negative relationship ($r = -0.17$).

2.4 Discussion

2.4.1 Image registration validation

The measured TRE values before and after registration using the symmetric forces Demons algorithm demonstrate that the registrations improve the alignment of the fiducial markers for registrations 1, 2, and 3. Overall, for registration 1 (capturing tissue deformation occurring during needle insertion and biopsy gun firing), 55% of the pre-registration fiducial misalignment is eliminated by the algorithm. For registrations 2 (needle insertion only) and 3 (biopsy gun firing only), 55% and 45% of the pre-registration fiducial misalignment is eliminated, respectively, suggesting that the algorithm was most challenged by the registration of the images occurring before and

after biopsy gun firing. Although the FLE accounts for less than half of the TRE for the overall biopsy procedure (registration 1), it contributes non-trivial variability, suggesting that the actual TRE of this algorithm may in fact be lower than our measurements suggest. Our reported confidence intervals are therefore likely to be conservative.

2.4.2 Quantification of deformation

Measurement 1: Deformation as a function of distance to the needle axis. We observe a maximum value of $1.96\sigma_1(P_d^A) = 2.1$ mm, occurring at $d = 0$, across both systems. Consequently, spherical tumours with radius 2.1 mm or more can be sampled with 95% confidence, under the assumption of zero error elsewhere in the biopsy system. Although $1.96\sigma_1(P_d^A)$ has a higher plateau for the mechanically assisted system, compared to the hand held system, the difference in deformation in the region along the needle axis is less than 0.38 mm. This slight increase in deformation may be explained by the fact that the mechanical system, due to its stabilization of the ultrasound probe, does not require the physician to maintain constant inward pressure on the probe to keep it within the rectum with good acoustic coupling to the prostate. Although this stabilization can reduce the amount of deformation applied to the prostate as the probe is reoriented to aim for different targets, the reduced pressure on the prostate may permit the observed increase in tissue motion during needle insertion and biopsy gun firing. In addition, there is less variability arising from the mechanical system in the deformation on the lateral side of the prostate, to the left of the needle axis (compare Figure 2.8(a,e) to Figure 2.8(b,f) for $d < 0$). Feedback from our collaborating radiologist suggests that this may be due to the mechanical system's stability in the absorption of recoil when the

biopsy gun is fired; recall that the mechanically assisted system holds the biopsy gun in a clip, allowing its mechanical assembly to stabilize the gun and needle during firing. In the hand held system, the physician may be inclined to proactively compensate for recoil by driving the biopsy gun forward slightly at the time of firing, causing the observed lateral deformation variability. Additionally, there exists a relative increase in deformation in the region surrounding the needle axis for the hand held system during needle insertion (peak in the curve at $d = 0$ in Figure 2.8(c)); this does not occur in the mechanically assisted system (no peak in the curve at $d = 0$ in Figure 2.8(d)). This may be due to a slower speed of needle insertion in the mechanical system due to the fact that biopsies taken with this system were targeted using a heads-up display, causing the physician to take extra care when setting the initial needle trajectory during penetration of the rectal wall.

Measurement 2: Deformation as a function of distance to the lower piercing point. As was observed with the deformation relative to the needle axis, the deformation relative to the lower piercing point, $1.96\sigma_1(P_d^l)$, is 0.38 mm higher in the mechanically assisted system, compared with the hand held system. Overall, the mechanically assisted approach yields a deformation that is less dependent on the distance from the lower piercing point, compared with the hand held approach (flatter curves in Figure 2.9(b, d, f), compared with Figure 2.9(a, c, e)).

Measurement 3: Deformation in the lateral and axial directions. At $d = 0$, the ratio of $\sigma_1^x(P_d^A)$ to $\sigma_1^y(P_d^A)$ is 1.2 for the mechanically assisted system, and 1.3 for the hand held system. The observed lateral tissue motion proximal to the needle shaft is expected, since tissue must be displaced laterally in order to accommodate the insertion

of the biopsy needle into the prostate; this observation provides qualitative support for the plausibility of the deformation vector fields generated by our chosen registration algorithm. This analysis is motivated by the long, narrow shape of the biopsy core, so it is of value to observe the 95% confidence interval around the lateral tissue motion along the needle axis. This quantity is 1.3 mm for the hand held system and 1.5 mm for the mechanically assisted system. In both systems, the ratio of $\sigma_1^y(P_d^l)$ to $\sigma_1^x(P_d^l)$ is greater than one proximal to the lower piercing point; this dependence is in the axial direction, parallel to the needle axis, and so is of little concern given the shape of the biopsy core.

Measurement 4: Deformation as a function of lateral position of the needle relative to the prostate. The observed weak negative relationship between $1.96\sigma_1(P_{5mm}^{AR})$ and the lateral position of the biopsy needle relative to the prostate suggests that although the tissue medial to the prostate may be more stable during biopsy, compared with the tissue nearer to the sides, this effect is not large enough to warrant compensation during targeting.

2.4.3 Limitations

One limitation of this work arises due to the fact that obtaining images at a suitable frame rate to capture the deformation occurring during rapid biopsy gun firing necessitates the use of 2D, rather than 3D, TRUS imaging. We are therefore able to quantify deformation in directions non-parallel to the 2D TRUS imaging plane only indirectly, in several ways. First, because the biopsy sequence images in this study were selected in part due to the presence of visible micro-calcifications for the purposes of quantifying the TRE and FLE, the visibility of such small structures in all three images in each sequence limits the out-

of-plane tissue motion by a function of calcification size and ultrasound beam thickness. Second, the measured in-plane lateral dependence shown in Figure 2.10 suggests a bound on the out-of-plane deformation, under the assumption that it is similar to that which is observed within the 2D TRUS images. Finally, because we quantified the tissue deformation for a large number of biopsies (190) taken during clinical sessions, our in-plane deformation quantifications are on a representative sampling of differently positioned and oriented prostate tissue cross sections imaged by 2D TRUS.

We calculated the TRE using the fiducials located by a single observer over multiple days. One limitation of this approach is that inter-observer variability in fiducial localization is not taken into account. As a step toward assessing this limitation, a second observer located 64 fiducials of four patients five times on five different days. The measured FLE of the second observer (0.09 mm) was similar to that of the first observer (0.12 mm), suggesting that inter-observer variability in fiducial localization may not be a dominant factor.

In order to evaluate the tested registration algorithms and incorporate measurement error into our tissue deformation estimates, we computed a single TRE for each algorithm based on multiple fiducials localized in images of several patients. This approach makes the assumption of a spatially uniform TRE that is invariant to differences between subjects. Although it is theoretically possible to calculate a separate TRE for each subject, each biopsy sequence, and even (via TRE interpolation) each pixel of each registered image pair, such calculations require a sufficiently regular and dense distribution of intrinsic fiducials (calcifications) in every image in order to robustly estimate a spatially-varying TRE for every image pair. With an average of 6.2 naturally

occurring calcifications appearing in each of our tested images, the robustness of an estimate of a spatially-varying TRE for each image is questionable. This motivated the computation of an overall TRE based on 390 fiducials across multiple patients, under the above assumptions.

Another limitation of this work concerns the assumption of the independence of uncertainties in Equation 2.4. Since the TRE of a registration algorithm may have some effect on the standard deviation of the deformation vector fields that it produces, it could be argued that there may be some dependence between these uncertainties. Since the strength of the independence assumption is unclear, it is reasonable to consider the effect on the results if this assumption is not made. In this case, the *upper bound* on the total uncertainty is the ordinary sum of the individual uncertainties [16]; i.e., in our case, $\sigma_r(P)$ would become $\tilde{\sigma}_r(P) + TRE$. Using this extremely conservative approach, we would observe a maximum value of $1.96\sigma_1(P_d^A) = 2.3$ mm, occurring at $d = 0$, across both systems. Consequently, spherical tumours with radius 2.3 mm or more could be sampled with 95% confidence, under the assumption of zero error elsewhere in the biopsy system.

2.5 Conclusion

In this work, we utilized deformation vector fields given by the symmetric forces Demons non-rigid image registration algorithm to quantify the deformation of prostate tissue that occurs during needle insertion and biopsy gun firing. We computed the coherence of the tissue motion as well as the 95% confidence interval around the amount of tissue motion, incorporating the measurement error given by the TRE. We calculated

these statistics in clinically relevant regions of the deformation vector fields in order to observe trends in the deformation as functions of the distances to the needle axis and lower piercing point. We also decomposed the deformation and into its lateral and axial components, and computed the relationship of the deformation to the lateral position of the needle with respect to the prostate. All of these measurements were used to compare the conventional hand held approach to a mechanically assisted biopsy system developed in our laboratory. Overall, we observed a statistically significant, but clinically insignificant, maximum difference of 0.38 mm in the deformation resulting from the hand held and mechanically assisted systems along the needle axis. The mechanical system resulted in a lower relative increase in deformation proximal to the needle axis during needle insertion, as well as lower variability of deformation during biopsy gun firing. The results show that for both systems, the tissue deformation is such that throughout the length of the needle axis, including regions proximal to the lower piercing point, spherical tumours with radius 2.1 mm or more can be sampled with 95% confidence, under the assumption of zero error elsewhere in the biopsy system. Along the needle axis, the deformation was predominantly in the lateral direction; this is of particular importance given the long, narrow shape of the biopsy core. We measured lateral tissue motion proximal to the needle axis of not more than 1.5 mm, with 95% confidence. There was a weak negative relationship between tissue deformation in a local region around the needle and the lateral position of the needle with respect to the prostate; the closer was the needle to the center of the prostate, the less was the observed deformation. Given the clinical need to biopsy tumours of volume greater than or equal to 0.5 cm³,

corresponding to spherical tumours of radius 5 mm or more, the tissue motion induced by needle insertion and gun firing contributes to the overall error of the biopsy system

References

1. K. R. Moreira Leite, L. H. Camara-Lopes, M. F. Dall'Oglio, J. Cury, A. A. Antunes, A. Sanudo and M. Srougi, "Upgrading the Gleason score in extended prostate biopsy: implications for treatment choice," *Int J Radiat Oncol Biol Phys* **73**, 353-356 (2009).
2. D. W. Cool, M. J. Connolly, S. Sherebrin, R. Eagleson, J. I. Izawa, J. Amann, C. Romagnoli, W. M. Romano and A. Fenster, "Repeat prostate biopsy accuracy: simulator-based comparison of two- and three-dimensional transrectal US modalities," *Radiology* **254**, 587-594 (2010).
3. D. Cool, S. Sherebrin, J. Izawa, J. Chin and A. Fenster, "Design and evaluation of a 3D transrectal ultrasound prostate biopsy system," *Med Phys* **35**, 4695-4707 (2008).
4. A. Krieger, R. C. Susil, C. Menard, J. A. Coleman, G. Fichtinger, E. Atalar and L. L. Whitcomb, "Design of a novel MRI compatible manipulator for image guided prostate interventions," *IEEE Trans Biomed Eng* **52**, 306-313 (2005).
5. J. Bax, D. Cool, L. Gardi, K. Knight, D. Smith, J. Montreuil, S. Sherebrin, C. Romagnoli and A. Fenster, "Mechanically assisted 3D ultrasound guided prostate biopsy system," *Med Phys* **35**, 5397-5410 (2008).
6. J. I. Epstein, H. Sanderson, H. B. Carter and D. O. Scharfstein, "Utility of saturation biopsy to predict insignificant cancer at radical prostatectomy," *Urology* **66**, 356-360 (2005).
7. V. V. Karnik, A. Fenster, J. Bax, D. W. Cool, L. Gardi, I. Gyacskov, C. Romagnoli and A. D. Ward, "Assessment of image registration accuracy in three-dimensional transrectal ultrasound guided prostate biopsy," *Med Phys* **37**, 802-813 (2010).
8. H. Xu, A. Lasso, S. Vikal, P. Guion, A. Krieger, A. Kaushal, L. L. Whitcomb and G. Fichtinger, "Accuracy validation for MRI-guided robotic prostate biopsy," in *SPIE Medical Imaging: Visualization, Image-Guided Procedures*, (San Diego, CA, USA, 2010), pp. 762517 - 762517-762518.
9. V. Lagerburg, M. A. Moerland, J. J. Lagendijk and J. J. Battermann, "Measurement of prostate rotation during insertion of needles for brachytherapy," *Radiother Oncol* **77**, 318-323 (2005).
10. N. N. Stone, J. Roy, S. Hong, Y. C. Lo and R. G. Stock, "Prostate gland motion and deformation caused by needle placement during brachytherapy," *Brachytherapy* **1**, 154-160 (2002).
11. T. De Silva, A. Fenster, J. Samarabandu and A. D. Ward, "Quantification of Prostate Deformation due to Needle Insertion during TRUS-guided Biopsy," *Medical Image*

- Computing and Computer-Assisted Intervention - Miccai 2010, Pt Iii **6363**, 213-220 (2010).
12. J. P. Thirion, "Image matching as a diffusion process: an analogy with Maxwell's demons," *Med Image Anal* **2**, 243-260 (1998).
 13. T. Vercauteren, X. Pennec, A. Perchant and N. Ayache, "Symmetric Log-Domain Diffeomorphic Registration: A Demons-Based Approach," *Medical Image Computing and Computer-Assisted Intervention - Miccai 2008, Pt I, Proceedings* **5241**, 754-761 (2008).
 14. D. Rueckert, L. I. Sonoda, C. Hayes, D. L. G. Hill, M. O. Leach and D. J. Hawkes, "Nonrigid registration using free-form deformations: Application to breast MR images," *Ieee T Med Imaging* **18**, 712-721 (1999).
 15. J. M. Fitzpatrick, J. B. West and C. R. Maurer, Jr., "Predicting error in rigid-body point-based registration," *IEEE Trans Med Imaging* **17**, 694-702 (1998).
 16. J. R. Taylor, *Introduction to Error Analysis*, 2 ed. (University Science Books, Sausalito, 1997).
 17. P. Puppo, "Repeated negative prostate biopsies with persistently elevated or rising PSA: a modern urologic dilemma," *Eur Urol* **52**, 639-641 (2007).
 18. O. Haussler, J. I. Epstein, M. B. Amin, P. U. Heitz and S. Hailemariam, "Cell proliferation, apoptosis, oncogene, and tumor suppressor gene status in adenosis with comparison to benign prostatic hyperplasia, prostatic intraepithelial neoplasia, and cancer," *Hum Pathol* **30**, 1077-1086 (1999).
 19. J. Meunier, "Tissue motion assessment from 3D echographic speckle tracking," *Phys Med Biol* **43**, 1241-1254 (1998).

Chapter 3.

2D-3D rigid registration to compensate for prostate motion during 3D TRUS-guided biopsy

3.1 Introduction

With the aim of improving the cancer detection rate, systems have been developed [1, 2] that can plan and record biopsy locations in a 3D TRUS image acquired at the beginning of the biopsy procedure. Although early reports of these systems are promising, some limitations have been identified that require attention [3]. For instance, patient motion and ultrasound probe pressure can cause the prostate to move and deform during the biopsy procedure. In this chapter, we focus on improving the needle targeting accuracy of such systems by compensating for prostate motion during the procedure. Target biopsy locations are usually identified with the assistance of an MR image acquired prior to the biopsy session, in which cancerous regions are more visible. These locations are mapped to the 3D TRUS image acquired during the biopsy session to provide guidance using image information contained in the MR image. The 3D TRUS image can then act as a baseline image, to guide the physician to the target biopsy locations by augmenting the 2D TRUS planes acquired during biopsy with 3D contextual information. However, motion during the procedure could lead to a misalignment between the targets identified in the initially-acquired 3D image and their corresponding locations within the patient's prostate as depicted by the real-time 2D TRUS images acquired throughout the biopsy procedure. Compensating for the prostate motion and deformation by registering the pre-

acquired 3D image to the live 2D images acquired throughout the procedure is an important step toward improving the targeting accuracy.

Previous approaches to compensation for prostate motion during biopsy have involved mechanical stabilization of the ultrasound probe, 3D tracking of the probe, and the use of biplanar or 3D transducers to continuously acquire richer image information supporting software-based motion compensation algorithms [1-5]. The mechanically assisted 3D TRUS-guided biopsy system developed in our laboratory and described in detail in [1], uses a passive mechanical arm to track the position and orientation of the ultrasound probe during the biopsy procedure. The design yields a remote centre of motion positioned at the centre of the ultrasound probe tip that provides enhanced stability to the US probe minimizing prostate motion. Several methods have been proposed in similar 3D TRUS-guided biopsy systems to register real-time TRUS images during the procedure to an initially acquired 3D image [2, 4, 5]. The 3D TRUS-guided biopsy system presented in Xu et al. [2] uses a magnetic tracking method to locate the ultrasound plane and it then performs an intermittent rigid registration to compensate for *out-of-plane* prostate motion; the registration is invoked when misalignment is detected visually by an operator. The magnetic tracker transform provides an initialization for the 2D US plane within the world coordinate system in their system. In that work, however, registration accuracy was measured with a phantom study. Baumann et al. [5] presented a method relying on the simultaneous real-time acquisition of dual, orthogonal 2D TRUS images acquired from a 3D ultrasound probe. The same authors presented an algorithm [4] to compensate for motion using 3D TRUS volumes acquired continuously throughout the biopsy session. This system does not use any method to track ultrasound probe

motion; therefore, it relies only on the image information for tracking and uses a coarse-to-fine image-based approach to limit the search space during optimization. In addition, this approach requires a special 3D ultrasound probe with enhanced functionality that could simultaneously acquire orthogonal 2D TRUS planes and image acquisition occurs at a lower frame rate, compared to more conventional 2D TRUS. Moreover, compared to 2D TRUS images, orthogonal 2D planes deliver considerably more spatial information; registration of a single 2D TRUS plane to a 3D TRUS image is a more challenging problem.

Previous work [6] has assessed the registration accuracy of several algorithms intended to register two intra-session 3D TRUS images. Although the reported registration errors in [6] are within a clinically acceptable range, using this method within the clinical workflow would require stopping the procedure and acquiring an additional 3D TRUS image each time prostate motion correction is required, leading to questionable feasibility of clinical implementation. Registration of real-time 2D TRUS images to the pre-acquired 3D TRUS image enables motion compensation without adding extra 3D image-acquisition time (approximately a minute using 3D TRUS system in [1]) to the biopsy protocol, and without requiring the use of a 3D TRUS probe. *To the best of our knowledge, no previous work has described and evaluated on human clinical images a method for the registration of 2D TRUS to 3D TRUS images for prostate motion compensation during biopsy.* Such a technique, if properly validated, will make it possible to perform prostate motion compensation on 3D biopsy guidance systems that use readily available 2D ultrasound probes for live image acquisition throughout the

procedure, permitting more widespread use of targeted biopsy systems and thus greater potential impact on the patient population.

2D-3D registration methods have been applied to several other interventional applications in image-guided procedures and Markelj et al. [7] contains an excellent review. Birkfellner et al. [8] compared the performance of several image similarity measures and optimization techniques for 2D-3D registration of fluoroscopic images and found that cross-correlation is an optimal metric for intra-modality matching. In addition, the parallelizability of the computation of the cross-correlation metric in an intra-modal registration could be used improve the speed of execution to become useful in a clinical setting. Wein et al. [9] presented a method to compensate for respiratory motion during abdominal biopsies and ablations under ultrasound guidance, optimizing local normalized cross-correlation using the Powell-Brent direction search technique. Although these previous successes speak to the potential feasibility of addressing the issue of prostate motion compensation in software using a 2D-3D intensity-based image registration technique, prostate appearance on TRUS and motion characteristics during biopsy may differ from those of other organs due to different tissue stiffness properties and flexibility of surrounding anatomical structures. *In this work, our objective is to develop and evaluate a 2D TRUS-3D TRUS intensity-based image registration technique to compensate for prostate motion with sufficient accuracy and speed to be translated to clinical use for 3D biopsy guidance.*

This work describes three primary contributions: (1) We present an intensity-based registration algorithm to register 3D TRUS images acquired at the start of the biopsy procedure to 2D TRUS images acquired during the procedure before the physician

fires the biopsy gun. We evaluated the performance of the registration algorithm both in terms of accuracy and speed, after using a GPU-accelerated implementation. The accuracy of the algorithm was measured using manually identified intrinsic fiducials within the prostate. (2) We performed the registration for 2D TRUS images acquired every second throughout the biopsy procedure in order to evaluate registration accuracy in a scenario when prostate motion is compensated continuously using software, without requiring any human input to trigger the algorithm. This continuous process was executed in parallel with other software providing the user interface and thus the continuous execution of this registration procedure was transparent to the user. At every one-second interval, we incrementally transformed the baseline 3D TRUS image according to the registration obtained during the interval. (3) We further validated the algorithm using a set of 3D TRUS images that were obtained with different levels of controlled probe pressure. 3D TRUS images were sampled to obtain representative 2D TRUS images with different amounts of prostate motion and deformation. This data set contained images with intentionally introduced motion and deformation of magnitudes intended to challenge the algorithm. In addition, the availability of the 3D information yielded more intrinsic fiducials for validation. In this work, we also studied the correlation between image similarity metric values and the amount of misalignment in the prostate.

3.2 Materials and methods

3.2.1 Data acquisition

We acquired images from human clinical biopsy procedures using a mechanically assisted 3D TRUS-guided biopsy system [1] in a study approved by the Human Research Ethics Board of Western University. The system, using a commercially available end-firing 5-9 MHz TRUS transducer probe (Philips Medical Systems, Seattle, WA), acquired a 3D TRUS image at the beginning of the biopsy procedure, and then acquired and displayed 2D TRUS images at a video frame rate (7-30 frames per second) during the biopsy session. The mechanical encoders attached to the ultrasound probe tracked its 3D position and orientation throughout the procedure. Using this system, we recorded images acquired during clinical biopsy procedures under two different protocols, in order to obtain data sets to test the robustness of the registration algorithm under different motion characteristics of the prostate. For both protocols, all 3D TRUS images were recorded prior to taking any biopsy tissue samples. For the first protocol (henceforth referred to as the *biopsy protocol*), we acquired images from eight patients. Following the standard operating procedure for 3D TRUS-guided biopsy in our trial, a 3D TRUS image was acquired at the start of the biopsy procedure. From the sequence of images that followed at video frame rate (10-30 frames per second) during the procedure, we recorded live 2D TRUS images at one frame per second. For the second protocol (henceforth referred to as the *probe pressure protocol*), images were acquired from ten patients. 3D TRUS images were acquired after applying three different probe pressures on the prostate gland centrally: 1) applying a medium probe pressure, similar to what the physician usually applies during a biopsy, 2) applying a low probe pressure that caused

minimal prostate displacement, and 3) applying a high probe pressure that caused substantial prostate deformation and anterior displacement. This yielded a data set with prostate displacements and deformations under a wide range of ultrasound probe pressures.

3.2.2 2D-3D registration – biopsy protocol

For each of the eight subjects, we selected 1–3 2D TRUS images per patient 1–2 seconds prior to biopsy needle insertion from the 10–12 biopsy samples taken during the biopsy. This choice of 2D TRUS images was motivated by the fact that accurate alignment of the predefined targets with the intra-procedure anatomy is chiefly required immediately prior to biopsy, when a tissue sample is to be taken from an intended biopsy target. We analyzed 16 such images from eight patients.

The transformation, $T_{Tr} : \Psi \rightarrow \Omega$, given by encoders on the joints of the linkage of the mechanical assisted 3D-TRUS biopsy system [1], maps each live 2D TRUS image, $I_{live} : \Psi \rightarrow \mathbb{R}$, to the world coordinate system of the previously acquired 3D TRUS image $I_{base} : \Omega \rightarrow \mathbb{R}$, where $\Psi \subset \mathbb{R}^2$ and $\Omega \subset \mathbb{R}^3$. Within the 3D world coordinate system, any differences in prostate position and orientation between the real-time 2D TRUS images and the initially-acquired 3D TRUS image are due to prostate motion within the patient, gross movements of the patient during the procedure, and the biopsy system’s tracking errors. The accuracy of the initialization for the prostate motion registration algorithm is based in part on tracking errors of the biopsy system. In the system developed by Bax et al. [1], the accuracy in delivering a needle to a biopsy core in a phantom were found to be 1.51 ± 0.92 mm. Registration of live 2D TRUS images to

the pre-acquired 3D image compensates for both the tracking errors and errors due to prostate and patient motion.

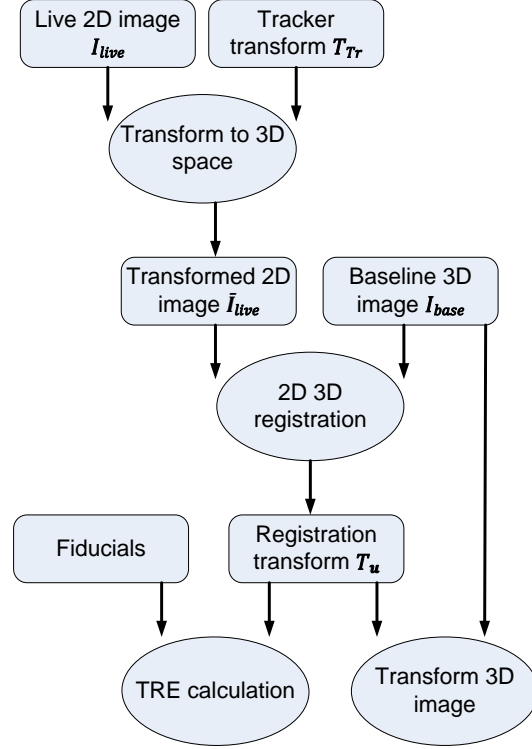


Figure 3.1:2D-3D registration workflow

The overall workflow in our method is depicted in Figure 3.1. Using the mechanical tracker transform (T_{Tr}) we transform I_{live} to the 3D world coordinate system. Registration is then performed to I_{base} within this coordinate system. To reduce the effects of speckle, anisotropic diffusion filtering [10] (conductance parameter = 2, time step = 0.625) of images was used as a pre-processing step. Although there can be non-rigid deformation of the prostate due to ultrasound probe pressure [6], a rigid alignment can be found with lower computational cost, so we investigated the accuracy of rigid registration in this work to determine whether rigid registration is sufficient for the clinical purpose of biopsy targeting. For each 2D TRUS image, finding the corresponding plane in the pre-acquired 3D TRUS volume is a 2D-to-3D intra-modality

rigid registration problem. Due to limited ultrasound contrast within the prostate, reliable extraction of the boundary and other anatomic features is challenging. Therefore, we tested an intensity-based registration algorithm.

Using the mechanical tracker transform T_{Tr} , we can position and orient the 2D TRUS image I_{live} within the 3D world coordinate system yielding a 3D image \tilde{I}_{live} as $\tilde{I}_{live}(T_{Tr}(p_1)) = I_{live}(p_1)$ where $p_1 \in \Psi$.

The registration of the baseline 3D image I_{base} to \tilde{I}_{live} is performed in this 3D world coordinate system considering I_{base} as the source image and \tilde{I}_{live} as the target image. The objective of the registration is to find the transformation, $T_u: \Omega \rightarrow \Omega$, consisting of a six-parameter-vector given by \mathbf{u} , that aligns anatomically homologous points in I_{base} and \tilde{I}_{live} . We used normalized cross-correlation (NCC) [11] as the image similarity metric that was optimized during the registration. For two images \tilde{I}_1 and I_2 , we optimized the objective function defined as:

$$F = \underset{\mathbf{u}}{\operatorname{argmax}} NCC(\tilde{I}_1, I_2; \mathbf{u}), \text{ where}$$

$$NCC(\tilde{I}_1, I_2; \mathbf{u}) = \frac{\sum_{p \in \Omega_{1,2}^{T_u}} (\tilde{I}_1(p) - \bar{\tilde{I}}_1)(I_2(T_u(p)) - \bar{I}_2)}{\left\{ \left(\sum_{p \in \Omega_{1,2}^{T_u}} (\tilde{I}_1(p) - \bar{\tilde{I}}_1)^2 \right) \left(\sum_{p \in \Omega_{1,2}^{T_u}} (I_2(T_u(p)) - \bar{I}_2)^2 \right) \right\}^{\frac{1}{2}}} \quad (3.1)$$

and Ω_1 and Ω_2 represent the subspaces of $(\Omega \subset \mathbb{R}^3)$ containing the image domains of I_1 and I_2 , i.e., $\Omega_{1,2}^{T_u} = \{p \in \Omega_1 | T_u^{-1}(p) \in \Omega_2\}$.

We optimized the image similarity measure given by $NCC(I_{live}, I_{base})$ to obtain T_u for each of the 16 images we acquired. We used Powell's method [12, 13] to optimize the six-dimensional search space that includes three translations and three rotations.

Powell’s method improved the speed of execution, when compared with a gradient-descent-based method during our initial experiments.

3.2.3 Incremental 2D-3D registration for continuous intra-biopsy motion compensation

The registration to compensate for prostate motion can be performed frequently (e.g., once per second) throughout the biopsy procedure, with the frequency of registration limited by the time required to register a single pair of images. At a given time point denoted by t_n (time elapsed in seconds from the start of the biopsy), we initialized the source image for the n^{th} registration with the transformation matrix obtained from registrations at previous time points using

$$T_{\mathbf{u}} = \prod_{t=t_0}^{t_n} T_{\mathbf{u}_t}, \quad (3.2)$$

During the n^{th} registration, we found the parameter vector \mathbf{u}_{t_n} that gave the optimum *NCC* measure for the transformation matrix $T_{\mathbf{u}_{t_n}}$. We performed the registration for the complete biopsy procedure for the eight patients described in the previous section using the sequence of live 2D TRUS images recorded every second from the start of the biopsy procedure.

3.2.4 2D-3D registration – probe pressure protocol

3D TRUS images acquired at different probe pressures can provide additional anatomical context to enhance the validation of our registration algorithm. We denote images acquired at low, medium and high probe pressures, respectively, as $I_{low}, I_{med}, I_{high}: \Omega \rightarrow \mathbb{R}$. We acquired 30 such images from 10 patients.

We set the image acquired at medium pressure, I_{med} , as the source image. As our target image, we selected 2D slices ($\tilde{I}_{\{low,high\}}$) from the 3D images I_{low} and I_{high} . For the 20 registrations performed (using the 30 3D TRUS images) mechanical tracker transformations (T_{Tr}) were randomly selected from 16 frames (across 8 subjects in the biopsy protocol) occurring an average of 1-2 seconds prior to the firing of the biopsy gun in real biopsy procedures, according to $\tilde{I}_{\{low,high\}}(p_2) = I_{\{low,high\}}(T_{Tr}(p_1))$ where $p_1 \subset \Psi$ and $p_2 \subset \Omega$.

Hence, the target images are representative of live 2D TRUS images depicting a situation with minimal prostate motion (slice from I_{low}) and substantial prostate motion (slice from I_{high}). Since the physician intentionally applies different levels of pressure during the acquisition, the set of images contains a wide range of prostate displacements and deformations that are intended to represent the extremes of probe pressure during the biopsy procedure to challenge the registration algorithm. For each subject, we perform registration between images $I_{med}-I_{low}$ and $I_{med}-I_{high}$ by respectively optimizing the image similarity measures, $NCC(\tilde{I}_{low}, I_{med})$ and $NCC(\tilde{I}_{high}, I_{med})$ as defined above in Equation 3.1.

3.2.5 Validation

3.2.5.1 Biopsy protocol registration

The registration was validated using manually-identified corresponding intrinsic fiducial pairs (micro-calcifications) [6]. For the images acquired under the biopsy protocol, fiducials appearing in I_{base} , denoted by f_{base} , and the corresponding fiducials from I_{live} , denoted by f_{live} , were identified ($f_{live} \subset \Psi$ and $f_{base} \subset \Omega$). We identified 52 fiducial

pairs for 16 biopsies in eight patients. These fiducial pairs were used for validation only and were not provided as input to the registration algorithm. Fiducial localization error (FLE) has been reported in previous studies in the context of 3D TRUS and 2D TRUS images. The FLE in 3D TRUS images was reported to be 0.21 mm [6] and in 2D TRUS images was 0.11 [14] mm. The target registration error was calculated as the root mean square (RMS) error

$$TRE_b = \sqrt{\frac{\sum_{k=1}^{N_k} (T_{Tr}^{-1}(f_{live}^k) - T_u^b(f_{base}^k))^2}{N_k}}, \quad (3.3)$$

$$TRE_{biopsy} = \sqrt{\frac{\sum_{b=1}^{N_b} TRE_b^2}{N_b}}, \quad (3.4)$$

where N_b is the number of biopsies and N_k is the number of fiducials identified for a particular pair of images. The TRE was estimated by first calculating RMS values TRE_b using the fiducials identified in each pair of images for each biopsy and then calculating the RMS value TRE_{biopsy} for the number of biopsies performed. This approach averaged the contributions to the TRE from the variable number of fiducials manually identified in each pair of images during a biopsy. The pre-registration error was calculated without applying the registration transform T_u in Equation 3.3 to compare against TRE post registration to assess the improvement.

We selected images that contained visible micro-calcifications within the prostate in calculating TRE_{biopsy} ; an ideal registration algorithm would bring these homologous landmarks into alignment after registration. Although the fiducials are small (less than ~1 mm radius) by comparison to the size of the prostate and field of view (Figure 3.2 depicts some sample fiducials that we identified), in principle it is possible that the

presence of the calcifications could guide an intensity-based registration algorithm to a result giving a lower TRE_{biopsy} than would be obtained if the fiducials were not present in the images. In order to test if the presence of micro-calcifications drive the registration algorithm to a more accurate solution, we defined masks over the identified fiducials in both the target and source images and performed the registrations described in the biopsy protocol registration, restricting the calculation of the image similarity metric to regions outside of the masks; i.e., to regions not containing the fiducials. Thus, in this experiment, the registration algorithm was blinded to the presence and locations of the fiducials. The masks were defined as spherical regions with 1 mm radius in order to fully cover the largest fiducial markers we observed in our data set.

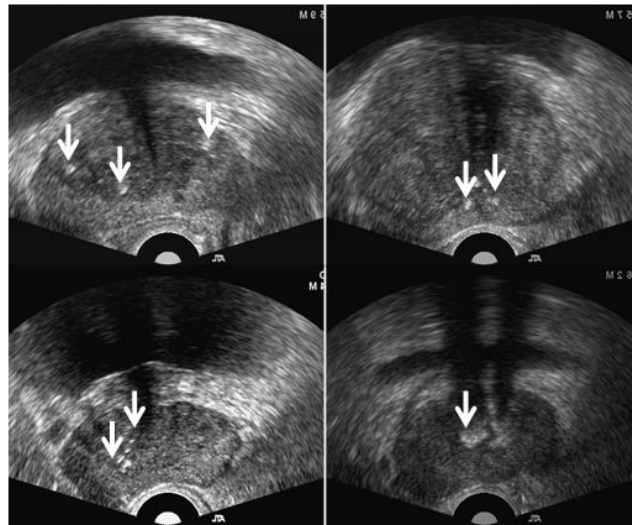


Figure 3.2: Sample fiducials identified.

3.2.5.2 Probe pressure protocol registration

In the data set acquired under the probe pressure protocol, full 3D anatomical information for the whole prostate was available for both the source and target images. We manually identified 188 fiducials throughout the 3D volumes obtained from 10 subjects, without

limiting the fiducials to lie within the particular extracted plane used in the registration.

The TRE was computed as

$$TRE_p = \sqrt{\frac{\sum_{k=1}^{N_k} (T_{3D-world}(f_{med}^k) - T_u^b(f_{\{low,high\}}^k))^2}{N_k}}, \quad (3.5)$$

$$TRE_{pressure} = \sqrt{\frac{\sum_{b=1}^{N_p} TRE_p^2}{N_p}}, \quad (3.6)$$

where $f_{\{med,low,high\}} \subset \Omega$ are the fiducials identified in $I_{med}, I_{low}, I_{high}$.

We also computed the optimal rigid alignment using the identified fiducials to define the rigid transformation that yielded the minimum TRE for the given fiducials per patient. To do this, we found the fiducial registration error (FRE) [15] for each set of fiducial pairs in each patient, after transforming the fiducials with the parameters corresponding to the best rigid alignment. With the presence of non-rigid deformations in the probe pressure protocol data set, the FRE gives a lower bound on the $TRE_{pressure}$ that can be obtained using a rigid registration. In a sense, the FRE gives an indication of the amount of non-rigid deformation present in the data set; e.g., an FRE of 0 mm would indicate that a rigid transformation could fully compensate for the observed changes in the prostate, and an FRE > 0 mm would indicate that some amount of non-rigid deformation may have occurred in the prostate. Thus the FRE gives some indication of a “best-case” TRE that could be obtained from a registration algorithm using a rigid transformation and it is therefore of interest to compare the FRE to the $TRE_{pressure}$ obtained from our registration algorithm.

We used the fiducials throughout the prostate to calculate the TRE. To test whether the TRE varies with distance to the registration plane, we plotted TRE against the distance to the registration plane for each fiducial.

3.2.6 GPU implementation

The step consuming the most computation time during execution of the registration was the calculation of the image similarity metric during optimization. Therefore, we implemented the *NCC* calculation on an nVidia GTX 690 (Nvidia Corporation, Santa Clara, CA) graphics processing unit (GPU) using compute unified device architecture (CUDA) C++. The normalized cross-correlation calculation is inherently parallelizable. Instead of using a sequential approach to transform each voxel independently, we transformed all voxels in the moving image in parallel during each iteration of optimization. These transformations were followed by 3D linear interpolation of image intensities to resample the moving image that was also performed within the GPU. The subsequent calculation of the summations in Equation 3.1 was also done in parallel to further accelerate the execution.

3.2.7 Correlation between image similarity metric and misalignment

During registration, we optimize an image similarity metric over a 3D transformation space. The relationship between the image similarity metric and the amount of misalignment not only conveys the suitability of the metric to be used in registration, but also it shows whether the image-similarity metric could be used as an indicator of the misalignment. This could be a useful feature to trigger the registration algorithm in a system that does not continuously compensate for motion as during biopsy. To analyze

this relationship using the biopsy protocol data, we plotted the calculated normalized cross-correlation measures for each instance before registration, during registration (for each iteration during the optimization) and after registration (after the optimizer converged) and their corresponding TRE_{biopsy} values.

With manually identified fiducials, we should be able to find a plane within the 3D TRUS image that yields zero (or near zero) TRE. We analyzed the behaviour of normalized cross-correlation near this “optimum” plane by extracting 2D images lying nearby (in terms of the six parameters, \mathbf{u} , defining 3D translation and rotation) planes in the 3D TRUS image, and computed the image similarity metric for the 2D TRUS image and these nearby 2D images from the 3D TRUS image. Although this approach does not fully explore the six-dimensional objective function, to simplify the visualization of the results, we analyzed the metrics by varying one degree-of-freedom at a time.

3.2.8 TRE as a function of distance to the probe tip

We analyzed the TRE as a function of distance of each fiducial to the ultrasound probe tip, to test if the registration error is larger within the regions of the prostate close to the ultrasound probe. Since we used a rigid transformation during registration, non-rigid deformation of the prostate would be reflected as part of the TRE. Ultrasound probe pressure might cause inconsistent deformation in different regions of the prostate, which could lead to regionally-varying accuracy of motion compensation by a rigid transformation.

3.3 Results

3.3.1 Validation: biopsy protocol data

The TRE_{biopsy} was calculated according to Equation 3.4 and its $RMS \pm std.$ was found to be 1.87 ± 0.81 mm, after manually localising 52 fiducial pairs over 8 patients. This was an improvement over 4.75 ± 2.62 mm before registration. Since these TRE distributions were found to be not normally distributed using one-sample Kolmogorov-Smirnov test with a significance level $p < 0.0001$, we tested the null hypothesis that their medians were equal with a non-parametric test using Prism 5.04 (Graphpad Software Inc., San Diego, USA). The Wilcoxon signed rank matched pairs test rejected the null hypothesis ($p < 0.0001$) suggesting that there is a statistically significant difference in TREs before and after registration. When the registrations were performed with the fiducials masked out, the TRE was found to be 1.93 ± 0.66 mm. When compared with the distribution of TRE_{biopsy} , the Wilcoxon signed rank matched pairs test failed to reject the null hypothesis ($p = 0.74$). Thus, we were unable to detect a statistically significant difference between the TREs resulting from registrations where the fiducials were present and registrations where the fiducials were absent.

When 2D-3D registration was performed incrementally every second during the biopsy, the $RMS \pm std$ TRE was reduced to 1.63 ± 0.51 mm. The mean number of iterations required for convergence decreased from 5.6 to 2.75. Figure 3.3 shows changes in TRE values before registration, after registration and after registering the frame obtained every second for each biopsy taken. Figure 3.4 contains two representative example images, depicting the visual alignment qualitatively for registration just prior to biopsy. The post-registration TRE of these two example images

were found to be 1.5 mm (top row) and 1.2 mm (bottom row), which had improvements from 3.7 mm (top row) and 5.3 mm (bottom row) before registration. Grid lines overlaid at corresponding locations in image space facilitate visual evaluation of the alignment of the anatomy pre- and post-registration.

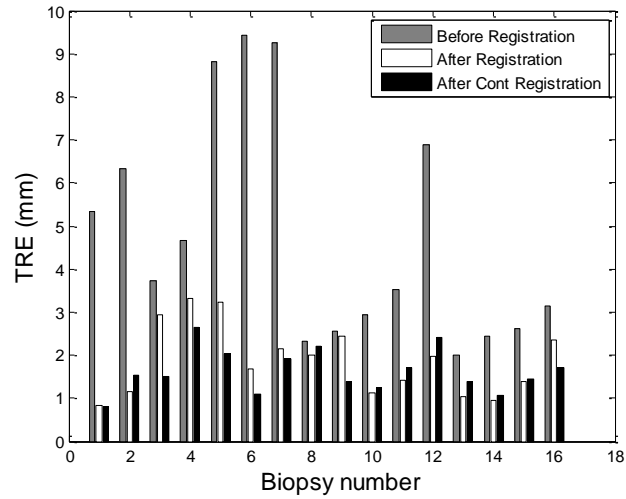


Figure 3.3: TRE before registration, after registration and after continuous registration every second for each biopsy in prostate biopsy protocol.

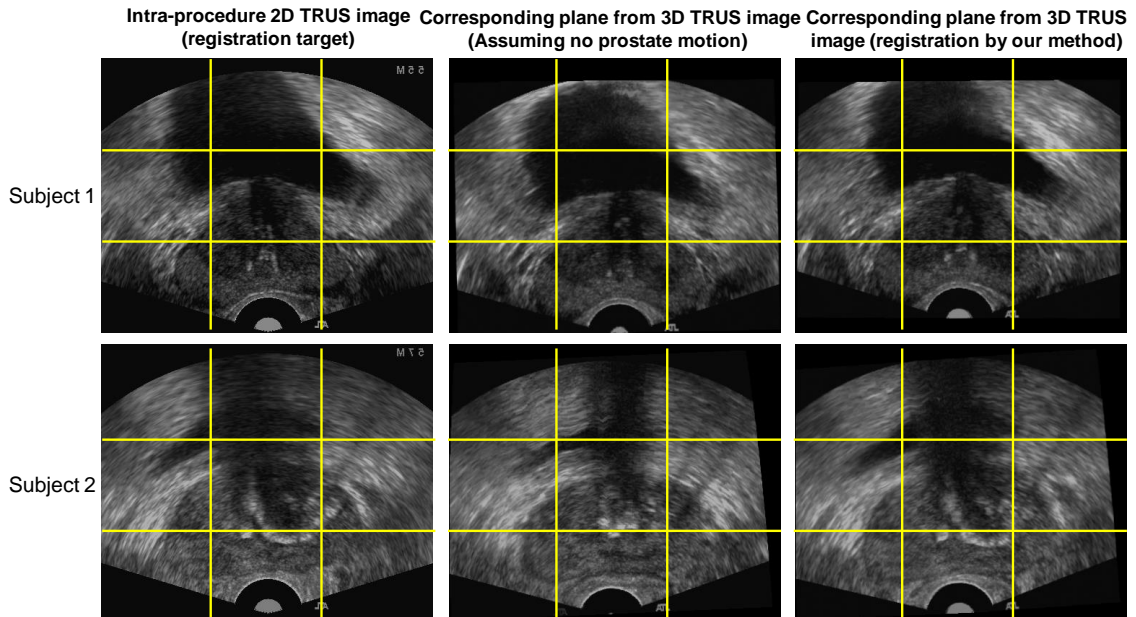


Figure 3.4: Images before and after registration immediately prior to taking a biopsy sample. Left column: Real-time 2D TRUS images. Middle column: Corresponding images before registration assuming no prostate motion (from the transformation given by the mechanical tracking system). Right column: Corresponding images after registration.

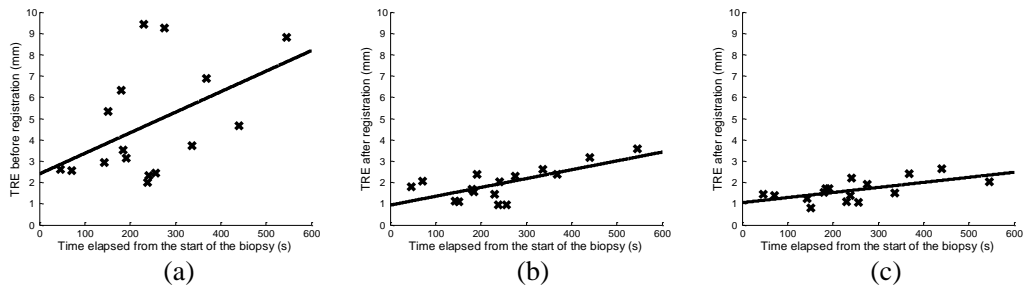


Figure 3.5: TRE as a function of time elapsed from the start of the biopsy. (a) TRE before registration. (b) TRE after registration. (c) TRE after registering the images acquired every second.

In order to see the effect of patient motion over time during the biopsy session, we analyzed the TREs obtained from eight patients as a function of time elapsed since the start of the biopsy. According to the results shown in Figure 3.5, it can be seen that the TRE values before and after registration have an increasing trend with the elapsed time during the biopsy. Weak relationships were found with slopes of the best-fit line $10 \mu\text{m/s}$ (correlation coefficient (r^2) = 0.23) before registration and $4 \mu\text{m/s}$ (r^2 = 0.41) after registration. When the registration was performed every second, the slope of best-fit line

was found to be $2 \mu\text{m/s}$ ($r^2 = 0.37$). We also calculated the slopes of the best-fit lines to plots of TRE versus time elapsed during biopsy for each individual patient, and then calculated the mean and standard deviation of these observed slopes in scenarios with and without the use of motion-compensating registration. Without registration, we observed a mean \pm std slope of $14\pm 15 \mu\text{m/s}$. With registration, we observed a mean \pm std slope of $7\pm 10 \mu\text{m/s}$, and $5\pm 14 \mu\text{m/s}$ with continuous registration.

3.3.2 Validation: probe pressure protocol data

The RMS TRE for the data acquired under the probe pressure protocol was 3.18 ± 1.6 mm. This was an improvement from a 6.89 ± 4.1 mm TRE before registration. Note that we used the fiducials in the whole prostate (not just the slice containing the fiducials) in TRE calculation as given in Equation 3.6. The mean value for the FRE, corresponding to the best rigid transform that aligns the identified fiducials, was found to be 1.85 ± 1.2 mm. The distribution of TRE values before registration, after registration, and after transforming with the best rigid alignment is shown in Figure 3.6. Table 3.1 contains TRE calculated separately for I_{med} -to- I_{high} and I_{med} -to- I_{low} . Registration between I_{med} and I_{high} has resulted in a larger TRE. We also observed higher FRE in I_{med} -to- I_{high} , suggesting a greater amount of non-rigid deformation of the prostate at this extremum of probe pressure. The error in registration includes the errors due to non-rigid deformation occurring within prostate regions outside of the 2D target image (as opposed to the errors arising only due to deformation within the 2D target image as in the biopsy protocol) and the variability in manually locating the fiducials in 3D. However, according to the relationship between distance from registration plane to each fiducial and the TRE shown

in Figure 3.7, we did not observe a strong relationship between the TRE and the distance from registration plane to the fiducial.

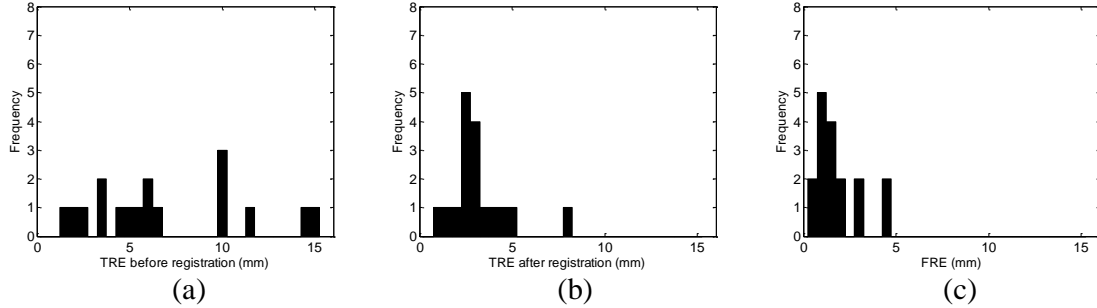


Figure 3.6: Histograms for TRE before and after registration for probe pressure protocol data. Left: TRE distribution before registration Middle: TRE distribution after registration. Right: TRE distribution with the best rigid alignment for the identified fiducials.

Table 3.1: Errors before and after probe protocol registration.

	Error before registration (mm)	TRE after registration (mm)	FRE (mm)
$I_{med-to-I_{high}}$	7.57 ± 4.58	3.65 ± 2.12	2.12 ± 1.45
$I_{med-to-I_{low}}$	6.12 ± 3.68	2.65 ± 0.34	1.54 ± 0.68
Average	6.89 ± 4.12	3.17 ± 1.60	1.85 ± 1.67

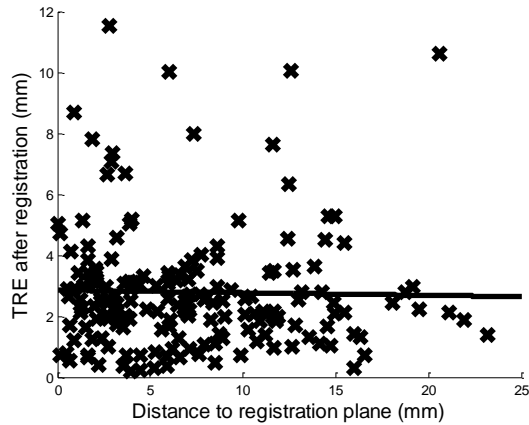


Figure 3.7: TRE of each fiducial as a function of distance to the registration plane. The black line represents the least-square fit to the scattered points.

3.3.3 Speed of execution

After the GPU-accelerated implementation (nVidia GTX 690 GPU card and Intel Core i7-3820 3.6 GHz processor) the registration was performed with mean \pm std times of 1.1 ± 0.1 seconds for the biopsy protocol experiments described in this paper.

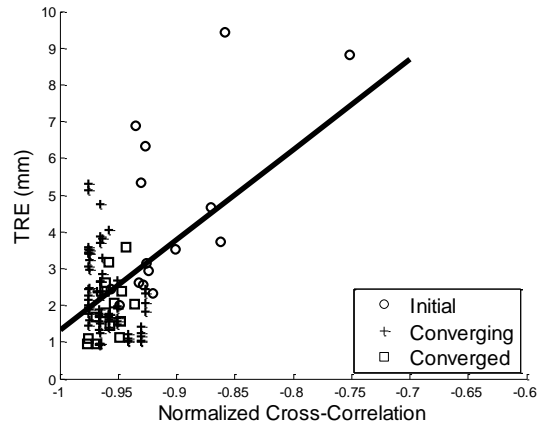


Figure 3.8: TRE as a function of metric value during the optimization. Initial points (circles), converged (squares) and converging points (crosses).

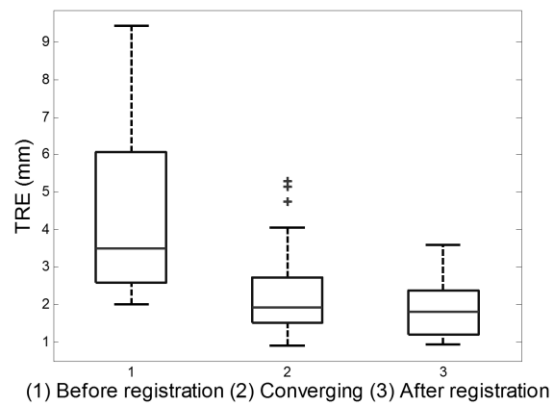


Figure 3.9: TRE distributions before registration, during convergence and after registration.

3.3.4 Correlation between image similarity measure and misalignment

Figure 3.8 shows the relationship between the image-similarity measure and values of TRE for each transformation obtained during the optimization iterations. The circle

points show the values before registration, and the square points show the values after registration converged. The cross points depict the values during convergence. The correlation coefficient (r^2), calculated using all points (before, during, and after convergence) in Figure 3.8, was found to be 0.23. Figure 3.9 shows a box plot of the TRE distributions of the points before registration, during convergence and after registration. While the TRE decreases in general during convergence, a weak correlation can be seen between image similarity measures and TRE from these results.

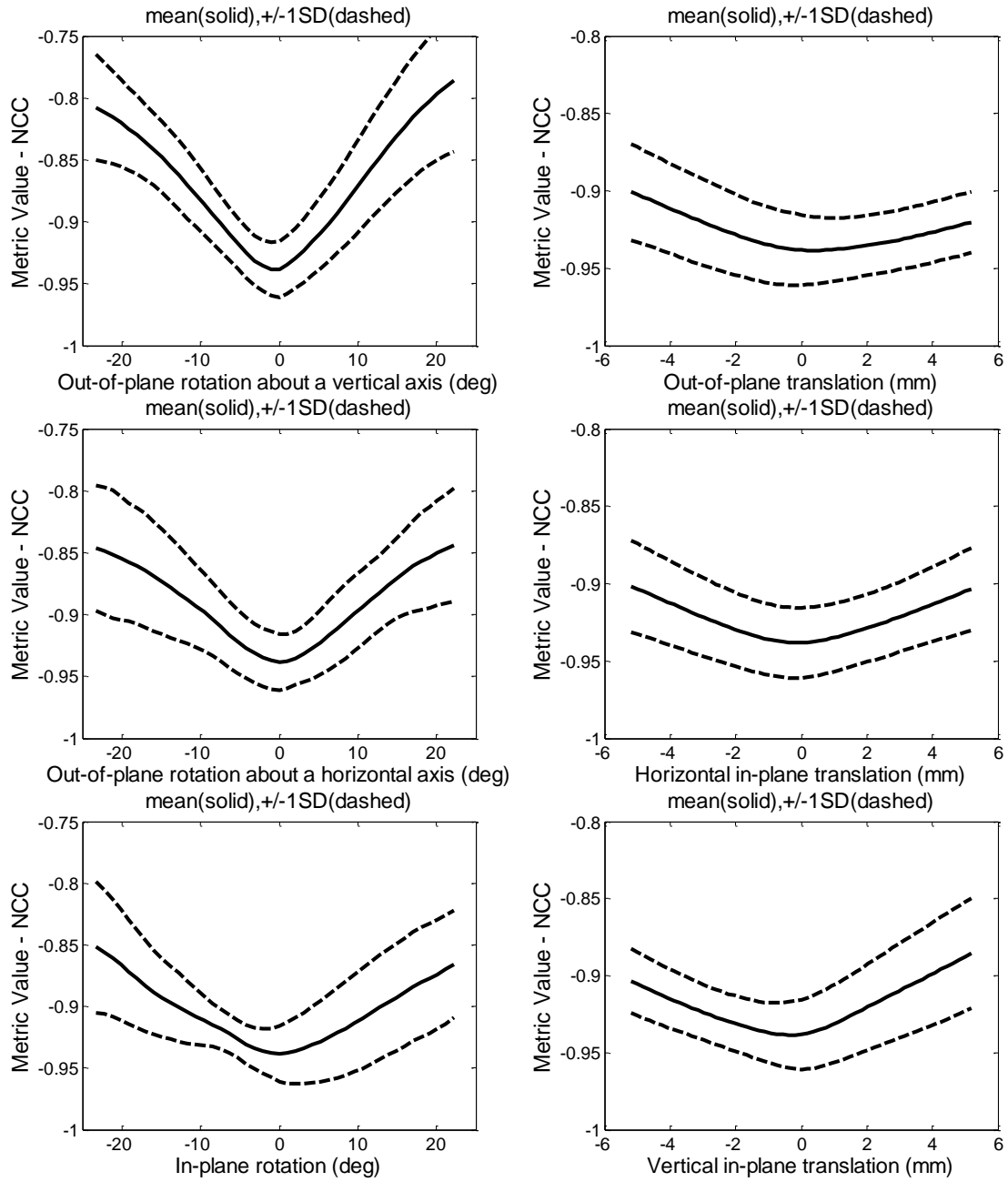


Figure 3.10: Mean and standard deviations of normalized cross-correlation values for 16 image pairs of eight patients in the six-degrees-of-freedom transformation space, one degree-of-freedom varying at a time. The zero location in the x-axis corresponds to real-time 2D-TRUS frame.

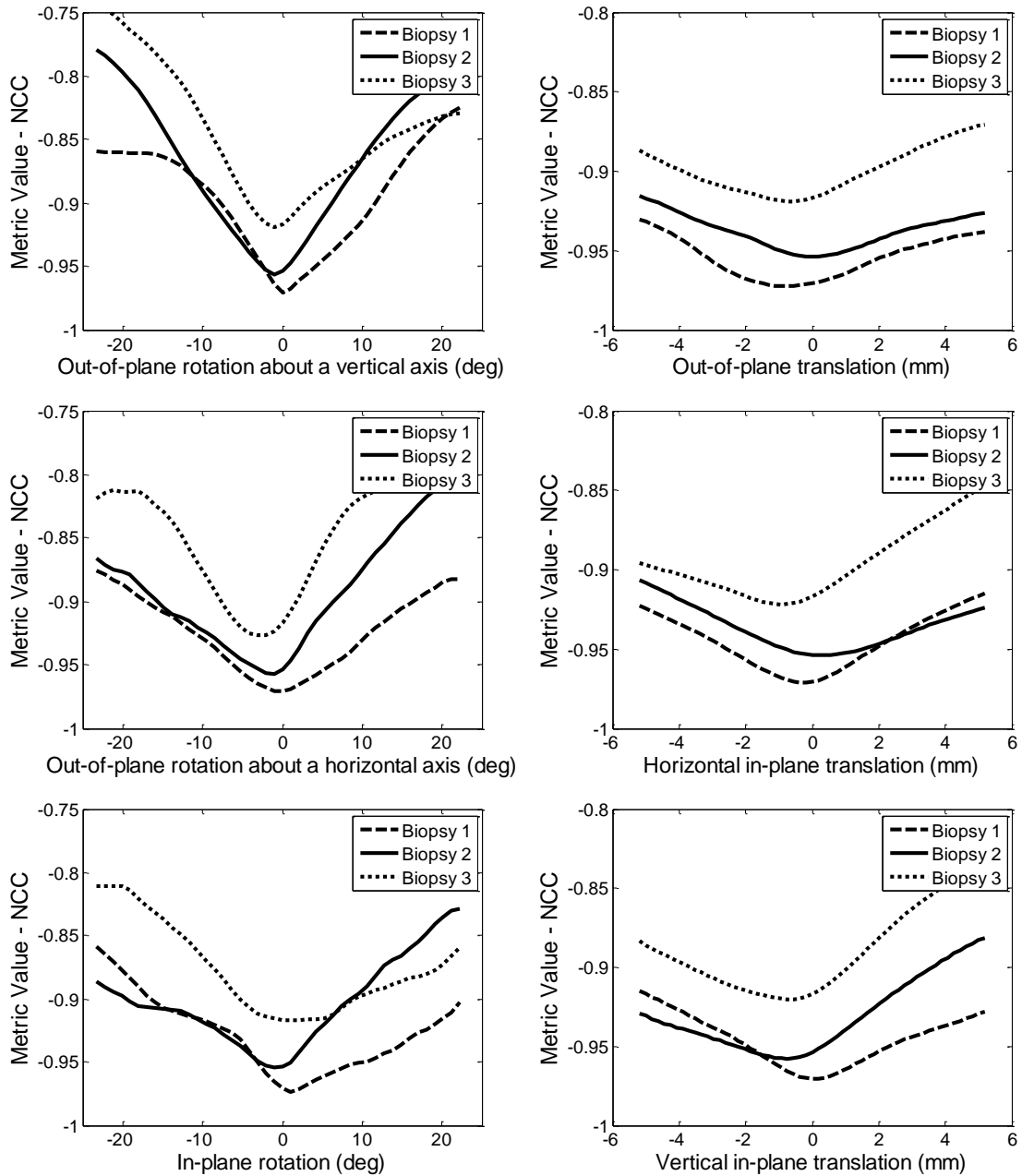


Figure 3.11: Normalized cross-correlation values for a single image pair of a biopsy for 3 patients (each biopsy represented by a separate line pattern) in the six-degrees-of-freedom transformation space, one degree-of-freedom varying at a time. The zero location in the x-axis corresponds to real-time 2D-TRUS frame.

Figure 3.10 shows plots of the normalized cross-correlation metric versus out-of-plane, in-plane rotations and translations. The solid curves represent the mean values of the metrics for different out-of-plane rotations and translations for 16 2D TRUS images

across eight subjects, and the dashed curves show the values one standard deviation above and below the mean. The convexity of the mean curves gives an indication of the general capture range of the objective functions for many registrations. Figure 3.11 shows the three plots of normalized-cross-correlation metrics similarly obtained for a single biopsy in three patients. The generally convex shape of the functions observed in Figure 3.10 and Figure 3.11 encourages the use of normalized cross-correlation during registration in compensating for prostate motion.

3.3.5 TRE as a function of distance to the probe tip

Figure 3.12 shows TRE as a function of the distance to the probe tip for each individual. The TRE tends to increase closer to the probe tip (r^2 value = 0.1); however, the correlation between distance to the probe tip and the TRE before registration is weak.

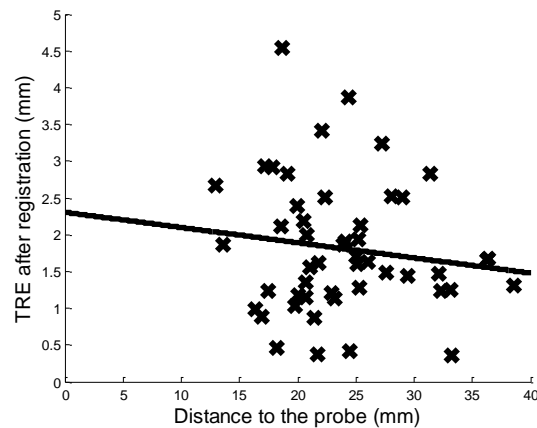


Figure 3.12: TRE as a function of distance to the probe tip.

3.4 Discussion

3.4.1 Accuracy of registration

Our image registration method was validated using the fiducials identified in clinical images acquired during the biopsy procedures. There was a significant improvement of

TRE after registration in both biopsy and probe pressure protocols. The required accuracy of the biopsy system to guide needles to target locations stems from the size of the smallest clinically-relevant tumours (0.5 cm^3 , corresponding to a spherical target with 5 mm radius) [16, 17]. A biopsy system with a measured RMS error of 2.5 mm in taking a sample from the intended target will have a probability of at least 95.4% of taking a sample within this 5 mm radius since 5 mm is 2 standard deviations away from the mean of the distribution of targets given by an system with RMS error of 2.5 mm [6]. An image-based registration during the procedure, while compensating for prostate motion, also corrects for tracking errors in the biopsy system, if any. Therefore, if the registration was performed immediately before the physician fires the biopsy gun to capture a tissue sample from the prostate, the targets identified in the pre-acquired 3D image would be aligned with the live 2D TRUS image, with accuracy limited by the TRE of the registration algorithm. However, the motion and deformation induced due to the rapid firing of the biopsy gun, which happens during a sub-second interval remains an error in the biopsy system that is challenging to correct. When targeting a predefined location, the TRE of the motion compensation algorithm and the error during the rapid biopsy-gun firing process, which was quantified in [14] to be an error with 95% confidence interval less than 2.1 mm, may accumulate and become an important consideration.

Alignment of the targets identified in the 3D TRUS image to the live 2D TRUS image is primarily required immediately before the physician fires the biopsy gun. Consequently, this registration could be integrated into the clinical workflow by executing it just prior to the physician aiming at target locations. However, according to the results, both the accuracy and speed of the registration were improved when the

registration was performed on the 2D TRUS images acquired every second.

Initializations obtained by placing 2D TRUS images within the 3D coordinate system using the mechanical tracker transform (T_{Tr}) might further improve when the baseline 3D TRUS image is updated more frequently with the transforms from registrations performed every second. This may help the algorithm in faster convergence to a suitably accurate optimum. Therefore, in a clinical procedure, this algorithm can be performed in the background continuously compensating for motion.

3.4.2 Change of TRE with time during biopsy

The weak positive relationship between TRE and time elapsed shown in Figure 3.5(a), suggest that the misalignment between pre-acquired and live images increases with time (slope of the best-fit line = $10 \mu\text{m/s}$, $\text{mean}\pm\text{std} = 14\pm 15 \mu\text{m/s}$ for individual patients).

After performing the registration just before a biopsy sample is taken, there is still a positive relationship (slope = $4 \mu\text{m/s}$, $\text{mean}\pm\text{std} = 7\pm 10 \mu\text{m/s}$) between TRE and time.

This indicates that image pairs, with higher initial misalignments towards the end of the biopsy procedure, were more challenging for the algorithm. In Figure 3.5(c), the slope of the best-fit line was lower (slope = $2 \mu\text{m/s}$, $\text{mean}\pm\text{std} = 5\pm 14 \mu\text{m/s}$) when the registrations were performed every second. Thus, although the TRE does appear to increase with time even when registration is applied, this effect is less pronounced compared to the no-registration scenario. The increasing trend in TRE with time that we observe for eight patients in Figure 3.5(c) even when the motion was being compensated every second could be due to accumulation of registration errors during continuous registration. In addition, the swelling and deformation of the prostate caused by the

increasing number of needles being inserted might increase the challenge to the algorithm as a function of time elapsed since the start of the biopsy.

3.4.3 Probe pressure protocol

The TREs from the probe pressure protocol are surrogate measures of the absolute total registration error that could be observed under extreme prostate deformations during prostate biopsy. In probe pressure protocol, the TRE was 1.2 mm higher than that of the biopsy protocol. This increase could be attributed to the use of fiducials from the whole prostate during validation. The best rigid transform for the selected plane may not necessarily be the best rigid fit for the whole prostate due to non-rigid deformations occurring at different (out of plane) regions of the prostate. Moreover, the high probe pressures intentionally exerted by the physician when acquiring these images might have caused more than the usual deformation that occurs during biopsy. The extreme range of probe pressures and prostate displacement and deformation could make accurate registration more challenging as the algorithm is more susceptible to local optima the further the initialization is from target alignment. In addition, substantial non-rigid deformation may result in higher TREs from rigid registration algorithms when high probe pressure is applied to the prostate. Whereas the prostate deformations occurring during the biopsy protocol arise from real clinical biopsy sessions, the probe pressure protocol was explicitly designed to test the performance of the algorithm at the extrema of non-rigid deformations that can be reasonably applied to the patient's prostate in vivo, without consideration of the plausibility of such deformations occurring in a clinical biopsy context. The outliers observed in Figure 3.6(c) suggest that a non-rigid transformation may be useful in correcting for the more extreme deformations applied

during the probe pressure protocol. This is illustrated quantitatively in the FRE column of the first row of Table 3.1, where registration errors involving high probe pressure were separately analyzed. However, the fiducial identification process was relatively more straightforward due to the availability of 3D contextual information in both the fixed and moving images.

3.4.4 Correlation between similarity metric and TRE

Figure 3.8 shows a weak correlation between similarity metric values before, during and after convergence and the TRE. We can observe for the cases where the metric values were greater than -0.9, the TREs were greater than 3.5 mm. Furthermore, the generally convex shapes observed in Figure 3.10 and Figure 3.11 in metric values as a function of different amounts of introduced translations and rotations, suggest that the metric value could be used as a weak indicator to the quality of the registration.

In Figure 3.12, a weak negative correlation can be seen between the TRE and distance to the probe tip. This suggests that near the probe tip there could be higher non-rigid deformation of the prostate that may not be accurately compensated with a rigid registration algorithm. However, given the limited sample size and the weak relationship observed, further verification is required to attribute the negative correlation to the presence of non-rigid deformation.

3.5 Conclusions

Accurate and quick registration to compensate for motion during biopsy is an important step to improve the accuracy in delivering needle to target locations within the prostate. We presented a 2D-to-3D rigid intensity-based registration algorithm validated on human

clinical images using intrinsic fiducial markers, to align a 3D TRUS image (with associated prostate biopsy targets) acquired at the start of the procedure to 2D TRUS images taken immediately prior to each biopsy during the procedure. We also presented evidence that image similarity metrics can be used as a weak indicator of the amount of prostate misalignment (with respect to the initially acquired 3D TRUS image), and could be used to trigger the execution of a registration algorithm when necessary. Using our high-speed GPU implementation (1.1 seconds total time per registration), this algorithm has the potential to be useful during the clinical workflow of a biopsy procedure. Although 2D-3D registration methods described in this paper yielded statistically significant improvements in accuracy, the RMS TRE was found to be 3.18 ± 1.6 mm with the 3D TRUS data set acquired under a more controlled range of probe pressures intending to thoroughly test the algorithm. Therefore, achieving a more accurate and robust registration for motion compensation could be helpful to meet the clinical requirements of accurately targeting smallest clinically significant tumors using 3D TRUS-guided biopsy systems.

References

1. J. Bax, D. Cool, L. Gardi, K. Knight, D. Smith, J. Montreuil, S. Sherebrin, C. Romagnoli and A. Fenster, "Mechanically assisted 3D ultrasound guided prostate biopsy system," *Med Phys* **35**, 5397-5410 (2008).
2. S. Xu, J. Kruecker, B. Turkbey, N. Glossop, A. K. Singh, P. Choyke, P. Pinto and B. J. Wood, "Real-time MRI-TRUS fusion for guidance of targeted prostate biopsies," *Comput Aided Surg* **13**, 255-264 (2008).
3. D. Cool, S. Sherebrin, J. Izawa, J. Chin and A. Fenster, "Design and evaluation of a 3D transrectal ultrasound prostate biopsy system," *Med Phys* **35**, 4695-4707 (2008).
4. M. Baumann, P. Mozer, V. Daanen and J. Troccaz, "Prostate biopsy tracking with deformation estimation," *Med Image Anal* **16**, 562-576 (2013).
5. M. Baumann, P. Mozer, V. Daanen and J. Troccaz, "Prostate biopsy assistance system with gland deformation estimation for enhanced precision," *Med Image Comput Comput Assist Interv* **12**, 67-74 (2009).
6. V. V. Karnik, A. Fenster, J. Bax, D. W. Cool, L. Gardi, I. Gyacskov, C. Romagnoli and A. D. Ward, "Assessment of image registration accuracy in three-dimensional transrectal ultrasound guided prostate biopsy," *Med Phys* **37**, 802-813 (2010).
7. P. Markelj, D. Tomazvic, B. Likar and F. Pernus, "A review of 3D/2D registration methods for image-guided interventions," *Medical Image Analysis* **16**, 642-661 (2012).
8. W. Birkfellner, M. Figl, J. Kettenbach, J. Hummel, P. Homolka, R. Scherthaner, T. Nau and H. Bergmann, "Rigid 2D/3D slice-to-volume registration and its application on fluoroscopic CT images," *Medical Physics* **34**, 246-255 (2007).
9. W. Wein, J. Z. Cheng and A. Khamene, MICCAI Workshop on Image Guidance and Computer Assistance for Soft-Tissue Interventions 2008.
10. P. Perona and J. Malik, "Scale-Space and Edge-Detection Using Anisotropic Diffusion," *Ieee Transactions on Pattern Analysis and Machine Intelligence* **12**, 629-639 (1990).
11. J. Hajnal, D. J. Hawkes and D. Hill, *Medical Image Registration*. (CRC Press, 2001).
12. M. J. D. Powell, "A Method for Minimizing a Sum of Squares of Non-Linear Functions without Calculating Derivatives," *Comput J* **7**, 303-307 (1965).

13. W. H. Press, B. P. Flannery, S. A. Teukolsky and W. T. Vetterling, *Numerical Recipes in C*, 2 ed. (Cambridge University Press, 1992).
14. T. De Silva, A. Fenster, J. Bax, C. Romagnoli, J. Izawa, J. Samarabandu and A. D. Ward, "Quantification of prostate deformation due to needle insertion during TRUS-guided biopsy: comparison of hand-held and mechanically stabilized systems," *Med Phys* **38**, 1718-1731.
15. J. M. Fitzpatrick, J. B. West and C. R. Maurer, Jr., "Predicting error in rigid-body point-based registration," *IEEE Trans Med Imaging* **17**, 694-702 (1998).
16. G. Ploussard, J. I. Epstein, R. Montironi, P. R. Carroll, M. Wirth, M. O. Grimm, A. S. Bjartell, F. Montorsi, S. J. Freedland, A. Erbersdobler and T. H. van der Kwast, "The Contemporary Concept of Significant Versus Insignificant Prostate Cancer," *European Urology* **60**, 291-303 (2011).
17. J. I. Epstein, P. C. Walsh, M. Carmichael and C. B. Brendler, "Pathologic and clinical findings to predict tumor extent of nonpalpable (stage T1c) prostate cancer," *JAMA : the journal of the American Medical Association* **271**, 368-374 (1994).

Chapter 4.

Evaluating the utility of intra-procedural 3D TRUS image information in guiding registration for motion compensation during prostate biopsy

4.1 Introduction

With the objective of improving the cancer detection rate during biopsy, systems have been developed to perform a targeted biopsy by fusing pre-biopsy MRI with 3D TRUS [1-6]. In many such systems, prior to performing biopsy, suspicious lesions delineated as targets in a pre-biopsy MR image are mapped to the static baseline 3D TRUS image acquired at the beginning of the biopsy session [7-10]. Biopsy is subsequently performed, targeting each suspicious lesion using the live 2D TRUS images acquired while tracking the ultrasound probe position and orientation relative to the baseline 3D TRUS image. However, patient or prostate motion during the procedure causes misalignments in the targets mapped to the live 2D TRUS images from the baseline 3D TRUS image.

While 2D TRUS images are widely used for intra-procedural guidance, some solutions utilize richer intra-procedural images such as bi- or multi-planar TRUS or 3D TRUS, acquired by specialized probes. Multiple algorithms have been proposed to perform software-based motion compensation by registering intra-procedural TRUS images to an initially acquired 3D TRUS image [1, 2, 5, 11]. However, intra-procedural image acquisition and initialization within the 3D coordinate system prior to registration are quite different in each method. The system

proposed in Baumann et al. [1] used a GE Voluson endorectal RIC5-9 probe (GE Healthcare, United States) to acquire 3D intra-procedural images to perform image-based tracking to compensate for motion. The 3D intra-procedural image acquisition time in that system was reported to be 0.5-5 s depending on the image quality while the subsequent non-rigid registration consumed an additional 7-8 s. In Baumann et al. [2], the authors described a similar registration approach using simultaneously acquired dual-orthogonal frames from a 3D TRUS probe as the intra-procedural images. Xu et al. [5] performed the registration after initializing several previous 2D TRUS frames in a 3D coordinate system using the transformations provided by a magnetically tracked probe. In that system, 2D TRUS frames were acquired using a Philips C9-5 2D TRUS probe (Philips Medical Systems, Seattle, WA) in real-time while the motion compensation algorithm, with an approximate execution time of 4 seconds, was triggered by the operator after visual detection of misalignment. De Silva et al. [11] previously performed a 2D-3D registration using the initialization provided by a mechanically tracked probe. The registration was performed in 1.1 seconds following the real-time acquisition of the intra-procedural image using the same conventional 2D TRUS probe (Philips Medical Systems, Seattle, WA) as in Xu et al. [5]. Both of the systems [5, 11] constructed the baseline 3D TRUS image at the beginning of the procedure using the 2D images acquired from a ~10 second rotational sweep of a tracked 2D TRUS probe. In addition, intra-procedure prostate motion has been identified as a potential problem [12] hindering accurate needle targeting in MR-guided prostate biopsy systems [13-15]. Solutions [16, 17] have been proposed for motion compensation by co-registering multi-slice intra-procedural MR images with a pre-acquired MR image.

Live intra-procedural images acquired during the biopsy procedure need to be registered both quickly and accurately to compensate for motion. During registration, we optimize an image-based similarity metric between pre- and intra-procedural images in a rigid 3D transformation space. Although prostate deformation due to TRUS probe pressure could be compensated by a non-rigid registration approach, it is less desirable considering the slower speed of non-rigid registration in the context of the short duration of the biopsy procedure and the limited time of effect of the local anesthesia provided to the patient. In addition, achieving a robust rigid registration is an essential initial step before proceeding to a non-rigid refinement. Limited anatomical context available in single plane 2D TRUS images could limit the robustness of the registration, especially considering the rotational symmetry of the prostate, as there can be multiple ways (i.e., local optima) to orient a single 2D TRUS image within the 3D context that yield high image similarity values. On the other hand, intra-procedural 3D information in multi-planar or 3D TRUS images provides richer anatomical context than in single plane 2D TRUS; this could help to improve the accuracy of the registration algorithm. Therefore, by including additional 3D image planes in the image-similarity metric calculation, the objective function shape could change due to the additional (or “richer”) anatomical information, in order to improve the robustness of the optimizer in finding the desired registration solution. However, both image acquisition and image registration require additional time when using intra-procedure 3D information. Multi-planar or 3D TRUS image acquisition either using probes with enhanced functionality or via multiple acquisitions by a rotational sweep of a tracked conventional 2D TRUS probe is slower than that using a near real time conventional 2D TRUS probe. Moreover, image registration requires more time when using intra-procedural 3D TRUS images to calculate the image similarity metric values using more intensity samples.

In order to design a suitable approach to compensate for prostate motion, taking into account these tradeoffs between accuracy and speed, it is useful to quantify the improvements in registration accuracy obtained by acquiring different amounts of 3D information in the intra-procedural TRUS images. In this work, (1) we compared the motion compensation accuracies resulting from the use of several potential intra-procedural imaging approaches, ranging from single 2D TRUS frames to full 3D TRUS imaging, to evaluate how different amounts of 3D image information affect the registration accuracy; (2) we analysed how frequently and in which anatomic regions of the prostate the motion compensation accuracy benefits most from additional 3D image information acquired during the procedure; and (3) we investigated whether rigid alignments obtained via image-based registration could achieve accuracies suitable for use in a clinical setting. Our results could inform the designers of next-generation guided prostate biopsy systems as to (1) optimal design/selection of ultrasound imaging techniques to be used intra-procedurally; (2) whether and how to adaptively acquire additional 3D information when the physician is targeting specific regions of the prostate; and (3) whether to invest effort in the development of real-time non-rigid registration for prostate motion compensation during the procedure.

4.2 Materials and methods

4.2.1 Materials

29 patients (mean \pm std age: 59 ± 7 , PSA: 5.4 ± 2.8 ng/ml, prostate volume: 38.8 ± 20.0 cm³) were included in this study that was part of a larger human subjects research ethics board approved MRI-3D TRUS fusion biopsy study. The 3D TRUS images were collected in advance of the scheduled biopsy as part of our institution's standard protocol to fuse MRI to pre-biopsy

3D TRUS images. 3D TRUS images were acquired with a mechanically tracked 3D TRUS-guided biopsy system described in Bax et al. [3], using a commercially available end-firing 5-9 MHz HDI 5000 TRUS transducer probe (Philips Medical Systems, Seattle, WA). During 3D TRUS image reconstruction, a set of 2D TRUS images was acquired by a 180 degree probe-axial rotation of the otherwise stationary TRUS probe (i.e., the entire probe is rotated, including its outer surface) and then resampled the resulting 2D planes in a 3D grid to obtain the 3D TRUS image. Each 3D TRUS volume had a grid size of $224 \times 224 \times 175$ voxels, with an isotropic voxel size of 0.37 mm, and was preprocessed via anisotropic diffusion filtering [18] (conductance parameter = 2, time step = 0.625) for speckle reduction. Each 3D TRUS image acquisition required approximately 10 seconds.

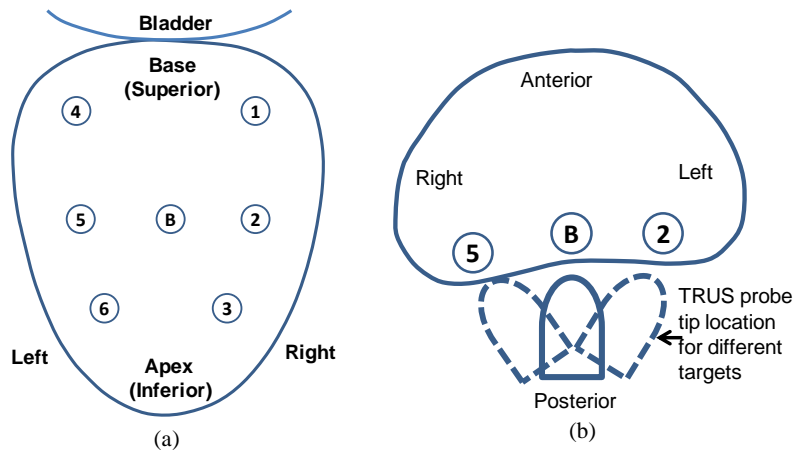


Figure 4.1: (a) Coronal view (from the posterior perspective of the TRUS probe) of relative positions of the probe tip during image acquisition (B: baseline, 1-6: sextant locations) (b) Transverse view showing the necessary reorientation of the probe to acquire images at baseline and targets 2 and 5.

A total of 7 3D TRUS volumes were acquired per patient, with the first image acquired centrally within the gland—corresponding to the typical baseline 3D TRUS image acquired at the start of most MRI-TRUS fusion biopsy procedures [5, 11]. The six additional 3D TRUS images were acquired after maneuvering the TRUS probe toward each of the sextant biopsy

locations. Figure 4.1 shows the relative bilateral sextant biopsy locations in the base, mid-gland and apex regions of the prostate when acquiring 3D TRUS images by a rotational sweep of the TRUS probe at each position. The order of sextant 3D TRUS acquisitions was reversed for half of the patients (the order from 1 to 6 were reversed to 6 to 1 according to the positions shown in Figure 4.1) in an effort to mitigate possible dependence of prostate motion at each sextant location to the previous probe position.

Each sextant 3D TRUS image comprises a set of 2D TRUS images that could be acquired using a conventional 2D TRUS probe when targeting a region in that sextant. The mechanical encoders attached to the ultrasound probe tracked the 3D position and orientation of the individual 2D TRUS images acquired during the rotational sweep, yielding a transformation of every 2D TRUS image to a common 3D world coordinate system. The 7 3D images indicated by probe positions in Figure 4.1 were acquired from 29 patients, for a total of 203 3D TRUS images. During registration, surrogate intra-procedural images were extracted from the 3D TRUS images acquired at the bilateral sextant probe positions that simulated different 3D TRUS-guided biopsy scenarios while the 3D TRUS image acquired at the baseline probe position served as the pre-procedural image.

4.2.2 Image registration

For all registrations, the 3D TRUS image at the baseline position (I_B) was used as the moving image to update the target locations in the baseline image to compensate for motion. We used several different fixed image configurations, ranging from a single 2D TRUS plane to a full 3D TRUS image; Figure 4.2 lists the notations for the fixed image configurations used in the registration experiments in this paper, along with a schematic description of each. The fixed

images extracted from 3D TRUS images at sextant probe positions are denoted as $I_{\alpha_1, \alpha_2, \dots, \alpha_n}$, where n is the number of planes extracted from angles α , or $I_{\alpha_1-\alpha_2}$ for all planes between angles α_1 and α_2 ; $\alpha = 0$ denotes the transverse or axial plane. Thus, at one end of a continuum, I_0 indicates the use of a single transverse 2D TRUS image as the fixed image, and at the other end, I_{0-179} indicates the full 3D TRUS image. Extracting different planes from the 3D TRUS image to construct the fixed image (illustrated in Figure 4.2) simulates intra-procedural images for different intra-procedural scenarios, ranging from monoplanar 2D TRUS imaging [5, 11], through multi-planar and partial volume imaging [2], to full 3D TRUS imaging [1] conducted throughout the procedure.









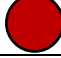
Fixed image	Planes extracted	Fixed image	Planes extracted	Fixed image	Planes extracted
I_0		$I_{0,90}$		I_{0-45}	
$I_{0,45}$		$I_{0,45,135}$		I_{0-90}	
$I_{0,135}$		$I_{0,45,90,135}$		I_{0-179}	

Figure 4.2: Fixed image configurations used in this paper: notation and schematics of planes from a probe-axis view.

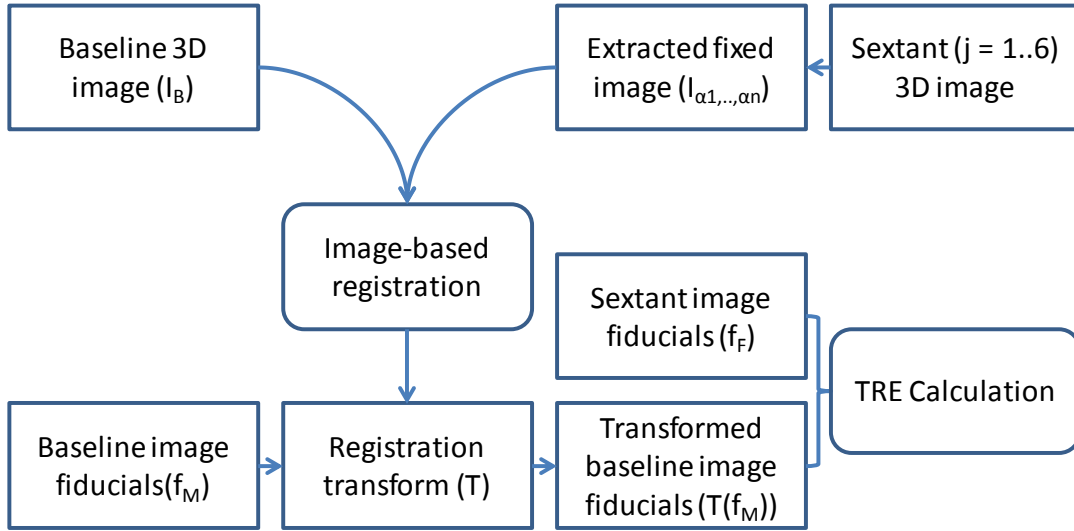


Figure 4.3: Overall workflow in methods and validation.

For each fixed image configuration given in Figure 4.2, registration and validation were performed according to the overall workflow given in Figure 4.3. During image-based registration, the transformation from the mechanical tracker initialized the subsequent rigid registration performed by optimizing the normalized cross-correlation [19] (NCC) using Powell's method [20] as the optimizer, as described in De Silva et al. [11]. A total of 174 registrations were performed on images of 29 patients (6 registrations per patient) for each construction of fixed images according to Figure 4.2. For each patient $i = 1 \dots 29$ and fixed image constructions with different probe positions $j = 1 \dots 6$ we optimized the objective function given by normalized cross-correlation as

$$T^{ij} = \mathop{\text{arg max}}_{i,j} NCC(I_{\alpha_1, \dots, \alpha_n}^{ij}, I_B^i; \tilde{T}^{ij})$$

to determine the rigid transformation T^{ij} corresponding to the motion.

4.2.3 Registration error measurement

Although the patient was in the lateral decubitus position during 3D TRUS image acquisitions, patient discomfort and TRUS probe pressure can cause prostate motion. Therefore, the ultrasound probe tracking information cannot be used to determine the motion of the prostate, since the prostate may have moved relative to the probe. This motion was quantified relative to manually identified intrinsic fiducials (micro-calcifications) of the prostate. Registration error was measured as the root mean square (RMS) target registration error (TRE) [21, 22] of manually identified corresponding pairs of fiducials for every registered 3D TRUS image pair. It is important to note that the fiducial pairs were identified only to measure the accuracy of registration and were not provided as input to the registration algorithm. Fiducials were identified throughout the 3D TRUS images regardless of the planes used for registration and the k^{th} fiducial in the fixed image of the i^{th} patient in the j^{th} sextant position is denoted by f_F^{ijk} and the fiducials in the moving image by f_M^{ik} . Using the transformation ($T_{\alpha_1, \dots, \alpha_n}^{ij}$) obtained from the registrations at each fixed image configuration, the RMS TRE was calculated as

$$TRE_{\alpha_1, \dots, \alpha_n} = \sqrt{\frac{\sum_{i,j,k} (f_F^{ijk} - T_{\alpha_1, \dots, \alpha_n}^{ij}(f_M^{ik}))^2}{N}}.$$

4.2.4 Experimental methods

A total of 1003 fiducial pairs were identified across image pairs of all patients with a mean \pm standard deviation (std) of 5.8 ± 1.2 fiducial pairs per registration. Figure 4.4 shows the distribution of the identified fiducials projected to Anterior/Posterior (A-P), Left/Right (L-R) and Inferior/Superior (I-S) planes from the 3D space, with the prostate size normalized from 0 to 1

along each direction. Figure 4.5 depicts the sample calcification pairs that were identified as the anatomical landmarks.

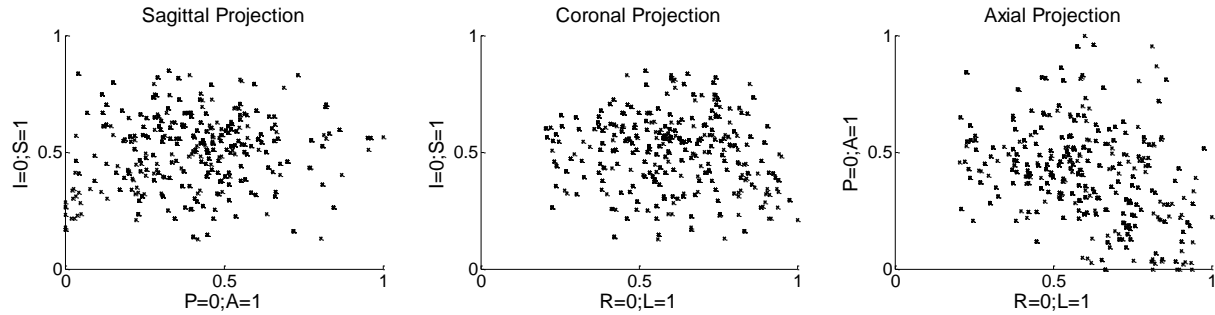


Figure 4.4: Distribution of manually identified fiducials used for registration validation. Each fiducial is shown with its Anterior/Posterior (A/P), Left/Right (L/R) and Inferior/Superior (I/S) position within the normalized prostate in which the boundaries extend from 0 to 1 along each direction.

4.2.5 TRE for different fixed image configurations

The $\text{RMS} \pm \text{std TRE}$ was calculated for each registration using the fixed image configurations defined in Figure 4.2. To provide context for interpretation of these results, the pre-registration error and the fiducial registration error (FRE) [21] were also calculated. To compare the two extremes of fixed image information (2D versus full 3D), the distribution of TRE improvements ($TRE_0^{ij} - TRE_{0-179}^{ij}$) were calculated when using a full 3D TRUS image as opposed to using a single 2D TRUS image for motion compensation.

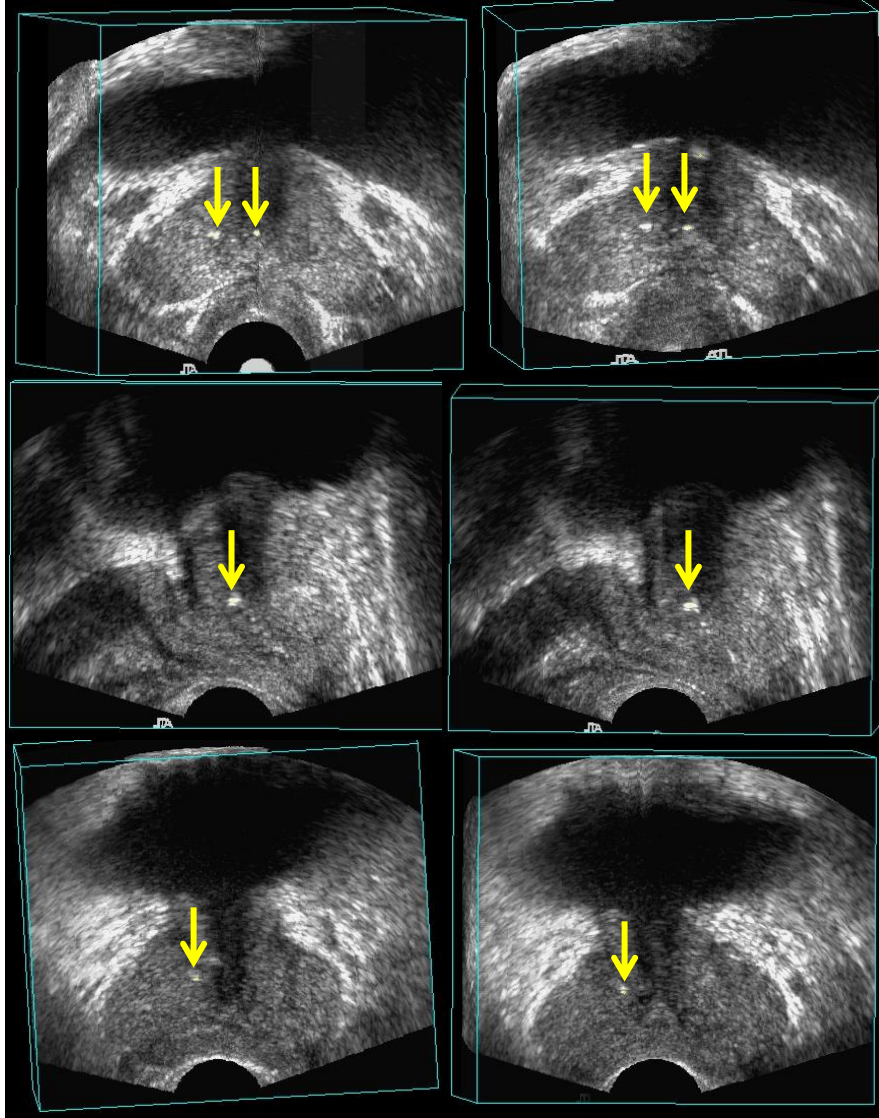


Figure 4.5: Example of the identified fiducials for three pairs of images. Arrows point to homologous fiducial pairs in each row. Baseline images with the fiducials are shown in the left and the sextant images of the same patient with corresponding fiducials are shown in the right.

4.2.6 TRE for base, mid-gland and apex regions

The TRE distributions were analysed separately for mid, base and apex regions of the prostate to understand the benefit of using additional 3D image planes in each region. The TRE for each probe position was calculated separately as

$$TRE^j_{\alpha_1, \dots, \alpha_n} = \sqrt{\frac{\sum_{i,k} (f_F^{ijk} - T_{\alpha_1, \dots, \alpha_n}^{ij}(f_M^{ik}))^2}{N^j}}$$

To determine an optimal registration error against which to compare the TREs, we calculated the FRE resulting from the rigid transformation that optimally aligned the intrinsic fiducials. The FRE was calculated by finding the optimal rigid transformation that yielded the least squared error for the fiducials in a given image pair as

$$FRE^{ij} = \arg \min_{T^{ij}} \sqrt{\frac{\sum_k (f_F^{ijk} - T^{ij}(f_M^{ik}))^2}{N^k}}$$

4.3 Results

4.3.1 TRE for different fixed image configurations

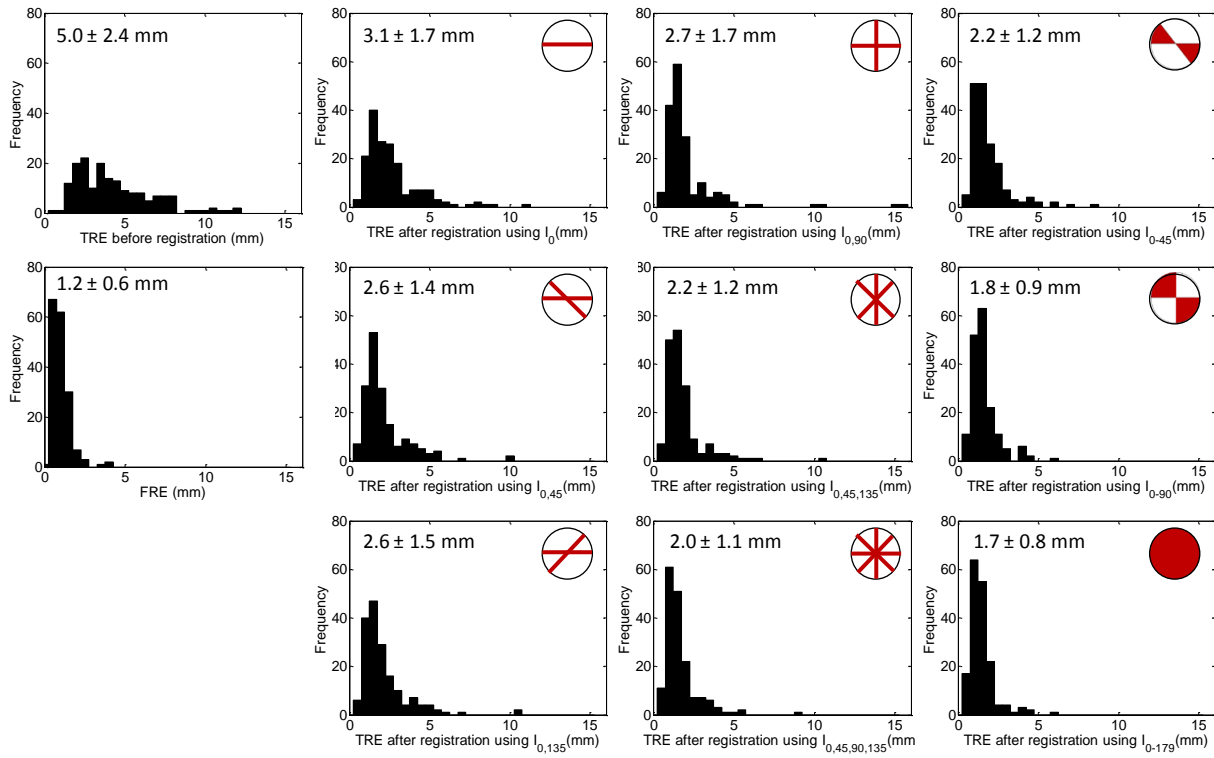


Figure 4.6: TRE histograms for registrations using different fixed images, with the RMS \pm std TRE shown in the top left of each histogram. To provide context for the TRE distributions, row 1, column 1 shows the error distribution prior to registration and row 2, column 1 shows the error distribution after optimal rigid registration using the fiducials (FRE).

Figure 4.6 shows the RMS \pm std TRE for registration using each fixed image configuration defined in Figure 4.2, along with the pre-registration error and the FRE and the histograms of

each distribution. Since these TRE distributions were found to be not normally distributed by a one-sample Komogorov-Smirnov test ($p > 0.05$), for each pairing of fixed image configurations we tested the null hypothesis that the paired distributions have the same medians with the non-parametric Wilcoxon signed rank test. The null hypothesis was rejected for each pair of distributions ($p < 0.006$) except for the pair of distributions with fixed images as $I_{0,45}$ and $I_{0,135}$ ($p = 0.2$). The RMS TRE decreased monotonically with an increasing number of planes included in the fixed image configuration. The lowest and least variable error was obtained when the fixed image was selected to be the full 3D image (I_{0-179}). Figure 4.7 compares the parameters of the TRE distributions at different fixed image configurations as a box and whisker plot. To directly compare the extremes of fixed image configurations, Figure 4.8 shows the histogram of distribution of TRE error reductions resulting from the use of a 3D fixed image configuration, compared to a 2D fixed image configuration, calculated as $TRE_0^{ij} - TRE_{0-179}^{ij}$. Figure 4.9 shows qualitative examples of the alignments provided by registration with different fixed image configurations, for three patients. Mean execution times for registrations with single-plane, bi-plane, partial-volume, and full 3D volume fixed image configurations are shown in Table 4.1. The time required increases with more intensity samples used for registration. The times were measured using a graphics processing unit (GPU) accelerated implementation of the NCC calculation with NVIDIA GTX 580 (NVIDIA Corporation, Santa Clara, CA) GPU and an Intel Xeon 2.5 GHz processor (Intel Corporation, Santa Clara, CA).

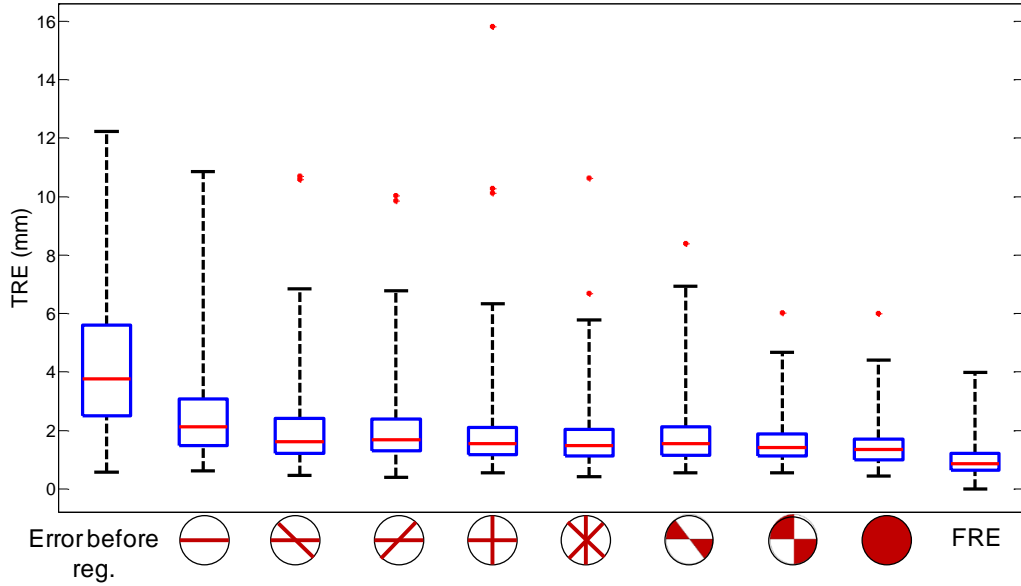


Figure 4.7: Comparison of TRE distribution parameters for different fixed image configurations.

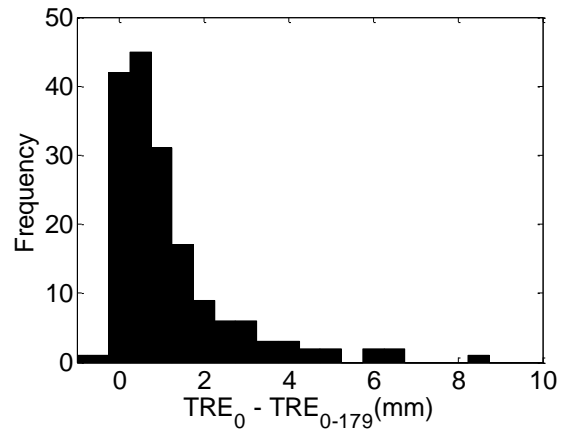


Figure 4.8: Histogram of TRE differences between I_0 and I_{0-179} .

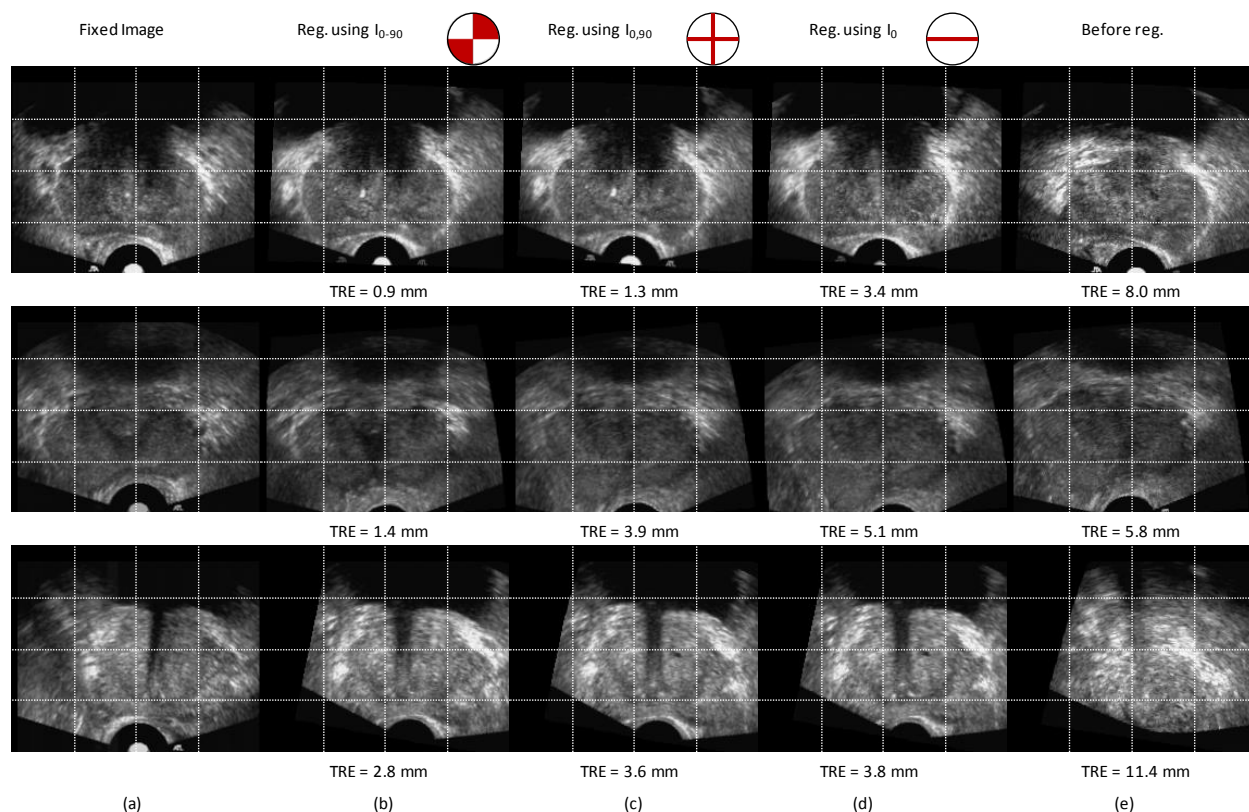



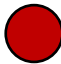


Figure 4.9: Corresponding transverse 2D planes from; (a) fixed image, (b)-(d) transformed moving image after registration using the fixed image configurations as indicated, (e) moving image before registration.

Table 4.1: Mean execution times for registration with different fixed image configurations

Fixed image configuration	Mean execution time (s)*
TRE_0 	1.8
$TRE_{0,90}$ 	2.1
TRE_{0-90} 	8.0
TRE_{0-179} 	14.6

*Using a GPU accelerated implementation for NCC calculation (NVIDIA GTX 580 GPU card and Intel Xeon 2.5 GHz processor)

4.3.2 TRE for base, mid-gland and apex regions

In Table 4.2, we present the average TRE values in base, mid and apex regions of the prostate as well as TRE separately for each sextant region for two fixed image configurations: single plane

and full 3D TRUS image. The error before registration as well as TRE_0 using a single plane was higher in the base and apex regions of the prostate when compared with the mid-gland; for both distribution pairs, the non-parametric Wilcoxon signed rank test rejected the null hypothesis ($p < 0.001$) that the paired distributions had the same median. The observed motion during biopsy movements within the left gland of the prostate was significantly larger (Wilcoxon signed rank test, $p < 0.001$) than that of the right gland even though the order of left to right and right to left acquisitions were reversed for half of the patients during image acquisitions. The additional improvement in TRE ($TRE_0^j - TRE_{0-179}^j$) when using full 3D information as opposed to using a single plane for registrations, was larger (Wilcoxon signed rank test, $p < 0.07$) in the base and apex regions when compared with the improvements obtained in the mid-gland. However, at the 95% confidence level ($p = 0.05$) there was no significant difference between base, apex regions and the mid-gland detected.

Table 4.2: RMS \pm std TREs for registrations at different sextant probe positions.

Sextant position (j)	Before reg. (mm)	FRE (mm)	TRE_0^j (mm)	TRE_{0-179}^j (mm)	$TRE_0^j - TRE_{0-179}^j$ (mm)
Base	5.3 \pm 2.6	1.2 \pm 0.6	3.4 \pm 1.8	1.7 \pm 0.7	1.7
– Left base	4.6 \pm 2.6	1.1 \pm 0.5	2.8 \pm 1.6	1.5 \pm 0.6	1.3
– Right base	5.9 \pm 2.4	1.4 \pm 0.7	3.9 \pm 1.8	1.9 \pm 0.9	2.0
Mid	4.1 \pm 2.1	0.9 \pm 0.4	2.2 \pm 1.0	1.3 \pm 0.5	0.9
– Left mid	3.0 \pm 1.5	1.0 \pm 0.4	1.6 \pm 0.6	1.3 \pm 0.5	0.3
– Right mid	5.0 \pm 2.2	0.9 \pm 0.3	2.7 \pm 1.2	1.3 \pm 0.5	1.4
Apex	5.3 \pm 2.2	1.2 \pm 0.7	3.5 \pm 1.9	1.9 \pm 1.0	1.6
– Left apex	4.1 \pm 1.5	1.4 \pm 0.8	3.0 \pm 1.4	2.1 \pm 1.2	0.9
– Right apex	6.3 \pm 2.4	1.2 \pm 0.5	4.0 \pm 2.3	1.7 \pm 0.7	2.3

4.4 Discussion

In this work, we compared the accuracy and robustness of prostate motion compensation during TRUS-guided biopsy when varying amounts of 3D image content are available in the live images used for guidance, ranging from 2D images such as would be acquired from a conventional monoplanar probe, through bi- and multi-planar images, to full 3D TRUS imaging. The results could inform the selection of a suitable approach in a clinical setting considering the trade-offs in accuracy, time and hardware costs. Although 3D information has aided the registration algorithm in converging robustly to more accurate solutions, image acquisition and registration requires more time when using such information, and probe costs may increase. In previously published approaches for 3D TRUS-guided biopsy [1, 5, 11], additional intra-procedural images have been obtained using the probes with enhanced functionality (the system described in Baumann et al. [1] requires 0.5–5s per temporal frame of acquisition) or could potentially be obtained via the rotation of a tracked TRUS probe prior to each biopsy (the systems described in Xu et al. [5] and De Silva et al. [11] require ~10s for a full 3D TRUS acquisition). Whereas the former approach allows for more convenient acquisition of multiplanar images, the latter approach permits the use of widely available conventional 2D TRUS probes in systems that provide 3D TRUS guidance (e.g., by retrofitting, as in [3]), lowering the cost barrier to entry into 3D TRUS-guided biopsy and leveraging the physician’s investment in existing 2D ultrasound machines. For example, Xu et al. [5] proposed a method of incorporating additional 3D information by selecting frames with the largest separation in translations and rotations in the out-of-plane directions using the probe’s tracking information from the set of live 2D TRUS frames prior to targeting. This approach uses the natural motion of the handheld probe over a short time period prior to biopsy to acquire additional planes. As another example, the

mechanical system in Bax et al. [3] permits acquisition of additional imaging planes via the rotation of the tracked TRUS probe. This system provides mechanical stabilization of the probe (including optional mechanical locking of all joints, permitting only axial probe rotation), which in principle could result in reduced prostate motion during acquisition.

The co-registration to compensate for prostate motion could be improved further by applying a subsequent non-rigid refinement after the rigid registration, thereby compensating for the prostate deformation caused by the variability in TRUS probe pressure. However, this clinical application requires high-speed registration; the higher degrees-of-freedom of a non-rigid transformation render high-speed registration very challenging. The FRE calculated using manually identified intrinsic fiducials yields the error after an optimal rigid registration. The FRE provides information about the room for improvement that may be obtained from a non-rigid registration, to shed light on the potential return on investment of effort in development of high-speed non-rigid image registration algorithms for this clinical procedure. We calculated an overall RMS \pm std FRE of 1.2 ± 0.6 mm, which indicates that an optimal rigid alignment could achieve a clinically desirable level of accuracy (i.e., < 2.5 mm RMS error [23]), possibly eliminating the need to implement a more time-consuming non-rigid registration algorithm. Our results show that the TRE values approached the FRE when including 3D intra-procedural imaging during registration. Moreover, previous work [1, 22] suggests that non-rigid registration yielded RMS TRE improvements < 0.6 mm when using intra-procedural 3D TRUS images. Therefore, the use of intra-procedural 3D TRUS imaging with rigid registration seems to provide a larger incremental benefit than the use of non-rigid registration.

The development of image registration methods to compensate for motion could have applications in other 3D guided diagnostic and therapeutic interventional procedures [24, 25].

Hungr et al. [25] describe a 3D ultrasound robotic prostate brachytherapy system that utilizes motion compensation algorithms previously validated for biopsy guidance. The limited anatomical context available in single-plane 2D intra-procedural images could challenge the accuracy of co-registration with 3D pre-procedural images in many other interventional applications. Uneri et al. evaluated the effect of dual projection view angles on 3D-2D registration accuracy of CT and x-ray projection images for surgical guidance. Zvonarev et al. [26] and Fallavollita et al. [27] described multiple 2D plane-3D registrations related to lung and prostate brachytherapy. The methods described in this paper could have relevance in developing and evaluating techniques to improve registration accuracy and robustness in such interventional applications requiring rapid, robust registration by acquiring intra-procedural 3D imaging efficiently, only when necessary.

4.4.1 TRE for different fixed image configurations

The TREs for bi-planar registrations shown in Figure 4.6 do not indicate substantial variability in accuracy for the different angles between the two planes tested for those three fixed image configurations (i.e., $I_{0,45}$, $I_{0,135}$, $I_{0,90}$). The acquisition of a partial volume up to the angle of rotation with a conventional tracked monoplanar probe may support more accurate motion compensation than acquiring a single additional plane. Consequently, that approach could result in more robust registrations than with a probe that simultaneously acquires dual orthogonal planes, at the cost of extra time for rotational acquisitions.

According to the TRE_0 distribution in Figure 4.6, 63% of the registrations have a TRE < 2.5 mm when using a single 2D TRUS image as the fixed image configuration. Figure 4.8 shows the histogram of distribution of TRE improvements calculated as $TRE_0^{ij} - TRE_{0-179}^{ij}$.

According to this distribution, the improvements were less than 1 mm in 56% of all registrations and were less than 2.5 mm in 87% of the registrations. This suggests that although 3D information improved the accuracy and robustness of the registration, in the majority of the cases the error when using a single 2D TRUS plane was within a clinically acceptable range [23] or the improvements were not substantial when additional planes were included in the registration. Intra-procedural detection of misregistration by the operator could direct the efficient use of 3D image acquisition only for the subset of cases where this is beneficial.

4.4.2 TRE for base, mid-gland and apex regions

The analysis of TRE separately in the different sextant regions indicated that the base and apex regions were more challenging for the registration algorithm to compensate when only using a single 2D TRUS image, as compared with mid-gland regions. The additional 3D TRUS information provided during registration was generally more beneficial in the base and apex regions, yielding higher comparative accuracy improvements as shown in Table 1.2. When the TRUS probe is positioned near the edge of the gland at the base or apex, the resulting transverse 2D views contain minimal prostate anatomy, which may not be sufficient to unambiguously co-register with the pre-acquired baseline 3D TRUS image. In order for the image-based registration to be successful in such challenging cases, it is reasonable to expect that the image content needs to capture richer contextual information, which can be achieved through oblique 2D views or 3D partial volumes.

4.4.3 Limitations

The registration error (TRE) measurements in this paper were made using manually identified intrinsic fiducial landmarks within the prostate. Therefore, the TRE measurements are limited

by the fiducial localization error (FLE) in 3D TRUS images, which were measured to be 0.21 mm in a previous study [22] involving 3D TRUS images. Fiducials were identified in baseline and sextant 3D TRUS images, irrespective of the planes used for registration in different fixed image configurations. Therefore, when using fewer planes than the complete 3D TRUS image, the registration algorithm lacks complete information to calculate the optimal rigid transform for the identified fiducials. While rigid motion of the prostate was assumed, any presence of non-rigid motion would challenge the ability of the registration algorithm to reach the ground truth measured by the identified fiducials using fewer image planes. FRE, calculated as the lowest possible error after applying a rigid transformation, is reflective of the magnitude of non-rigid deformation of the prostate. Our results show that TRE approaches FRE when increasing the amount of intra-procedural 3D-TRUS image information during registration. The remaining difference between the FRE and TRE_{0-179} could possibly be attributed to the FLE and the vulnerability of the registration optimizer in converging to local optima even when using full 3D TRUS images.

The results presented in this paper are applicable to biopsy systems that utilize 3D guidance (e.g., Artemis [Eigen, Grass Valley, CA, USA], UroNav [In Vivo, USA], Urostation [Koelis, Grenoble, France], BiopSee [Pi Medical, Athens, Greece], Virtual Navigator [Esaote, Italy], Real-time Virtual Sonography [HI RVS] [Hitachi, Japan]). Furthermore, in our study, the 3D TRUS images were acquired using a manually rotated, tracked, and mechanically stabilized 2D TRUS probe.

4.5 Conclusion

In 3D TRUS-guided biopsy, accurate and rapid registration of live intra-procedural images to a pre-acquired 3D TRUS image is necessary to minimize targeting errors. Intra-procedural 3D TRUS information supports robust convergence of the registration algorithm to more accurate solutions while compensating for motion. Intra-procedural 3D TRUS information could be acquired either using probes with enhanced functionality (multi-planar or 3D probes) or by axial rotation of a tracked conventional 2D TRUS probe. The acquisition of a partial volume up to the angle of rotation supported more accurate motion compensation than acquiring bi-plane configurations. The results are helpful for devising mechanisms for motion compensation by taking advantage of intra-procedural 3D image acquisitions, considering the tradeoff of time, probe cost, and accuracy of motion compensation. In 3D TRUS-guided biopsy systems, 3D intra-procedural image acquisitions help to achieve a robust registration that could improve the needle targeting accuracies to meet the clinical demands of such systems.

References

1. M. Baumann, P. Mozer, V. Daanen and J. Troccaz, "Prostate biopsy tracking with deformation estimation," *Med Image Anal* **16**, 562-576 (2013).
2. M. Baumann, P. Mozer, V. Daanen and J. Troccaz, "Prostate biopsy assistance system with gland deformation estimation for enhanced precision," *Med Image Comput Comput Assist Interv* **12**, 67-74 (2009).
3. J. Bax, D. Cool, L. Gardi, K. Knight, D. Smith, J. Montreuil, S. Sherebrin, C. Romagnoli and A. Fenster, "Mechanically assisted 3D ultrasound guided prostate biopsy system," *Med Phys* **35**, 5397-5410 (2008).
4. D. Cool, S. Sherebrin, J. Izawa, J. Chin and A. Fenster, "Design and evaluation of a 3D transrectal ultrasound prostate biopsy system," *Med Phys* **35**, 4695-4707 (2008).
5. S. Xu, J. Kruecker, B. Turkbey, N. Glossop, A. K. Singh, P. Choyke, P. Pinto and B. J. Wood, "Real-time MRI-TRUS fusion for guidance of targeted prostate biopsies," *Comput Aided Surg* **13**, 255-264 (2008).
6. O. Ukimura, M. M. Desai, S. Palmer, S. Valencerina, M. Gross, A. L. Abreu, M. Aron and I. S. Gill, "3-Dimensional elastic registration system of prostate biopsy location by real-time 3-dimensional transrectal ultrasound guidance with magnetic resonance/transrectal ultrasound image fusion," *J Urol* **187**, 1080-1086 (2012).
7. G. A. Sonn, S. Natarajan, D. J. A. Margolis, M. MacAiran, P. Lieu, J. T. Huang, F. J. Dorey and L. S. Marks, "Targeted Biopsy in the Detection of Prostate Cancer Using an Office Based Magnetic Resonance Ultrasound Fusion Device," *Journal of Urology* **189**, 86-91 (2013).
8. M. M. Siddiqui, S. Rais-Bahrami, H. Truong, L. Stamatakis, S. Vourganti, J. Nix, A. N. Hoang, A. Walton-Diaz, B. Shuch, M. Weintraub, J. Kruecker, H. Amalou, B. Turkbey, M. J. Merino, P. L. Choyke, B. J. Wood and P. A. Pinto, "Magnetic Resonance Imaging/Ultrasound-Fusion Biopsy Significantly Upgrades Prostate Cancer Versus Systematic 12-core Transrectal Ultrasound Biopsy," *European Urology* **64**, 713-719 (2013).
9. P. A. Pinto, P. H. Chung, A. R. Rastinehad, A. A. Baccala, J. Kruecker, C. J. Benjamin, S. Xu, P. K. Yan, S. Kadoury, C. Chua, J. K. Locklin, B. Turkbey, J. H. Shih, S. P. Gates, C. Buckner, G. Bratslavsky, W. M. Linehan, N. D. Glossop, P. L. Choyke and B. J. Wood, "Magnetic Resonance Imaging/Ultrasound Fusion Guided Prostate Biopsy Improves Cancer Detection Following Transrectal Ultrasound Biopsy and Correlates With Multiparametric Magnetic Resonance Imaging," *Journal of Urology* **186**, 1281-1285 (2011).
10. N. B. Delongchamps, M. Peyromaure, A. Schull, F. Beuvon, N. Bouazza, T. Flam, M. Zerbib, N. Muradyan, P. Legman and F. Cornud, "Prebiopsy Magnetic Resonance Imaging

- and Prostate Cancer Detection: Comparison of Random and Targeted Biopsies," *Journal of Urology* **189**, 493-499 (2013).
11. T. De Silva, A. Fenster, D. Cool, L. Gardi, C. Romagnoli, J. Samarabandu and A. D. Ward, "2D-3D rigid registration to compensate for prostate motion during 3D-TRUS guided biopsy," *Medical Physics* **40**, 022904 (2013).
 12. H. Xu, A. Lasso, S. Vikal, P. Guion, A. Krieger, A. Kaushal, L. L. Whitcomb and G. Fichtinger, "Accuracy validation for MRI-guided robotic prostate biopsy," in *SPIE Medical Imaging: Visualization, Image-Guided Procedures*, (San Diego, CA, USA, 2010), pp. 762517 - 762517-762518.
 13. A. Krieger, Iordachita, II, P. Guion, A. K. Singh, A. Kaushal, C. Menard, P. A. Pinto, K. Camphausen, G. Fichtinger and L. L. Whitcomb, "An MRI-compatible robotic system with hybrid tracking for MRI-guided prostate intervention," *IEEE Trans Biomed Eng* **58**, 3049-3060 (2011).
 14. A. Krieger, R. C. Susil, C. Menard, J. A. Coleman, G. Fichtinger, E. Atalar and L. L. Whitcomb, "Design of a novel MRI compatible manipulator for image guided prostate interventions," *IEEE Trans Biomed Eng* **52**, 306-313 (2005).
 15. J. Tokuda, K. Tuncali, I. Iordachita, S. E. Song, A. Fedorov, S. Oguro, A. Lasso, F. M. Fennessy, C. M. Tempany and N. Hata, "In-bore setup and software for 3T MRI-guided transperineal prostate biopsy," *Phys Med Biol* **57**, 5823-5840 (2012).
 16. A. Lasso, A. Fedorov, J. Fairhurst, J. Tokuda, K. Tuncali, R. Mulkern, N. Hata, C. M. Tempany and G. Fichtinger, "Multi-slice-to-volume registration for reducing targeting error during MRI-guided transrectal prostate biopsy," in *The 9th International Interventional MRI Symposium*, (Boston, MA, USA, 2012).
 17. H. Tadayyon, A. Lasso, A. Kaushal, P. Guion and G. Fichtinger, "Target motion tracking in MRI-guided transrectal robotic prostate biopsy," *IEEE Trans Biomed Eng* **58**, 3135-3142 (2011).
 18. P. Perona and J. Malik, "Scale-Space and Edge-Detection Using Anisotropic Diffusion," *Ieee Transactions on Pattern Analysis and Machine Intelligence* **12**, 629-639 (1990).
 19. J. Hajnal, D. J. Hawkes and D. Hill, *Medical Image Registration*. (CRC Press, 2001).
 20. W. H. Press, B. P. Flannery, S. A. Teukolsky and W. T. Vetterling, *Numerical Recipes in C*, 2 ed. (Cambridge University Press, 1992).
 21. J. M. Fitzpatrick, J. B. West and C. R. Maurer, Jr., "Predicting error in rigid-body point-based registration," *IEEE Trans Med Imaging* **17**, 694-702 (1998).

22. V. V. Karnik, A. Fenster, J. Bax, D. W. Cool, L. Gardi, I. Gyacskov, C. Romagnoli and A. D. Ward, "Assessment of image registration accuracy in three-dimensional transrectal ultrasound guided prostate biopsy," *Med Phys* **37**, 802-813 (2010).
23. J. I. Epstein, H. Sanderson, H. B. Carter and D. O. Scharfstein, "Utility of saturation biopsy to predict insignificant cancer at radical prostatectomy," *Urology* **66**, 356-360 (2005).
24. Z. Wei, G. Wan, L. Gardi, G. Mills, D. Downey and A. Fenster, "Robot-assisted 3D-TRUS guided prostate brachytherapy: system integration and validation," *Med Phys* **31**, 539-548 (2004).
25. N. Hungr, M. Baumann, J. A. Long and J. Troccaz, "A 3-D Ultrasound Robotic Prostate Brachytherapy System With Prostate Motion Tracking," *Ieee Transactions on Robotics* **28**, 1382-1397 (2012).
26. P. S. Zvonarev, T. J. Farrell, R. Hunter, M. Wierzbicki, J. E. Hayward and R. K. Sur, "2D/3D registration algorithm for lung brachytherapy," *Medical Physics* **40** (2013).
27. P. Fallavollita, C. Burdette, D. Song, P. Abolmaesumi and G. Fichtinger, "C-arm Pose Estimation in Prostate Brachytherapy by Registration to Ultrasound," *Medical Image Computing and Computer-Assisted Intervention - Miccai 2010, Pt Iii* **6363**, 311-318 (2010).

Chapter 5.

Robust 2D-3D registration optimization to motion compensation using learned prostate motion data

5.1 Introduction

In this chapter, we describe and evaluate a 2D-3D TRUS registration that incorporates knowledge of prostate motion characteristics into the optimization process in order to improve registration accuracy and robustness. Although 3D intra-procedure image acquisitions could help to improve the robustness of the registration algorithm as described in the previous chapter, it is faster, more economical and less cumbersome to acquire live 2D TRUS images and to use them in registration for motion compensation during the procedure. A robust 2D-3D registration algorithm would combine the advantages of more convenient live 2D TRUS acquisitions during the procedure with the improvements in motion compensation accuracy and robustness.

Multiple algorithms have been proposed [1-4] to perform software-based motion compensation by registering intra-procedural TRUS images to an initially acquired 3D TRUS image. The system proposed in [3] used TRUS images acquired from a 3D TRUS probe to perform image-based tracking to compensate for motion. Xu et al.[1] performed the registration after initializing several previous 2D TRUS frames in a 3D coordinate system using the transformations provided by a magnetically tracked probe. We previously [2] proposed a 2D-3D registration method using an initialization provided by a mechanically-tracked probe. The registration needs to be performed in a transformation space of, at minimum, 6 dimensions (for rigid registration), and the non-convexity of the objective function in the search space can drive the optimizer to local optima. The methods in [1, 2] rely on some initialization mechanism and then optimize an

image-based, non-linear cost function using a local optimization technique whereas in [3] an initial global search mitigated local optima in the subsequent Powell-Brent search. While 2D-3D registration using a conventional real-time TRUS probe could be more challenging than 3D-3D registration [3] using a 3D TRUS probe, motion compensation with low inter-patient registration error variability and increased robustness is vital for successful clinical integration. In this work, we investigated whether, in a 2D-3D registration problem, the learned characteristics of motion induced at different probe positions for prostates can be used to overcome local optima and drive the optimization to converge to the desired solution.

Statistical representations of high-dimensional transformations have been used to learn prostate deformations to improve MR-TRUS registration [5, 6]. However, statistical analyses have been previously performed using finite element analysis (FEA)-simulated motion in 3D TRUS images [5] and phantoms [6] whereas this work utilized statistics of observed motion in actual prostate interventions. Outside of the prostate TRUS context, statistical representations of high-dimensional transformations have been previously used to learn or constrain both rigid and non-rigid registrations [7-9]. Strategies have also been proposed to improve the robustness of optimization techniques during registration [10].

The objective of this work is to utilize the statistics of observed prostate motion data to improve the robustness of registration optimization. In this work, we analysed the prostate motions observed from 29 patients to learn a model representing the characteristics of prostate motion. We then incorporated the parameters from this model to improve the robustness of the registration optimization. The rest of the paper describes our approach to learning of prostate motion characteristics and our adaptation of that learned statistical information to improve the search for the optimum of the cost function.

5.2 Materials and Methods

5.2.1 Data acquisition

The images were acquired from 29 patients as part of a larger human subjects research ethics board approved MRI-3D TRUS fusion biopsy study of our institution. Using a mechanically-assisted biopsy system described in Bax et al. [11], we acquired 3D TRUS images with an end-firing 5-9 MHz TRUS transducer probe (Philips Medical Systems, Seattle, WA) during human clinical biopsy procedures. In addition to the baseline 3D TRUS image ($I_B: \mathbb{R}^3 \rightarrow \mathbb{R}$) that would usually be acquired following the standard operating procedure for the system in [11], we acquired six other 3D TRUS images ($I_{P_i}: \mathbb{R}^3 \rightarrow \mathbb{R}$ where $i \in \{1,2,..6\}$) after positioning the TRUS probe at the corresponding standard sextant systematic biopsy locations. Figure 5.1 shows the relative bilateral sextant probe positions in base, mid and apex regions of the prostate. The mechanical encoders attached to the TRUS probe tracked the 3D position and orientation of the probe in real-time, which enabled the transformation of 3D volume to a common world coordinate system. Images were acquired from 29 patients following the protocol described above with 7 3D TRUS images per patient, for 203 images in total. During 2D-3D registration a transverse 2D slice ($I_{p_i}: \mathbb{R}^3 \rightarrow \mathbb{R}$) was obtained from 3D TRUS images at each sextant probe position and registered to the baseline 3D image.

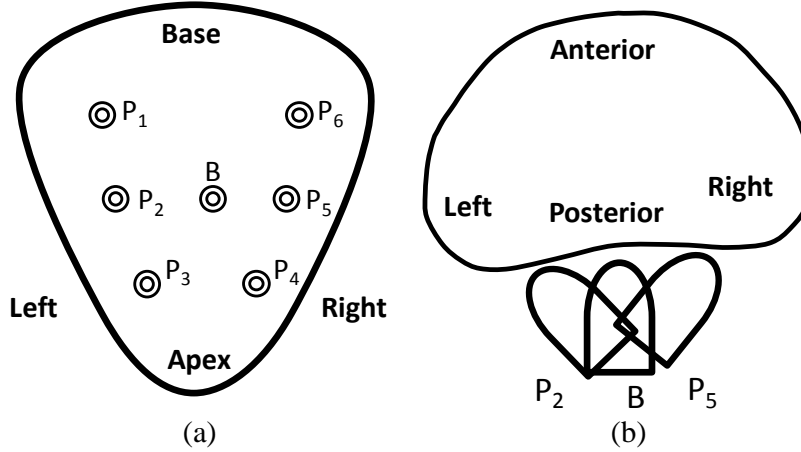


Figure 5.1: Probe positions during image acquisition shown relative to (a) coronal view (b) axial view.

5.2.2 Modeling rigid prostate motion

Corresponding fiducial pairs of anatomically homologous points (corresponding, naturally-occurring micro-calcifications) were manually identified in 3D TRUS image pairs consisting of (I_B, I_{P_i}) for each patient. We denote the fiducials identified in the baseline image as $f_B \in \mathbb{R}^3$ and those identified in the image with probe position i for that patient as $f_{P_i} \in \mathbb{R}^3$. For each patient j , we computed the optimal rigid alignment using the identified fiducials that defines the best six parameter rigid transformation vector x_{ij}^* (henceforth referred to as a *motion vector*) out of all the possible rigid transformation vectors $x_{ij} \in \mathbb{R}^6$ according to,

$$x_{ij}^* = \arg \min_{x_{ij}} \sum_{m=1}^M (f_{P_i}^m \otimes x_{ij} - f_B^m \otimes y_{ij})^2 \quad (5.1)$$

where $y_{ij}: \mathbb{R}^3 \rightarrow \mathbb{R}^3$ is the transformation obtained from tracking the probe (which maps the 3D image to the world coordinate system) and operator \otimes denotes the application of a rigid 3D transform to the fiducial location. M is the number of fiducial pairs identified per registration. Six such fiducial-based registrations per patient were performed, one for each sextant location. A total of 1003 fiducial pairs were identified with an average of 6 fiducial pairs per registration. It

is important to note that these fiducial pairs were identified only to measure and characterize prostate motion; *the registration algorithm described in the following sections is fully image-based and does not rely on the identification of fiducial landmarks.*

We analysed the estimated motion vectors to determine a suitable model to represent the observed data. Each vector x_{ij}^* , measured using manually identified fiducials, can be represented as a point in the six-dimensional (6D) rigid transformation space. Different patient and probe positions generate a cloud of points in the 6D space representing the motions observed in the data set. We assumed that prostate motion has some characteristic patterns, since the patient positioning constrains the motion in certain directions within the biopsy set-up and the transrectal access to the prostate constrains the motion of the TRUS probe during navigation. We analysed the distribution of the resulting point cloud in the 6D space to understand the patterns related to prostate movement during the biopsy procedure. During our initial analysis, the point distribution failed an uni-modal Gaussianity test (Kolmogorov-Smirnov test, $p < 0.001$). Assuming the point distribution is multi-modal, we performed an unsupervised clustering of the data by fitting a mixture-of-Gaussians (MoG) model using expectation maximization (EM) algorithm [12]. The number of clusters is an important parameter that needs to be provided as input to the EM algorithm. We used the gap statistic [13] to calculate a reasonable estimate to this parameter. We represented the estimated distribution of motion vectors as

$$\mathcal{F}(x) = \sum_{t=1}^T \mathcal{N}(\bar{x}_t, C_t) \quad (5.2)$$

where \bar{x}_t is the mean of the cluster t and C_t is the covariance matrix of the Gaussian distribution t .

5.2.3 Robust search strategy during registration optimization

Equipped with a MoG model that represents prostate motion characteristics, we explored more effective ways to traverse the transformation space during registration optimization. The class of optimization algorithms having the quadratic convergence property assume a quadratic model of the form $\mathcal{G}(x) = x^T A x + 2b^T x + c$ in the local neighborhood of the optimum [14]. If this assumption is met within reasonable bounds, these algorithms can find the function optimum within a finite number of function and/or derivative evaluations. This is a desirable property for registration problems requiring rapid convergence.

To achieve quadratic convergence, some algorithms attempt to evaluate or approximate the Hessian matrix, A , in the quadratic model, $\mathcal{G}(x)$, that captures the second order properties of the function [14]. Direction set methods like the conjugate gradient method [15] and Powell's method [16] approximate a set of directions conjugate to A without explicit knowledge of the function $\mathcal{G}(x)$. Improving (i.e., decreasing) the condition number of A (the ratio between the largest and smallest eigenvalues of A) has been demonstrated to improve the convergence properties of such algorithms [17]. This approach scales the search space to increase the isotropy of a multi-dimensional objective function, which is helpful for the optimizer to take approximately equidistant steps during the line searches performed in a set of conjugate directions. Figure 5.2 illustrates the effect of improving the condition number in a two-dimensional hypothetical function with example line search direction shown in a red arrow from the starting location depicted by the red circle.

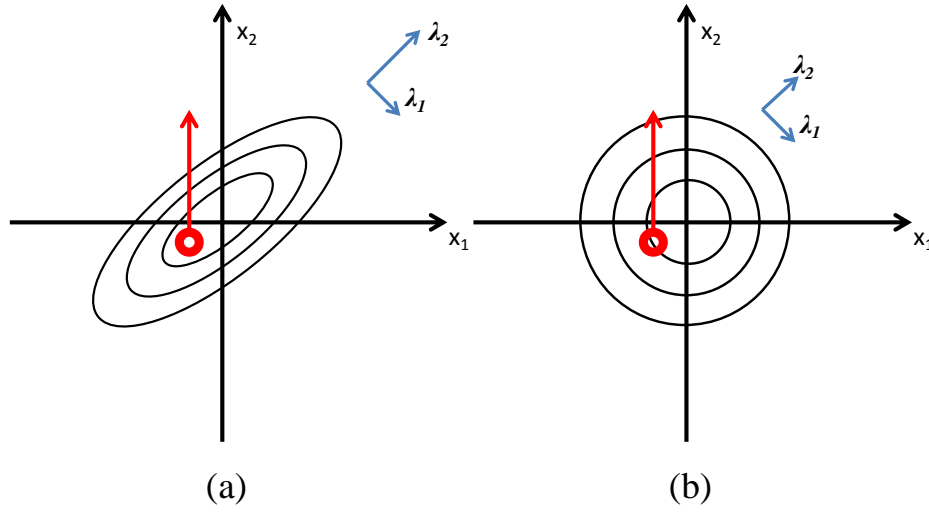


Figure 5.2: Diagram depicting the improvement (i.e., decrease) of the condition number (λ_2/λ_1) of a 2D objective function by scaling the search space according to the eigenvalues (λ_2, λ_1) of the matrix A of the objective function. (a) Initial search space of the objective function. (b) Situation after the search space is scaled according to λ_2, λ_1 . Black ellipsoids/circles show the function iso-contours, with larger circles/ellipses indicating less optimal values of the objective function. The red circle shows an example initial search location and the red arrow shows a typical Powell's method initial search direction.

Powell's method is a derivative-free optimization method that has quadratic convergence properties. For a D -dimensional quadratic function, line minimizations along D linearly independent, mutually conjugate directions will exactly find the function minimum. Powell's algorithm determines a set of such directions after initialization with the columns of any $D \times D$ orthogonal matrix. For non-quadratic functions, which are usually encountered in image registration problems, repeated cycles of D line searches are done iteratively until convergence. Usually this initialization is performed using the column vectors of an identity matrix [18].

$$C_t = U\Lambda^2U \tag{5.3}$$

$$\begin{aligned} \mathcal{N}(\bar{x}_t, C_t) &= \bar{x}_t + \mathcal{N}(0, C_t) = \bar{x}_t + C_t^{\frac{1}{2}}\mathcal{N}(0,1) \\ &= \bar{x}_t + (U\Lambda^2U)^{\frac{1}{2}}\mathcal{N}(0,1) \end{aligned} \tag{5.4}$$

U denotes the matrix containing the principal directions and Λ is the diagonal matrix containing the eigen values.

Each cluster in the MoG model can be represented by its mean x_t and covariance matrix C_t . The covariance matrix captures information related to the second order properties of the motion vector distribution in the 6D space within the cluster. The eigen decomposition of C_t yields an orthogonal matrix U as shown in Equation 5.3 that contain the principal directions of maximal inter-patient variability of the observed motion vectors in the cluster t . The eigenvalues of the matrix U (contained in the diagonal elements in the matrix Λ) can be used to scale the search along corresponding principal directions contained in U . Such an approach would scale the search space to improve the isotropic properties of the distribution of previously observed motion vectors in that cluster. Figure 5.3 illustrates how this scaling helps to guide the initial line searches towards the directions where we have already observed function optima. Thus, the principal directions given by the matrix U after being appropriately scaled by its eigenvalues could provide a good initialization for the Powell's direction set method. This is in principle different from the approach of scaling the search space to improve the condition number of the Hessian matrix, A in that we do not explicitly learn properties related to A for the functions in the observed data set. We instead use the locations within the search space where the previous functions similar to $\mathcal{G}(x)$ have converged. We adopted this approach since we observed that characteristics of the Hessian matrices for different objective functions across the patients in the data set seem to be arbitrary, yet we were able to generate a model that represent the characteristics of the locations of the function optima.

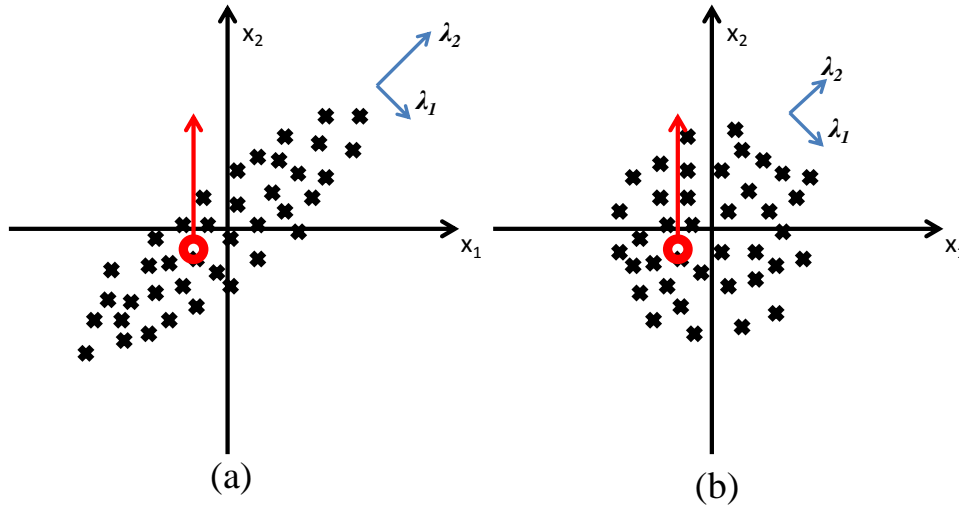


Figure 5.3: Scaling the search space according to the eigen values (λ_2, λ_1) of the covariance matrix C_t of the observed motion vectors. (a) Initial distribution of the motion vectors in the search space. (b) After the search space is scaled according to λ_2, λ_1 in the principal directions. The points representing the observed motion vectors (i.e., objective function optima). The red circle shows an example initial search location and the red arrow show a typical Powell's method initial line search direction.

We developed a two-stage search strategy with the objective of improving the robustness of registration optimization. In order to mitigate the optimizer finding local optima, a multi-start search was devised as the first step. The cluster means x_t in the MoG model were used to initialize the multiple start positions in the search space. Within each cluster, we optimized the normalized cross-correlation (NCC) image similarity metric using Powell's direction set method. Powell's method was initialized with the principal directions in the matrix U obtained from eigen decomposition of C_t as in Equation 5.3. The search along these directions was scaled using the eigenvalues in Λ , by setting the step size proportional to those eigenvalues during the line direction searches. This effectively scales the initial search directions such that the previously observed motion vectors are approximately isotropically distributed within the search space. During the second step of our search strategy, we selected the cluster that yielded best metric value after one iteration and continued the search until convergence. While the rapid convergence property of Powell's method is helpful in selecting the optimal cluster after a small

number of iterations, one iteration was empirically found to provide an accurate selection of the optimal cluster. Thus, the search strategy adds only a finite number of extra line minimizations to the standard Powell's method.

5.2.4 Experiments

For the 29 patients, we performed 174 registrations in total with 6 registrations per patient when the probe was positioned at each sextant biopsy location. We validated the registrations using the manually identified fiducials for each image pair and calculated the root mean square (RMS) target registration error (TRE). We used leave-one-out cross-validation approach; fiducials in test image of a given patient were excluded in calculating the model and search directions for that patient. To compare the results, we performed registrations using Powell's method as in [2, 18] henceforth referred to as the initial method, and using the new version described in this paper and calculated the TREs separately for each method.

5.3 Results

Multiple trials evaluating the gap statistic yielded a mode of 4 as the number of clusters (T) in our motion vector data. Table 5.1 shows the RMS TREs and standard deviations (std) of errors before registration, after registration with the initial method, after registration with the new optimization method using the MoG model, and fiducial registration errors (FRE). The FRE calculated using the fiducials used during validation provides a lower bound on the TRE that can be obtained after performing a rigid registration. Figure 5.4 shows distributions of TREs before and after registration with the two methods. With the new optimization method, we observed a statistically significant difference in TRE (paired t-test rejected the null-hypothesis with $p <$

0.001) compared to the initial method indicating an improvement in accuracy and robustness of the registration. After using learned optimization method, the average number of iterations required for convergence decreased from 4.9 to 3.3. Using a GPU accelerated implementation for NCC calculation (NVIDIA GTX 580 GPU card and Intel Xeon 2.5 GHz processor), the updated method takes approximately an additional 1.1 s. However, multi-start strategy at different motion clusters can be executed in parallel to further reduce execution time during registration. Figure 5.5 contains five representative example images, depicting the visual alignment qualitatively before and after registration with the methods described in the paper.

Table 5.1: Comparisons of performance before and after registration with new and initial methods, and FRE.

	Before	Initial method	New method	FRE
RMS TRE (mm)	4.95	3.12	2.33	1.15
std (mm)	2.37	1.70	1.12	0.57
Avg no of iterations	n/a	4.9	3.3	n/a
Execution time (s)	n/a	1.7	2.8	n/a

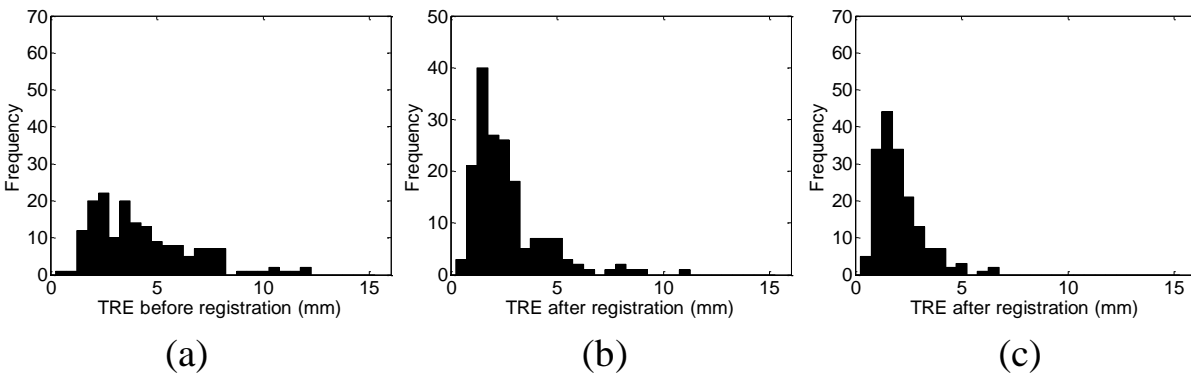


Figure 5.4: TRE histograms (a) TRE before registration. (b) TRE after registration without using learned prostate motion characteristics. (c) TRE after registration using the proposed method.

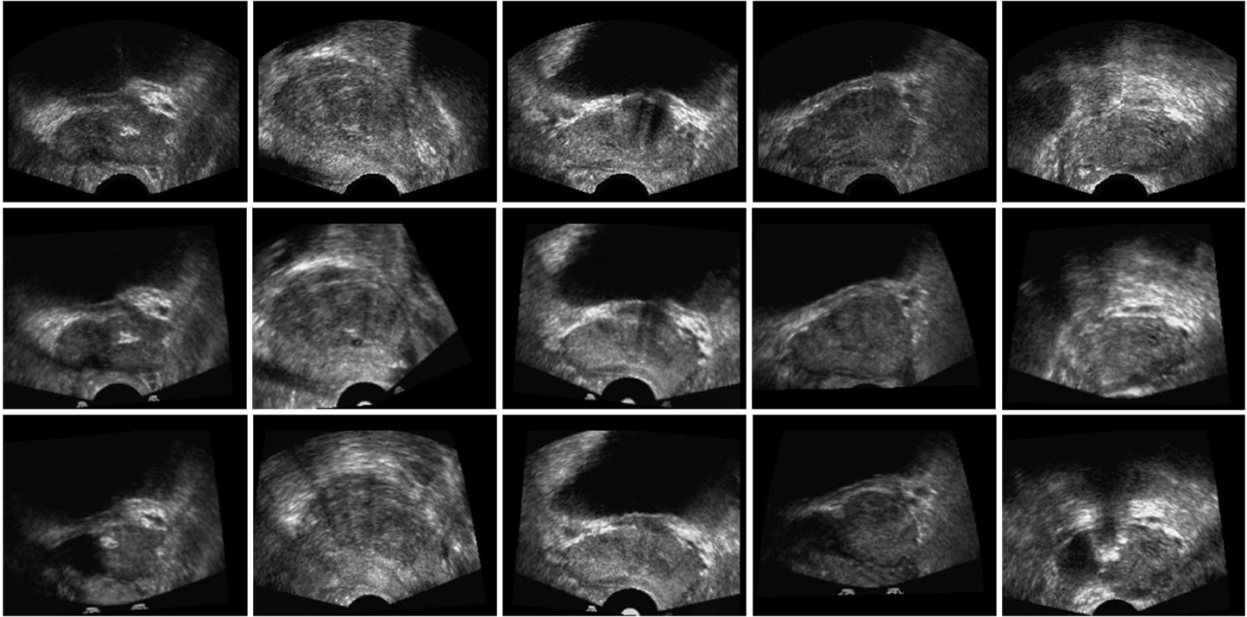


Figure 5.5: Images before and after registration for 5 patients. Top row: extracted 2D images (I_{p_i}). Middle row: corresponding frames from the registered I_B . Bottom row: corresponding frames before registration obtained from I_B after tracking the probe.

We analysed the robustness of the new method in comparison to the initial approach by evaluating the performance of the registration algorithms relative to the smallest clinically significant tumours, having a volume greater than 0.5 cm^3 according to Epstein et al. [19]. To ensure the successful sampling of tumours with 5 mm radius, we examined cases that resulted with $\text{TRE} > 5 \text{ mm}$ after the initial method to see how the accuracy has improved with the new method. Table 5.2 compares the performance of that subset of registrations ($\text{TRE} > 5 \text{ mm}$ with the initial method) with the two different methods.

Table 5.2: Comparison of performance for registrations with $\text{TRE} > 5 \text{ mm}$ with the initial approach.

	Registrations with $\text{TRE} > 5 \text{ mm}$ with the initial method				
	Mean	std	Median	Min	Max
TRE (initial) (mm)	6.70	1.71	5.96	5.00	10.84
TRE (new) (mm)	3.25	1.39	2.77	1.54	6.30
TRE(initial)-TRE (new) (mm)	3.45	2.49	2.69	-0.13	8.30

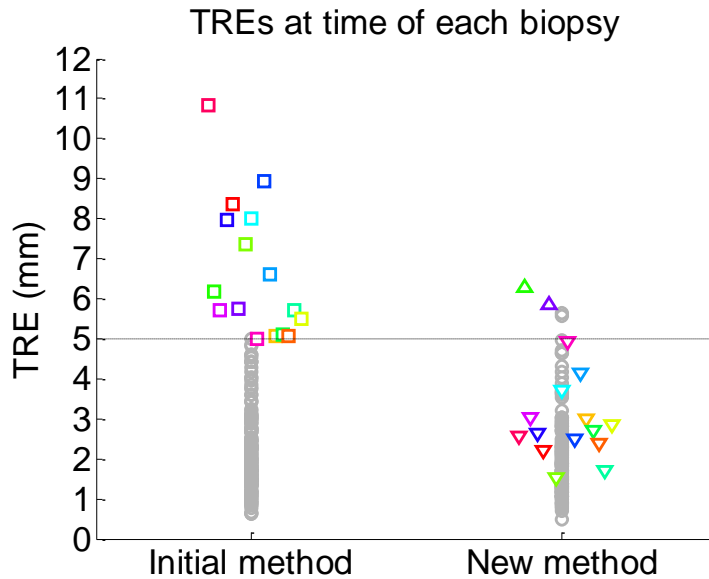


Figure 5.6: Comparisons of TREs in the two methods. The gray circles indicate biopsies for which the TRE from the initial method was ≤ 5 mm. The coloured symbols indicate biopsies for which the TRE from the initial method was > 5 mm. The coloured squares indicate TREs from the initial method, and the coloured triangles indicate TREs from the new method. Upward-pointing triangles show cases where the TRE from the new method was larger than the TRE from the initial method. Downward-pointing triangles indicate cases where the TRE from the new method was smaller than the TRE from the initial method. A symbol of a given colour corresponds to a specific registration.

With the initial method, the mean of all TREs > 5 mm was 6.7 mm. With the new method, the mean TRE for these same patient cases was reduced to 3.25 mm; a reduction of 3.45 mm. Figure 5.6 graphically illustrates the improvement in TRE given by the new method.

According to this figure, we can see that in all but two cases the new method improved over the initial method, for cases where the initial method produced a TRE of > 5 mm. We can also observe a shift of the gray circles in the downward direction with only a couple of circles lying above the 5 mm threshold line.

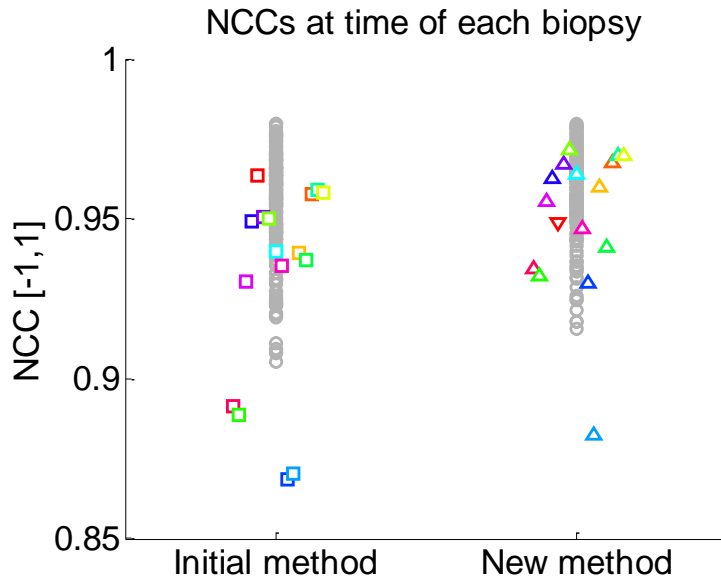


Figure 5.7: Comparison of NCC at convergence in the two methods. The gray circles indicate biopsies for which the TRE from the initial method was ≤ 5 mm. The coloured symbols indicate biopsies for which the TRE from the initial method was > 5 mm. The coloured squares indicate NCCs from the initial method, and the coloured triangles indicate NCCs from the new method. Downward-pointing triangles show cases where the NCC from the new method was smaller than the NCC from the initial method. Upward-pointing triangles indicate cases where the NCC from the new method was larger than the NCC from the initial method. A symbol of a given colour corresponds to a specific registration.

Figure 5.7 graphically illustrates the differences in NCC at convergence between the initial method and the new method. We observed that in all but one case the new approach to optimization based on learned motion data converged to a higher NCC than the initial method. We can also observe that the grey circles have an upward shift with the new method. The improved NCCs at the time of convergence indicate that the optimizer has been successful in finding desired solutions in the objective function space.

5.4 Discussion

We observed an improvement in the 2D-3D registration performance after incorporating learned prostate motion characteristics into the algorithm. Using the initial method, the 2D-3D registration had a TRE > 5 mm for nearly 10% (9.25%) of the biopsies in our sample. If 9.25%

of all biopsies are guided based using motion correction with $TRE > 5$ mm, then on average every patient undergoing 12-core extended sextant biopsy will have one or more biopsies taken with sufficient motion correction error such that a tumour of clinically significant size may be missed. Using the new method, the 2D-3D registration had a $TRE > 5$ mm for 1.16% of the biopsies in our sample. If 1.16% of all biopsies are guided based on using motion correction with $TRE > 5$ mm, then on average 1 out of every 86 biopsies will be taken with sufficient motion correction error such that a tumour of clinically significant size may be missed. Thus, on average, one out of every eight patients undergoing 12-core extended sextant biopsy will have one or more biopsies taken with sufficient motion correction error such that a tumour of clinically significant size may be missed.

The calculation of the best rigid transformations (x_{ij}^*) to characterize prostate motion is limited by the operator's ability to accurately identify and correspond fiducial locations. Since we considered the transformations given by the manually identified fiducials as the ground truth, fiducial localization error limits our ability to measure a registration algorithm's improvement of accuracy. Furthermore, any non-rigid deformation of the prostate would challenge our assumption of rigid motion. The ability of the registration to match the best rigid alignment calculated based on fiducials identified throughout the prostate could also be limited by the fact that we are restricted to using a single 2D slice during registration. In such a situation, non-rigid deformation might pose an additional challenge for the algorithm to estimate the overall rigid motion of the prostate by only using the image information in the 2D plane.

5.5 Conclusions

In this paper, we demonstrated that the learned prostate motion directions can be used to improve 2D-3D TRUS registration optimization, which has the potential to improve the clinical outcomes of MRI-3D TRUS fusion biopsy. Our results indicate that we can improve the accuracy and robustness of the algorithm, at the cost of 1-2 s of additional execution time. This would help 3D TRUS-guided biopsy systems to achieve clinically desired level of accuracy in needle targeting.

References

1. S. Xu, J. Kruecker, B. Turkbey, N. Glossop, A. K. Singh, P. Choyke, P. Pinto and B. J. Wood, "Real-time MRI-TRUS fusion for guidance of targeted prostate biopsies," *Comput Aided Surg* **13**, 255-264 (2008).
2. T. De Silva, A. Fenster, D. Cool, L. Gardi, C. Romagnoli, J. Samarabandu and A. D. Ward, "2D-3D rigid registration to compensate for prostate motion during 3D-TRUS guided biopsy," *Medical Physics* **40**, 022904 (2013).
3. M. Baumann, P. Mozer, V. Daanen and J. Troccaz, "Prostate biopsy tracking with deformation estimation," *Med Image Anal* **16**, 562-576 (2013).
4. M. Baumann, P. Mozer, V. Daanen and J. Troccaz, "Prostate biopsy assistance system with gland deformation estimation for enhanced precision," *Med Image Comput Comput Assist Interv* **12**, 67-74 (2009).
5. Y. P. Hu, H. U. Ahmed, Z. Taylor, C. Allen, M. Emberton, D. Hawkes and D. Barratt, "MR to ultrasound registration for image-guided prostate interventions," *Medical Image Analysis* **16**, 687-703 (2012).
6. A. Mohamed, C. Davatzikos and R. Taylor, In: Proc. of the 5th International Conference on MICCAI, London, UK, 2002.
7. Z. Xue, D. Shen, B. Karacali and C. Davatzikos, "Statistical representation and simulation of high-dimensional deformations: application to synthesizing brain deformations," *Med Image Comput Comput Assist Interv* **8**, 500-508 (2005).
8. A. Melbourne, D. Atkinson, M. J. White, D. Collins, M. Leach and D. Hawkes, "Registration of dynamic contrast-enhanced MRI using a progressive principal component registration (PPCR)," *Phys Med Biol* **52**, 5147-5156 (2007).
9. D. H. Chung, I. D. Yun and S. U. Lee, "Registration of multiple-range views using the reverse-calibration technique," *Pattern Recogn* **31**, 457-464 (1998).
10. M. Jenkinson, P. Bannister, M. Brady and S. Smith, "Improved optimization for the robust and accurate linear registration and motion correction of brain images," *Neuroimage* **17**, 825-841 (2002).
11. J. Bax, D. Cool, L. Gardi, K. Knight, D. Smith, J. Montreuil, S. Sherebrin, C. Romagnoli and A. Fenster, "Mechanically assisted 3D ultrasound guided prostate biopsy system," *Med Phys* **35**, 5397-5410 (2008).
12. R. Sundberg, "Iterative Method for Solution of Likelihood Equations for Incomplete Data from Exponential Families," *Commun Stat B-Simul* **B 5**, 55-64 (1976).

13. R. Tibshirani, G. Walther and T. Hastie, "Estimating the number of clusters in a data set via the gap statistic," *Journal of the Royal Statistical Society Series B-Statistical Methodology* **63**, 411-423 (2001).
14. R. Fletcher, *Practical Methods of Optimization*, 2nd Edition ed. (Wiley, 2000).
15. M. R. Hestenes and E. Stiefel, "Methods of Conjugate Gradients for Solving Linear Systems," *J Res Nat Bur Stand* **49**, 409-436 (1952).
16. M. J. D. Powell, "A Method for Minimizing a Sum of Squares of Non-Linear Functions without Calculating Derivatives," *Comput J* **7**, 303-307 (1965).
17. J. R. Shewchuk, "An Introduction to the Conjugate Gradient Method Without the Agonizing Pain ", (1994).
18. W. H. Press, B. P. Flannery, S. A. Teukolsky and W. T. Vetterling, *Numerical Recipes in C*, 2 ed. (Cambridge University Press, 1992).
19. J. I. Epstein, P. C. Walsh, M. Carmichael and C. B. Brendler, "Pathologic and clinical findings to predict tumor extent of nonpalpable (stage T1c) prostate cancer," *JAMA : the journal of the American Medical Association* **271**, 368-374 (1994).

Chapter 6.

Conclusions and Directions for Future Work

6.1 Conclusions

The work in this thesis intends to improve needle targeting accuracy of 3D TRUS-guided biopsy systems. Towards achieving this goal, the errors due to patient and prostate motion during the procedure were quantified and methods were developed to compensate for the intermittent motion via rapid image-based registration techniques. The methods developed in this work have been successfully integrated into the mechanically assisted 3D TRUS-guided biopsy system [1] previously developed in our lab and are currently being used in human clinical biopsy procedures as part of an ongoing study. The work was divided into four chapters according to the objectives listed in the Section 1.9, and the conclusions of each are discussed in the following.

In Chapter 2, we used non-rigid registration of 2D TRUS images to quantify the deformation that occurs during the needle insertion and the biopsy gun firing procedure and compared this effect in biopsies performed using a hand held TRUS probe with those performed using mechanically assisted 3D TRUS-guided biopsy system [1]. While such errors had been previously quantified in prostate brachytherapy applications where accurate needle guidance is necessary for radioactive seed implantations, we investigated this problem in the context of 3D TRUS-guided biopsy. Prostate deformation during needle insertion can cause target misalignments after the physician has successfully aligned the biopsy needle trajectory with the target locations in preparation for taking a

tissue sample. Since the needle insertion and biopsy gun firing happen in a rapid progression within a sub-second interval, the targeting error due to prostate deformation in that duration is very challenging to compensate. However, given the need to accurately sample the smallest clinically significant tumours, it is an important consideration when setting the design specifications for MR-targeted TRUS-guided prostate biopsy systems. As described in Section 1.10.2, an image registration algorithm with RMS TRE ≤ 2.3 mm is required for the central hypothesis of this work to be confirmed, in the context of our measured tissue displacement due to biopsy needle insertion.

In Chapter 3, we described a technique to compensate for intermittent patient and prostate motion during biopsy, which is the central problem addressed in the work of this thesis. Compared to the errors quantified in Chapter 2, patient motion due to discomfort and prostate motion due to applied TRUS probe pressure caused larger target misalignments, limiting needle targeting accuracy [2]. We developed an image-based 2D-3D registration algorithm to align live 2D TRUS images acquired during the procedure with the baseline 3D TRUS image acquired immediately prior to performing biopsy. The accuracy was measured by calculating the TRE using manually identified fiducials (micro-calcifications) of the prostate. A GPU-based implementation was used to improve the registration speed. While this showed encouraging results by achieving statistically significant improvements in accuracy, there were some registrations with error >5 mm and a measured RMS TRE of 3.2 mm. Therefore, methods to improve the accuracy and robustness of this technique would be helpful to meet the clinical requirements.

In Chapter 4, we evaluated the utility of incorporating additional intra-procedural 3D TRUS image information in guiding registration for improved motion compensation. The limited anatomical context available in a subset of the live 2D TRUS images might not capture sufficient information to obtain an accurate registration with the baseline 3D TRUS image. While 2D TRUS images are widely used for intra-procedural guidance, some solutions utilize richer intra-procedural images such as bi- or multi-planar TRUS or 3D TRUS, acquired by specialized probes. Therefore, the impact of such richer intra-procedural imaging on displacement compensation accuracy was measured to evaluate the tradeoff between cost and complexity of intra-procedural imaging versus improved displacement compensation. We performed an extensive validation using baseline and intra-procedural 3D TRUS images acquired from 29 patients. While the majority of the registrations using 2D TRUS images provided a clinically desired level of accuracy, intra-procedural 3D imaging helped improve the overall registration accuracy and robustness, especially in the base and apex regions of the prostate. These results are helpful for devising image-based registration methods and designing clinical workflow for motion compensation in 3D TRUS-guided biopsy systems.

Towards the objective of improving the robustness of registration for motion compensation, we investigated an alternative approach in Chapter 5 that does not require additional image acquisitions during the procedure. Since the patient motion is constrained while being in the left lateral decubitus positioning within the biopsy setup and the TRUS probe motion is restricted while accessing the prostate transrectally, it is reasonable to assume that prostate motion has some characteristic patterns. Incorporating

information of the identified characteristic patterns of prostate motion during registration optimization helped to improve the robustness in an effective manner.

In this thesis, we have demonstrated the use of image-based registration methods to quantify and compensate for prostate motion during 3D TRUS-guided biopsy. According to our hypothesis, the RMS error of the biopsy systems should be ≤ 2.5 mm in order to accurately sample the smallest clinically significant tumours. The errors due to prostate deformation during needle insertion and biopsy-gun firing restrict this requirement further to 2.3 mm. Although 2D-3D registration methods described in Chapter 3 were encouraging, with statistically significant improvements in compensating for intermittent patient and prostate motion, methods to further improve accuracy and robustness were needed for the successful clinical translation of this technique. Chapter 4 and 5 describe two different approaches to achieving improved registration accuracies. The improved accuracy and robustness either by acquiring intra-procedure 3D image information for use during registration or by improving the registration optimization using the learned motion characteristics of the prostate have demonstrated performance improvements in image-based registration that meet the clinical requirements for needle targeting accuracy of the biopsy system.

Thus, *the central hypothesis of this thesis is confirmed* when either of the approaches described in Chapters 4 or 5 are applied, and the choice of approach to use in a given context may be guided by ultrasound probe/machine availability. The central hypothesis of this thesis is not confirmed when only the approach described in Chapter 3 is applied.

6.2 Suggestions for future work

The registration techniques developed in this work could be directly helpful in ongoing clinical investigations related to prostate biopsy. There are other clinical applications that require rapid registration to transform pre-procedure image information to the intra-procedure image space to improve diagnostic and therapeutic clinical outcomes in image-guided interventions. Some extensions of the work described in this thesis might lead to applications in multiple such areas of currently active research.

6.2.1 Applications in ongoing clinical studies

Multiple clinical studies [3-5] have reported improved cancer detection rates using MR-targeted biopsy schemes. It would be interesting to investigate how the improved needle targeting accuracy after integrating prostate motion compensation into the clinical workflow during the procedure impact clinical outcomes of the procedure. The potential impact in cancer detection rates could be investigated in a prospective clinical study. The improved cancer detection rates could elevate the ability of the physician to better differentiate between clinically aggressive and indolent tumours by strengthening the confidence of the evidence. During prostate cancer diagnosis and patient risk stratification, however, the current standards of interpreting biopsy results are calibrated to the conventional random systematic biopsy schemes, which carry a higher degree of uncertainty. The ability to accurately target suspicious foci might lead to re-visit the current guidelines to improve the interpretation of biopsy results with more reliable evidence of the disease at hand.

6.2.2 Applications in other clinical procedures

The techniques developed in this thesis could have relevance in other image-guided interventions that require fast and accurate registration to compensate for organ motion. One such example with direct relevance to prostate cancer management is in emerging [6, 7] interventional systems developed to treat intermediate-risk prostate cancer with localized ablation. In such systems, tumours contoured prior to the procedure need to be detected and verified in the intra-procedure images prior to ablation. Motion correction algorithms could be helpful to align the target regions during the procedure to improve the accuracy of ablating the intended region and to ultimately reduce the margins ablated around the tumour due to uncertainty. Prostate deformation could be a potential challenge in developing such registration algorithms for some applications. For example, during focal laser ablation [6] of tumours, intra-procedure MR images are acquired to verify the target region. The endorectal coil used to acquire MR images could deform the prostate differently than when it was acquired prior to the procedure for diagnostic purposes. Non-rigid registration algorithms might be necessary to account for such differences in deformation during the procedure after achieving a robust rigid registration as an initial step. The techniques described in this work needs to be extended to account for non-rigid deformations in such applications.

Ultrasound-guided interventional systems have recently been developed for tissue ablation in kidney [8] and liver [9]. Organ motion during the procedure could limit their accuracy in delivering the treatment to the desired region. Hence, these systems might also potentially benefit from rapid image registration algorithms to compensate for organ

motion. However, the characteristics of motion in the organ of interest are an important consideration when developing registration techniques. The liver motion, for example, could be affected primarily by the periodic breathing, since it is an organ with close anatomical proximity to the lung. When compensating for such continuous and periodic motion, the registration might need to be performed faster than what was required during prostate biopsy. Efficient software code optimization and parallel implementations could help to further improve registration times.

6.2.3 Applications in image-based tracking

Intra-procedure image tracking is an essential component when developing systems to perform many image-guided interventions. Electromagnetic, optical and mechanical devices are typically used to track real-time imaging devices during the procedures. Pure image-based tracking is an alternative method that can be used to determine the position and the orientation of the imaging device via image registration. Low cost and compact design are the major advantages of this approach by eliminating the need for hardware tracking devices in the system. In the experiments described in this thesis, we used the transformation given by the mechanical tracking device to initialize the registrations. If the registration is performed without this initialization, it has to simultaneously compensate for motion of the prostate as well as the motion of the TRUS probe. This would be a very challenging correspondence problem considering the limited information available in a single plane 2D TRUS image. If the prior knowledge of the prostate anatomy and the prostate motion can be used to provide a reasonable initialization to the registration algorithm, that could help to make the registration problem more tractable

when only using the image information. Technical advancements in methodology for incorporating prior domain knowledge into the registration framework might help to achieve accurate and robust results that would benefit the development of software-based solutions and their widespread use for tracking purposes.

References

1. J. Bax, D. Cool, L. Gardi, K. Knight, D. Smith, J. Montreuil, S. Sherebrin, C. Romagnoli and A. Fenster, "Mechanically assisted 3D ultrasound guided prostate biopsy system," *Med Phys* **35**, 5397-5410 (2008).
2. V. V. Karnik, A. Fenster, J. Bax, D. W. Cool, L. Gardi, I. Gyacskov, C. Romagnoli and A. D. Ward, "Assessment of image registration accuracy in three-dimensional transrectal ultrasound guided prostate biopsy," *Med Phys* **37**, 802-813 (2010).
3. A. Peltier, F. Aoun, F. El-Khoury, E. Hawaux, K. Limani, K. Narahari, N. Sirtaine and R. van Velthoven, "3D versus 2D Systematic Transrectal Ultrasound-Guided Prostate Biopsy: Higher Cancer Detection Rate in Clinical Practice," *Prostate Cancer* **2013**, 783243 (2013).
4. G. A. Sonn, S. Natarajan, D. J. A. Margolis, M. MacAiran, P. Lieu, J. T. Huang, F. J. Dorey and L. S. Marks, "Targeted Biopsy in the Detection of Prostate Cancer Using an Office Based Magnetic Resonance Ultrasound Fusion Device," *Journal of Urology* **189**, 86-91 (2013).
5. D. G. Engehausen, K. Engelhard, S. A. Schwab, M. Uder, S. Wach, B. Wullich and F. S. Krause, "Magnetic Resonance Image-Guided Biopsies with a High Detection Rate of Prostate Cancer," *Sci World J* (2012).
6. J. Cepek, B. A. Chronik, U. Lindner, J. Trachtenberg, S. R. Davidson, J. Bax and A. Fenster, "A system for MRI-guided transperineal delivery of needles to the prostate for focal therapy," *Med Phys* **40**, 012304 (2013).
7. S. Crouzet, J. Y. Chapelon, O. Rouviere, F. Mege-Lechevallier, M. Colombel, H. Tonoli-Catez, X. Martin and A. Gelet, "Whole-gland ablation of localized prostate cancer with high-intensity focused ultrasound: oncologic outcomes and morbidity in 1002 patients," *Eur Urol* **65**, 907-914 (2014).
8. A. J. Hung, Y. Ma, P. Zehnder, M. Nakamoto, I. S. Gill and O. Ukimura, "Percutaneous radiofrequency ablation of virtual tumours in canine kidney using Global Positioning System-like technology," *BJU Int* **109**, 1398-1403 (2012).
9. H. Neshat, D. W. Cool, K. Barker, L. Gardi, N. Kakani and A. Fenster, "A 3D ultrasound scanning system for image guided liver interventions," *Med Phys* **40**, 112903 (2013).

Appendix A

A.1 Permission to reproduce previously published material in Chapters 2, 3 and 4



American Association of Physicists in Medicine

One Physics Ellipse
College Park, MD 20740-3846
(301) 209-3350
Fax (301) 209-0862
<http://www.aapm.org>

Office of the Executive Director
Angela R. Keyser
Phone: 301-209-3385 Fax: 301-209-0862
E-mail: akeyser@aapm.org

DATE OF REQUEST: May 12, 2014

FROM:

Tharindu De Silva, [REDACTED]

EMAIL ADDRESS: [REDACTED]

1. Permission is granted to:

Tharindu De Silva, Robarts Research Institute

2. Permission is requested to use the following material:

- T. De Silva, A. Fenster, J. Bax, C. Romagnoli, J. Izawa, J. Samarabandu, and A. D. Ward, "Quantification of prostate deformation due to needle insertion during TRUS-guided biopsy: Comparison of hand-held and mechanically stabilized systems," *Medical Physics*, 38(3): 1718-32, 2011.
- T. De Silva, A. Fenster, D. W. Cool, L. Gardi, C. Romagnoli, J. Samarabandu, and A. D. Ward, "2D-3D rigid registration to compensate for prostate motion during 3D TRUS-guided biopsy," *Medical Physics*, 40(2): 022904, 2013.
- T. De Silva, D. W. Cool, L. Gardi, C. Romagnoli, A. Fenster, and A. D. Ward, "Evaluating the utility of intra-procedural 3D TRUS image information in guiding registration for displacement compensation during prostate biopsy. (Recently submitted manuscript).

3. For what purpose:

To include in my PhD thesis.

Authors seeking permission must also notify the first author of the article from which permission is being sought.

Permission is hereby granted: [REDACTED]

Signature

May 13, 2014

Date

The Association's Journals are *Medical Physics* and *Journal of Applied Clinical Medical Physics*
Member Society of the American Institute of Physics and the International Organization of Medical Physics

A.2 Permission to reproduce previously published material in Chapters 5

Rightslink Printable License

<https://s100.copyright.com/CustomerAdmin/PLF.jsp?ref=243ec7a9-44c...>

SPRINGER LICENSE TERMS AND CONDITIONS

May 11, 2014

This is a License Agreement between Tharindu S De Silva ("You") and Springer ("Springer") provided by Copyright Clearance Center ("CCC"). The license consists of your order details, the terms and conditions provided by Springer, and the payment terms and conditions.

All payments must be made in full to CCC. For payment instructions, please see information listed at the bottom of this form.

License Number	3383250744516
License date	May 06, 2014
Licensed content publisher	Springer
Licensed content publication	Springer eBook
Licensed content title	Improving 2D-3D Registration Optimization Using Learned Prostate Motion Data
Licensed content author	Tharindu De Silva
Licensed content date	Jan 1, 2013
Type of Use	Thesis/Dissertation
Portion	Excerpts
Author of this Springer article	Yes and you are a contributor of the new work
Order reference number	None
Title of your thesis / dissertation	Image-based registration methods for quantification and compensation of prostate motion during trans-rectal ultrasound (TRUS)-guided biopsy
Expected completion date	May 2014
Estimated size(pages)	200
Total	0.00 CAD
Terms and Conditions	

Introduction

The publisher for this copyrighted material is Springer Science + Business Media. By clicking "accept" in connection with completing this licensing transaction, you agree that the following terms and conditions apply to this transaction (along with the Billing and Payment terms and conditions established by Copyright Clearance Center, Inc. ("CCC"), at the time that you opened your Rightslink account and that are available at any time at <http://myaccount.copyright.com>).

Limited License

With reference to your request to reprint in your thesis material on which Springer Science and Business Media control the copyright, permission is granted, free of charge, for the use

indicated in your enquiry.

Licenses are for one-time use only with a maximum distribution equal to the number that you identified in the licensing process.

This License includes use in an electronic form, provided its password protected or on the university's intranet or repository, including UMI (according to the definition at the Sherpa website: <http://www.sherpa.ac.uk/romeo/>). For any other electronic use, please contact Springer at (permissions.dordrecht@springer.com or permissions.heidelberg@springer.com).

The material can only be used for the purpose of defending your thesis limited to university-use only. If the thesis is going to be published, permission needs to be re-obtained (selecting "book/textbook" as the type of use).

Although Springer holds copyright to the material and is entitled to negotiate on rights, this license is only valid, subject to a courtesy information to the author (address is given with the article/chapter) and provided it concerns original material which does not carry references to other sources (if material in question appears with credit to another source, authorization from that source is required as well).

Permission free of charge on this occasion does not prejudice any rights we might have to charge for reproduction of our copyrighted material in the future.

Altering/Modifying Material: Not Permitted

You may not alter or modify the material in any manner. Abbreviations, additions, deletions and/or any other alterations shall be made only with prior written authorization of the author(s) and/or Springer Science + Business Media. (Please contact Springer at (permissions.dordrecht@springer.com or permissions.heidelberg@springer.com))

Reservation of Rights

Springer Science + Business Media reserves all rights not specifically granted in the combination of (i) the license details provided by you and accepted in the course of this licensing transaction, (ii) these terms and conditions and (iii) CCC's Billing and Payment terms and conditions.

Copyright Notice:Disclaimer

You must include the following copyright and permission notice in connection with any reproduction of the licensed material: "Springer and the original publisher /journal title, volume, year of publication, page, chapter/article title, name(s) of author(s), figure number(s), original copyright notice) is given to the publication in which the material was originally published, by adding; with kind permission from Springer Science and Business Media"

Warranties: None

Example 1: Springer Science + Business Media makes no representations or warranties with respect to the licensed material.

Example 2: Springer Science + Business Media makes no representations or warranties with respect to the licensed material and adopts on its own behalf the limitations and disclaimers established by CCC on its behalf in its Billing and Payment terms and conditions for this licensing transaction.

Indemnity

You hereby indemnify and agree to hold harmless Springer Science + Business Media and CCC, and their respective officers, directors, employees and agents, from and against any and all claims arising out of your use of the licensed material other than as specifically authorized pursuant to this license.

No Transfer of License

This license is personal to you and may not be sublicensed, assigned, or transferred by you to any other person without Springer Science + Business Media's written permission.

No Amendment Except in Writing

This license may not be amended except in a writing signed by both parties (or, in the case of Springer Science + Business Media, by CCC on Springer Science + Business Media's behalf).

Objection to Contrary Terms

Springer Science + Business Media hereby objects to any terms contained in any purchase order, acknowledgment, check endorsement or other writing prepared by you, which terms are inconsistent with these terms and conditions or CCC's Billing and Payment terms and conditions. These terms and conditions, together with CCC's Billing and Payment terms and conditions (which are incorporated herein), comprise the entire agreement between you and Springer Science + Business Media (and CCC) concerning this licensing transaction. In the event of any conflict between your obligations established by these terms and conditions and those established by CCC's Billing and Payment terms and conditions, these terms and conditions shall control.

Jurisdiction

All disputes that may arise in connection with this present License, or the breach thereof, shall be settled exclusively by arbitration, to be held in The Netherlands, in accordance with Dutch law, and to be conducted under the Rules of the 'Netherlands Arbitrage Instituut' (Netherlands Institute of Arbitration). *OR:*

All disputes that may arise in connection with this present License, or the breach thereof, shall be settled exclusively by arbitration, to be held in the Federal Republic of Germany, in accordance with German law.

Other terms and conditions:

v1.3

If you would like to pay for this license now, please remit this license along with your payment made payable to "COPYRIGHT CLEARANCE CENTER" otherwise you will be invoiced within 48 hours of the license date. Payment should be in the form of a check

or money order referencing your account number and this invoice number 501296247. Once you receive your invoice for this order, you may pay your invoice by credit card. Please follow instructions provided at that time.

**Make Payment To:
Copyright Clearance Center
Dept 001
P.O. Box 843006
Boston, MA 02284-3006**

For suggestions or comments regarding this order, contact RightsLink Customer Support: customercare@copyright.com or +1-877-622-5543 (toll free in the US) or +1-978-646-2777.

Gratis licenses (referencing \$0 in the Total field) are free. Please retain this printable license for your reference. No payment is required.

Curriculum Vitae

EDUCATION

- The University of Western Ontario, Canada **2009-present**
PhD Candidate in Biomedical Engineering
Thesis title: *Image-based registration methods for quantification and compensation of prostate motion during trans-rectal ultrasound (TRUS)-guided biopsy*
- University of Moratuwa, Sri Lanka **2004-2008**
B. Sc. in Engineering (First Class Honors) – 98th percentile overall GPA (3.99 / 4.2)
Major: Electronics and Telecommunication Engineering
Thesis title: *Centralized traffic controlling system for railways*

SCHOLARSHIPS, HONORS AND AWARDS

- 2013:** Third prize award, Imaging Network Ontario (ImNO) Consortium poster competition.
- 2012:** Third prize award, Imaging Network Ontario (ImNO) Consortium poster competition.
- 2011:** First prize award, Imaging Network Ontario (ImNO) Consortium poster competition.
- 2010-2012:** Natural Sciences and Engineering Council (NSERC) in Computer-Assisted Medical Interventions (CAMI) graduate scholarship (\$15,000/yr).
- 2009-2014:** Western Graduate Research Scholarship, The University of Western Ontario – Biomedical Engineering Graduate Program (\$16,000/yr).
- 2004-2008:** Academic merit scholarship sponsored by Dialog Telekom PLC, Sri Lanka; provided funding during undergraduate study (\$2000). This is a competitive scholarship awarded to the top 25 students in the physical science stream in Sri Lanka.
- 2004-2008:** Dean's List, University of Moratuwa (For achieving grade point average higher than 3.8 out of 4.2 in every semester of attendance).
- 2007:** Awarded University Colors for tennis for being a member of the champion-team in Sri Lanka University Games (SLUG).

PUBLICATIONS

PEER-REVIEWED JOURNALS (Published, accepted or under review)

1. **T. De Silva**, A. Fenster, D. W. Cool, L. Gardi, C. Romagnoli, J. Samarabandu, A. D. Ward, "2D-3D rigid registration to compensate for prostate motion during 3D TRUS-guided biopsy", *Medical Physics*, 40(2), 022904, 2013.

2. **T. De Silva**, A. Fenster, J. Bax, C. Romagnoli, J. Izawa, J. Samarabandu, A. D. Ward, "Quantification of prostate deformation due to needle insertion during TRUS-guided biopsy: Comparison of hand-held and mechanically stabilized systems", *Medical Physics*, 38(3): 1718-32, 2011.
3. **T. De Silva**, D. W. Cool, L. Gardi, C. Romagnoli, A. Fenster, A. D. Ward, "Evaluating the utility of intra-procedure 3D TRUS image information in guiding registration for motion compensation during prostate biopsy", submitted to *Medical Physics*, submitted January, 2014. (under review)

PEER-REVIEWED JOURNALS (Work in progress with greater than 80% work completed)

4. **T. De Silva**, D. W. Cool, J. Yuan, C. Romagnoli, A. Fenster, A. D. Ward, "Robust 2D-3D registration optimization using learned prostate motion data", in preparation for *IEEE Transactions on Medical Imaging*.

PEER-REVIEWED CONFERENCE PROCEEDINGS

1. **T. De Silva**, D. W. Cool, C. Romagnoli, A. Fenster, A. D. Ward, "Evaluating the utility of 3D TRUS image information in guiding intra-procedure registration for motion compensation", *Proceedings of the SPIE International Symposium on Medical Imaging 2014*, San Diego, CA: February 15-20, 2014 (accepted for **podium presentation**).
2. **T. De Silva**, D. Cool, J. Yuan, C. Romagnoli, A. Fenster, A. D. Ward. "Improving 2D-3D registration optimization using learned prostate motion data" Lecture Notes in Computer Science, *Medical Image Computing and Computer Assisted Intervention (MICCAI)*, 6363, 124-131, Nagoya, Japan, 2013 (**8 pages**; poster presentation; **32% acceptance rate**).
3. **T. De Silva**, A. Fenster, J. Bax, L. Gardi, C. Romagnoli, J. Samarabandu, A. D. Ward. "2D-3D rigid registration to compensate for prostate motion during 3D TRUS-guided biopsy", *Proceedings of the SPIE International Symposium on Medical Imaging 2012*, paper # 63160O, San Diego, CA: February 4-9, 2011 (**podium presentation**).
4. **T. De Silva**, A. Fenster, C. Romagnoli, J. Samarabandu, A. D. Ward, "Evaluating image-similarity metrics to detect prostate motion during 3D TRUS-guided prostate biopsy", *AAPM/COMP*, Vancouver, Canada, 2011 (**podium presentation**).
5. **T. De Silva**, J. Bax, A. Fenster, J. Samarabandu, A. D. Ward, "Quantification of prostate deformation due to needle insertion during TRUS-guided biopsy: Comparison of hand-held and mechanically stabilized systems", *Proceedings of the SPIE International Symposium on Medical Imaging 2011*, paper # 79680U, Orlando, FL: February 13-17, 2011 (**podium presentation**).
6. **T. De Silva**, A. Fenster, J. Samarabandu, A. D. Ward, "Quantification of prostate deformation due to needle insertion during TRUS-guided biopsy", Lecture Notes in Computer Science, *Medical Image Computing and Computer Assisted Intervention (MICCAI)*, 6363, 213-220, Beijing, China, 2010 (**8 pages**; poster presentation; **32% acceptance rate**).

7. T. Ambegoda, **T. De Silva**, K.T. Hemachandra, T.N. Samarasinghe, K. Samarasinghe Centralized Traffic Controlling System for Sri Lanka Railways. *IEEE 4th International Conference on Information and Automation for Sustainability*, 145-149, 2008 (**podium presentation**).

INVITED TALKS

- “Image-based registration for prostate motion compensation during 3D TRUS-guided biopsy”. Techna Institute, Toronto, ON, Canada. November 18, 2013. Host: Dr. Vladimir Pekar.
- “Quantification of prostate deformation due to needle insertion during TRUS-guided biopsy: Comparison of hand-held and mechanically stabilized systems”, Huazhong University of Science and Technology, Wuhan, Hubei, China. September 27, 2010. Host: Dr. Mingyue Ding.
- “Quantification of prostate deformation due to needle insertion during TRUS-guided biopsy”, University of Moratuwa, Sri Lanka. June 10, 2010. Host: Dr. I. Dayawansa.

PROFESSIONAL EXPERIENCE

2011 Participated in **Google Summer of Code project (GSOC)** for **Kitware Inc.**

Oversight: Dr. Marcus D. Hanwell and Dr. Jeff Baumes

Implemented and integrated two selected algorithms from IEEE VisWeek 2010 to VTK ((1) vtkAxisExtended and (2) vtkCellTreeLocator). This work was featured in a Kitware blog post at <http://www.kitware.com/source/home/post/44>.

2008-2009 **Assistant Research Engineer** for computer vision related embedded-design projects at Zone24x7 Research Laboratory, Sri Lanka.

2006-2007 **Telecommunication Engineering Intern** at Dialog Telekom PLC, Sri Lanka, which is the largest telecommunication service provider in Sri Lanka.

2009-2014 **Teaching Assistant** at the University of Western Ontario for the following courses.

2009 SE2250a Software Construction. **Oversight:** Dr. Jagath Samarabandu.

2010 ENGSCI1036b Programming Fundamentals for Engineers. **Oversight:** Dr. Quazi Rahman.

2011 SE3350 Software Engineering Design. **Oversight:** Dr. Keivan Kian-Mehr.

2012 ECE4455 Engineering Analysis of Physiological Systems. **Oversight:** Dr. James Lacefield.

2013 ECE4438 Advanced Image Processing and Analysis. **Oversight:** Dr. Aaron D. Ward.

2014 ES1050 Engineering Design. **Oversight:** Dr. Sharzad Barghi.

